12 90

UNIVERSIDADE Đ COIMBRA

Joana Pires Morgado Fernandes Pereira

VARIATIONS OF THE IONOSPHERIC TOTAL ELECTRON CONTENT OVER CONTINENTAL PORTUGAL AND ISLANDS

VARIATIONS OF THE IONOSPHERIC TOTAL ELECTRON CONTENT OVER CONTINENTAL PORTUGAL AND ISLANDS

by

Joana Morgado Pereira

Supervisor: Anna Morozova

September 2023

A dissertation submitted to the
Faculty of Science and Technology of
the University of Coimbra
in partial fulfillment of the requirements for the
degree of Master in Science.

Master in Physics: Nuclear and Particle Physics

Resumo

Meteorologia espacial (ME) refere-se a fenómenos que ocorrem nas proximidades da Terra controlados pelo Sol. Esses fenómenos estão relacionados com eventos oriundos da atividade solar, como erupções solares, ejeções de massa coronal e condições do meio interplanetário. A Ionosfera, parte superior da atmosfera, ionizada pela radiação solar ultravioleta, fluxos de raios-x e partículas energéticas, é fortemente afetada por ME. As alterações à taxa de ionização e, consequentemente, à densidade eletrónica alteram as condições para a propagação de ondas de rádio e desse modo, influenciam a qualidade do sinal eletromagnético que se propaga entre um dispositivo terrestre e um satélite (por exemplo, um satélite de um sistema de comunicação ou navegação). A compreensão dos processos que causam variações na densidade eletrónica e a previsão das variações do conteúdo total de eletrões (TEC) durante eventos de ME é crucial para melhorar a eficácia dos serviços dependentes de satélites.

O objetivo principal desta dissertação é o estudo das variações do TEC ionosférico nas regiões de Portugal continental e insular, em condições geomagneticamente calmas e perturbadas. Estudou-se o desempenho da análise de componentes principais na obtenção do TEC diário, confirmando-se que este método é uma ferramenta útil. Onze tempestades geomagnéticas foram analisadas no entre 2015 e 2018. Os resultados mostram variações de TEC síncronas nas diferentes localizações, para grande parte dos casos analisados. Dados observacionais foram também comparados com simulações feitas por dois modelos ionosféricos: IRI e PCA-NN. Ambos os modelos demonstraram ser adequados durante os períodos geomagnéticamnete calmos: o seu desempenho é mais fraco durante períodos geomagnéticamnete ativos, mas comparável com o desempenho de outros modelos atuais de TEC.

Abstract

Space weather (SW) refers to a range of phenomena that occur in the vicinity of Earth driven by the Sun. These phenomena are linked to solar activity events, such as solar flares, coronal mass ejections, and interplanetary medium conditions. The ionosphere, the upper part of the atmosphere ionised by the solar ultraviolet radiation (UV), X-ray (XR) fluxes and energetic particles, is strongly affected by SW. The changes in the ionisation rate and, consequently, of the electron density affect the conditions for the radio wave propagation and, therefore, influence the quality of the electromagnetic signal propagating between a ground-based device and a satellite (for example, a navigation or communication satellite systems). The understanding of processes causing variations of the electron density and forecasting of the total electron content (TEC) variations during SW events is crucial for enhancing the reliability and effectiveness of, for example, GNSS-based services.

The primary objective of this master's thesis is to study variations of the ionospheric TEC in the regions of Portugal's mainland and its insular territories during geomagnetically quiet and disturbed conditions. The performance of the principal component analysis (PCA) for obtaining daily TEC variations was studied, and this method was confirmed to be a useful tool. Eleven geomagnetic storms were analysed between 2015 and 2018. The results show synchronous TEC variations in the different locations for most of the analysed cases. Secondly, observational data was compared with simulations from two ionospheric models: IRI and PCA-NN. Both models demonstrate an adequate performance during quiet geomagnetic periods; their performance during geomagnetically disturbed periods is poorer but comparable with the performances of other state-of-the-art TEC models.

To my parents.

Agradecimentos

Tenho de agradecer imenso às instituições que acabaram por ser segundas casas ao longo de 5 anos: ao Departamento de Física, em particular a todos os professores que fizeram parte do meu percurso académico; ao Observatório Geofísico e Astronómico da Universidade de Coimbra, por facilitarem-me um espaço acolhedor para trabalhar e disponibilidade constante; e ao Instituto de Astrofísica pela vontade enorme de ter estudantes na sua equipa, proporcionando inúmeras oportunidades.

Quero dedicar particularmente este agradecimento à minha orientadora, Anna Morozova, por acolher-me neste projeto. É notável a sua dedicação durante todas as etapas que levaram à concretização deste trabalho. Quero agradecer as oportunidades que me proporcionou, como a participação em conferências internacionais, escolas de verão e a publicação de um artigo.

Não menos importante, está a minha família, à qual quero agradecer todo o apoio. Aos meus pais, que estiveram sempre presentes, nos bons e maus momentos, transmitindo-me segurança e paz. Ao meu pai, porque me inspirou a seguir este curso e deu-me muitos ensinamentos. À minha mãe, pela sua força e capacidade de superação que me inspiram e pelo interesse que mostra sempre no meu trabalho. Ao meu tio, Ricardo, pelas viagens

Table of Contents

Nomenclature

The next list describes several symbols that will be later used within the body of the document.

List of Acronyms

CME Coronal mass ejection

Dst Disturbance storm time

EEJ Equatorial electrojet

EOF Empirical orthogonal function

GNSS Global Navigation Satellite Systems

GOES Geostationary Operational Environmental Satellites

IMF Interplanetary magnetic field

IRI International Reference Ionosphere

LT Local time

NN Neural networks

NOAA National Centers for Environmental Information

PCA Principal component analysis

PC Principal component

RAEGE-Az Associação Rede Atlântica de Estações Geodinâmicas e Espaciais—Açores

RENEP Rede Nacional de Estações Permanentes GNSS

ROB Royal Observatory of Belgium

SW Space Weather

TECu Total electron content units

TEC Total Electron Content

TID Traveling ionospheric disturbance

UTC Coordinated Universal Time

UV Ultraviolet Radiation

XR X-Ray

List of Physical constants and Solar-Terrestrial parameters

$\mu_0 = 4\pi \times 10^{-7}$ H/m magnetic constant or permeability of free space

c=299792458 m/s Speed of light

e=1.602176634×10^{-19} C Elementary charge

G=6.67430×$10^{-11}m^3/kgs^2$ Gravitational constant

$k_B = 1.380649 \times 10^{-23}J/K$ Boltzmann Constant

$M_\oplus = 5.97219 \times 10^{24}$ kg Earth mass

$M_\odot = 1988500 \times 10^{24}$ kg Solar mass

m_e=9.10938356×$10^{-31}kg$ Electron mass

m_p=1.67262192×$10^{-27}kg$ Proton mass

1 AU = 1.5×10^{11} m 1 Astronomical Unit

$R_\oplus$=6371 km Earth Radius

$R_\odot$=695700 km Solar Radius

List of symbols

σ (std) Standard deviation

C Coulomb (unit of elementary charge)

H henry (unit of electrical inductance)

List of Tables

List of Figures

INTRODUCTION 1

(NOUN) **Space Weather:** *conditions in the region of space close to the Earth, especially the presence of electromagnetic radiation and charged particles emitted by the Sun, that can affect human activity and technology. - The Oxford English Dictionary*

Auroral sights have been recorded in many cultures worldwide for over 4000 years and started being studied in the 17th century. However, it was only in the 19th century that auroral events began to be related to events on the Sun, especially the appearance of sunspots and solar flares [1]. On 1st of September 1859, auroras were seen as far down as Puerto Rico, and significant telegraph damage was reported. This had been an outcome of one of the most significant geomagnetic storms recorded, and it was named after R. Carrington, who observed and reported a solar flare that was a source of this storm [2].

SW events affect the upper part of the Earth's atmosphere, the ionosphere. In 1839, C. Gauss and B. Stewart first introduced the idea of the ionosphere by stating that there should be an electrically conducting region in the Earth's atmosphere [3]. Later, contributions to the knowledge of this layer were made by A. Kennely and O. Heaviside, who postulated its existence and E. Appleton, who confirmed it experimentally.

The ionosphere plays a considerable role in today's technological society. Radio and global navigation satellite systems (GNSS) signals travel through this layer. Changes in the electron density due to SW events affect the conditions for the radio wave propagation. When the signal quality between a ground-based device and the GNSS satellites is affected, it may compromise the performance of GNSS-based services. These include safety operations of crewless vehicles for exploration and surveillance in remote areas, navigation of autonomous transportation systems for passengers and goods, precise landing procedures for commercial

✦✦✧✦✦

aviation, and GNSS-assisted positioning during rescue operations. Portugal (between $\sim 30°$ and $\sim 50°$N and from $\sim 30°$ to $\sim 6°$W) is located in a critical region as it lies on the western borders for the coverage of the European Geostationary Navigation Overlay (EGNOS), a satellite-based augmentation system (SBAS) for GNSS [4]. Understanding and forecasting of total electron content (TEC) variations during potentially dangerous SW events is crucial for enhancing the reliability and effectiveness of these GNSS-based services. Working towards that goal, the main objective of this master thesis is to comprehend the key characteristics of ionospheric variability during space weather events and quiet geomagnetic time intervals in the Portuguese territory. Furthermore, it aims to identify similarities and differences in these characteristics between the continental and oceanic Portuguese regions. The second purpose of this work is to compare observational TEC data with simulations made by a state-of-the-art ionospheric model, IRI and a new model, PCA-NN, developed at IA-U.Coimbra group in the frame of the PRIME project.

Chapter 1 (Introduction) explains the main drivers of SW. A small introduction to plasma physics and the mathematical tools is given, followed by a general introduction to the Sun, the solar-terrestrial environment and the magnetosphere. The ionosphere and its features are explained in detail. Then, in Chapter 2 (Mathematical methods), the statistical and mathematical tools used in this work are described. Chapter 3 (Data sources and description) describes the data used in this work. In Chapter 4 (Daily TEC variations), TEC during quiet geomagnetic time intervals is analysed using a standard procedure and the principal component analysis. In Chapter 5 (TEC response to space weather), multiple geomagnetic storms and flare events are studied for the locations covered. A detailed analysis of the TEC variability over these disturbed time intervals is presented. In Chapter 6 (Modeling TEC), two models of TEC are compared to the observed TEC data during the quiet and disturbed geomagnetic time intervals. The main conclusions are summarised in the final

chapter (Chapter 7, Conclusions and Outlook), together with an outlook for further studies of TEC for the Portuguese territory.

Personal contribution   The whole data analysis (Chapters 4,5 and 6) was done by me, this includes: the selection of the time intervals for the study (quiet days, geomagnetic storms and solar flare events) using the Dst index and solar flares data (see Chapter 3); the phyton scripts used for the analysis of the daily TEC variations, PCA, statistical analysis and the three TEC parameters used to study the geomagnetic storms' effect on TEC (Chapters 4 and 5); the IRI model TEC values, obtained from running IRI for the selected days in the online portal; the RMSE for IRI and PCA-NN models (see Chapter 6). This work has the following contributions: TEC data series from different GNSS receivers (see Chapter 3) was already processed and calibrated. PCA-NN TEC values were given in the requested time intervals.

1.1   A theoretical background on plasma physics

Plasma is a gas composed of charged particles that behave like a fluid. Plasma's temperature, T, must be high enough and the density, n, low enough so that it meets the condition $N_D = 1.38 \times 10^6 \sqrt{T^3/n} >> 1$. Also, the frequency of particles' oscillation, ω and mean time between collisions, τ must be $\omega\tau > 1$ so that collisions with neutrals do not happen too frequently (see Appendix A). The Sun, the interstellar space, and the upper atmosphere are in this fourth state of matter, so the properties of plasma relevant for the understanding of these physical systems are described [5].

Behaviour of a charged particle in the electromagnetic field

The motion of a charged particle (velocity $\mathbf{v}$) of a mass m and charge q in a magnetic field $\mathbf{B}$ and electric field $\mathbf{E}$ is given by the Lorentz equation (non-electromagnetic forces and collisional terms are neglected [2]):

$$m\frac{d\mathbf{v}}{dt} = q(\mathbf{E} + \mathbf{v} \times \mathbf{B}) \tag{1.1}$$

And the changes of the electric and magnetic fields are described by Maxwell's equations [2]:

$$\nabla \cdot \mathbf{E} = \frac{\rho}{\epsilon_0} \qquad \text{(Gauss's law)} \tag{1.2}$$

$$\nabla \cdot \mathbf{B} = 0 \qquad \text{(Gauss's law, no magnetic monopoles)} \tag{1.3}$$

$$\nabla \times \mathbf{E} = -\frac{\partial \mathbf{B}}{\partial t} \qquad \text{(Faraday's law)} \tag{1.4}$$

$$\nabla \times \mathbf{B} = \mu_0 \mathbf{J} + \mu_0 \epsilon_0 \frac{\partial \mathbf{E}}{\partial t} \qquad \text{(Ampère-Maxwell law)} \tag{1.5}$$

The velocity of a particle in an uniform electromagnetic field can be split into perpendicular ($v_\perp$) and parallel ($v_\parallel$) components with respect to the magnetic field $\mathbf{B}$ direction. The perpendicular component is a combination of a time-varying component $\tilde{\mathbf{v}}_\perp$ and a constant component $\mathbf{v}_E$ [2, 6]. Two types of perpendicular motion occur :

1. *Gyration about the magnetic field*

$$\frac{d^2\tilde{\mathbf{v}}_\perp}{dt^2} = \left(\frac{qB}{m}\right)^2 \tilde{\mathbf{v}}_\perp \tag{1.6}$$

The gyration is a simple harmonic oscillator movement with a "gyro-frequency" of $\Omega = |qB/m|$ (rad/s). The particle moves in a circle with radius $r_L = \frac{v_\perp}{\Omega}$, called

the Larmour radius. The movement is charge dependent: positive charged particles gyrate clockwise, and negative ones go anti-clockwise, relative to **B** (if viewed with the magnetic field pointing toward the observer).

2. $\boldsymbol{E} \times \boldsymbol{B}$ *drift*

$$\mathbf{v}_E = \frac{\mathbf{E} \times \mathbf{B}}{B^2} \tag{1.7}$$

This is the drift motion perpendicular to **B** and **E**. Particles drift to other forces as well.

Magnetic mirrors

The magnetic moment (See Appendix A) is an adiabatic invariant, for slow variations of the magnetic field's strength in relation to the gyro period. When a particle moves with increasing magnetic field intensity, the Larmour radius and perpendicular velocity increases. Because energy is conserved, the parallel velocity decreases until eventually it reaches 0, and the particle changes direction. This motion is called a "magnetic mirror" [6].

Vlasov Theory

Since space plasma has high temperature and low in density, let us assume that it is collisionless. The Boltzmann equation for continuous electric fields reduces to the Vlasov equation, in the absence of the collision term [1]:

$$\frac{\partial f}{\partial t} + \mathbf{v} \cdot \nabla f + \mathbf{a} \cdot \nabla_v f = 0 \tag{1.8}$$

From the distribution function $f(\mathbf{r}, \mathbf{v}, t)$, one can get the macroscopic variables for plasma (see Appendix A). The conservation laws (Magnetohydrodynamics' (MHD) equations) are

obtained by taking this equation's moments (integration over the velocity space for the powers of the velocity).

Electromagnetic wave propagation in a partially ionized plasma

The electromagnetic waves propagation (in space, $\mathbf{r}$ and in time, t), transverse to the direction of the electric field $\mathbf{E}$, at an angular frequency ω is given by [6]:

$$\mathbf{E}(\mathbf{r}, t) = E_0 \ e^{i(\mathbf{k} \cdot \mathbf{r} - \omega t)} \tag{1.9}$$

where E_0 is the wave amplitude, $\mathbf{k}$ is the wave vector (direction of the wave), and ω is the angular frequency of the wave in vacuum. Treating plasma as a dielectric medium [6], the motion of the electrons (mass m_e, velocity v_e and charge e) is described by:

$$m_e \frac{d\mathbf{v}_e}{dt} = -e\mathbf{E} \tag{1.10}$$

Working with Maxwell equations (Faraday's and Ampère-Maxwell's laws), one finds [6]:

$$\mathbf{k} \times (\mathbf{k} \times \mathbf{E}) + \frac{\omega^2}{c^2}\epsilon(\omega) = 0 \tag{1.11}$$

which describes the propagation of electromagnetic waves in vacuum, c is the velocity of light, and $\epsilon(\omega)$ is the dielectric constant ($\epsilon = 1$ in vacuum). For plasma $\epsilon(\omega)$ is written in terms of the angular frequency of the wave in plasma ω_p:

$$\epsilon(\omega) = \left(1 - \frac{\omega_p^2}{\omega^2}\right) \tag{1.12}$$

The relationship between the wave vector and the frequency is given by:

$$\omega^2 = c^2 k^2 + \omega_p^2 \tag{1.13}$$

here, $k = |\mathbf{k}|$. The phase velocity of an electromagnetic wave in plasma is $v_f = \omega/k > c$ (Equation 1.13), but the group velocity is $v_g = \partial\omega/\partial k = c^2/v_f < c$. The electromagnetic wave has a critical frequency (cut-off frequency) ω_p for plasma (when $\omega = \omega_p$, $k = 0$), and its propagation is damped. The attenuation is proportional to $|k|^{-1}$. The critical frequency changes in response to the electron density n_e of the plasma [7]:

$$\omega_p^2 = \frac{n_e e^2}{\epsilon_0 m} \tag{1.14}$$

For example, for $n_e = 10^4/cm^3$, the wave propagating wave is fully damped for $\omega = \omega_p = 10^7/s$, corresponding to a radio wave frequency.

1.2   The Sun

The Sun is a 4.5 billion years old, yellow G-type star (surface temperature between 5000-6000 K) [8] at $\sim$ 1.5 x 10^{11} m (1 astronomical unit, 1 AU) from the Earth. It is composed of ionised gas (hydrogen (90%) and helium (10%)) and has 330 thousand times the mass of the Earth [6]. Table 1.1 summarises some solar parameters as a reference. The Sun is dynamic, and different structures on its surface have been documented since the beginning of the 16th century. The Sun is the driver of SW phenomena felt and seen on Earth [9].

Table 1.1: Main solar bulk parameters, modeled values for the core, and atmospheric values [10].

Spectral type	G2 V
Mass (10^{24} kg)	1988500
Volumetric mean radius (km)	695700
Mean Distance from Earth (10^6 km)	~ 1.5
Central temperature (K)	1.571×10^7
Central pressure (g/cm^2)	2.477×10^{17}
Central density (g/cm^3)	1.622×10^2
Absolute magnitude	+4.83
Major elements	H - 90.965%, He - 8.889%
Luminosity (10^{24} J/s)	382.8

The structure of the Sun

The Sun is divided into spherical shells, as shown in Figure 1.1.
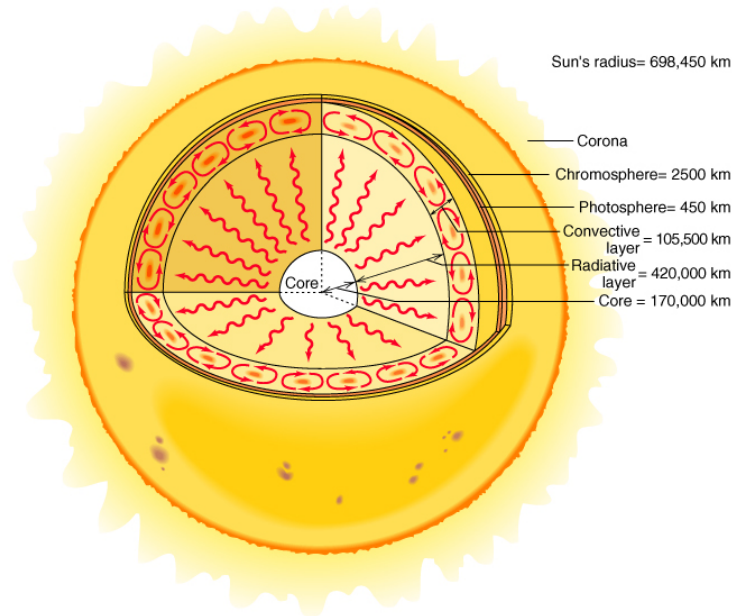
Figure 1.1: Schematic diagram of Sun's layers and respective thickness in km. The centre shows the core, radiative, and convective layers. The right side shows the photosphere, chromosphere, and corona [11].

In the **core** (0.2 $R_\odot$), energy is produced at a temperature of 15×10^6 K by nuclear fusion (Figure 1.2). During the process, 0.7% of the mass of the reactants is converted to energy [2].

Wrapping the core, there is the **Radiative zone**, where the energy, carried by photons, propagates by radiative diffusion. A turbulent convection occurs in the next region, the **Convective zone**. Moving plasma is one of the sources for the solar magnetic field [9].
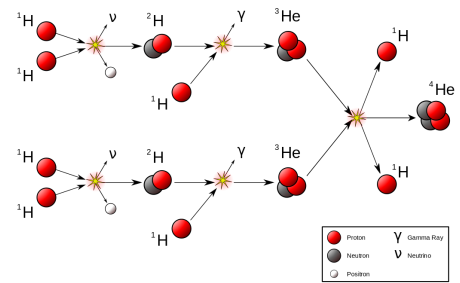
Figure 1.2: Diagram of a proton-proton reaction chain with deuterium and helium as products [12].

Between the radiative and the convective zone, there is a layer of thickness of 0.02 $R_\odot$ called the **solar tacholine**. This layer divides the region where the Sun rotates uniformly (rigid body) from the outer part of the Sun, which rotates deferentially. In the latter, rotation is slower near the poles and faster near the equator [13]. The steep velocity gradients in the tacholine are responsible for the **solar dynamo**, which dominates the production of solar magnetic fields [14].

The Sun's magnetic field can be measured using a phenomenon called Zeeman splitting: the division of a spectral line into several components in the presence of a magnetic field. Depending on the atom, the difference between the split lines can tell how strong the magnetic field is. The direction of the field can be deduced from an analysis of the Zeeman effect on the light with different polarization. The evolution of magnetic fields is described by MHD equations (Appendix A).

Solar atmosphere

The **Photosphere** (100 km) is often referred to as the "visible surface" of the Sun. It is transparent to photons (mostly in visible light wavelengths). Activity from the inner layers

manifests in the form of visible features [14].

In the Convective zone, the plasma's convective motion forms a pattern seen on the photosphere in small and large sizes, called **granulation**. This is a persistent feature of the quiet Sun [2].

The structures that are the most known manifestation of the solar activity are the **sunspots**. Magnetic flux tubes below the solar surface are bent and stretched due to differential rotation (Figure 1.3 left and centre). Mass and flux conservation make the tubes thinner, increasing the magnetic field density. As pressure between the tubes and the plasma surrounding it has to be balanced, the tubes rise and break in the surface, creating a pair of sunspots of the opposite magnetic polarity (Figure 1.3 c)). A sunspot is seen as a darker region called the umbra, where the magnetic field is predominantly vertical and more intense. Strong magnetic field inside the dark region inhibits convection, decreasing temperature in that region. Penumbra is the lighter region around the umbra and is characterised by weaker, horizontal magnetic fields (Figure 1.4) [6].
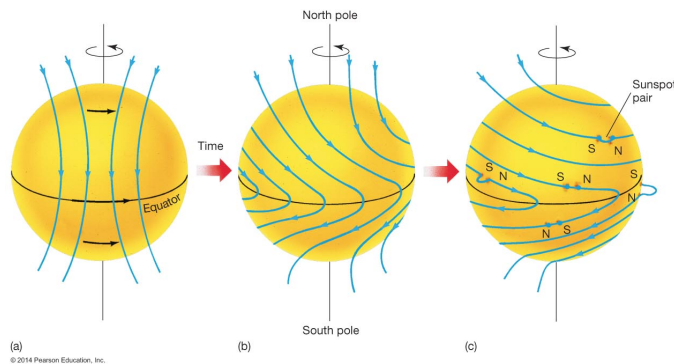
Figure 1.3: Schematic diagram of the formation of sunspots [15]. Left: simple magnetic field of the Sun. Centre: differential rotation stretches the field lines. Right: filed lines break at the surface, forming a pair of sunspots of opposite polarity.

Sunspots' observation over several centuries led to a conclusion that the Sun has an $\sim$ 11 year activity cycle: when the activity is at its highest, the number of sunspots is higher (the sunspot cycle, Figure 1.5 bottom). Additionally, in each cycle, the magnetic polarity near the solar poles inverts (magnetic north switches with magnetic south). Furthermore, when

Figure 1.4: A close-up on the Sun (Hα) shows the regions of a sunspot (umbra and penumbra) and the granulation pattern around them [16].

plotting the latitudes of the appearance of sunspots on the solar surface as a function of time, a pattern is seen (the so-called butterfly diagram, Figure 1.5 top). At the beginning of each cycle, sunspots appear at around $35°$ from the equator, and during the cycle, the latitude of new spots decreases.
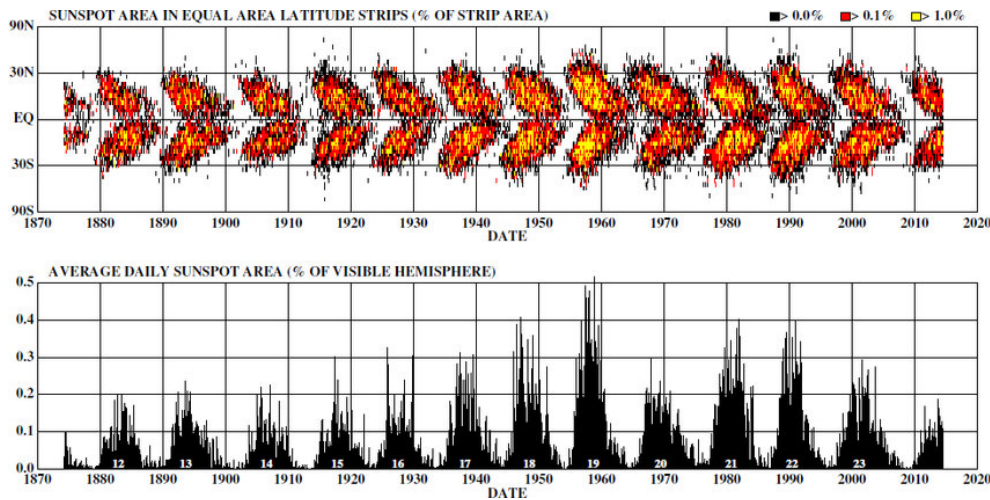
Figure 1.5: 11-year solar cycle from 1874 to present. Top: The Butterfly diagram, sunspot latitude vs. time. Bottom: Sunspot number over time [17].

In the **Chromosphere**, temperature increases abruptly in a $\sim$100 km distance, from 4500 K in the photosphere to 25000 K [1]. The heat from the upper regions of the solar atmosphere (its production is explained in the next paragraphs) flows down, increasing the temperature in the Chromosphere. The density of plasma increases, and it may get trapped

in the magnetic field lines that are rising through the surface, creating a loop structure called a **filament** or a **prominence** [6].

The **Corona** is the outer part of the solar atmosphere. Here, plasma is collisionless and follows the Sun's magnetic fields. If the field lines are closed, plasma gets trapped in a **coronal loop**; if they are open (closing very far away), the plasma escapes, creating a **coronal hole**.

Magnetic field loops may become unstable and more stretched, causing more tension. When a field line breaks, it will try to reconnect, releasing a large amount of energy that heats the solar atmosphere (the reconnection process will be explained in Section 1.3). These quick electromagnetic radiation emissions are called **solar flares**, and they energise the local plasma particles.

Another feature of the activity in the Sun are **coronal mass ejections** (CME), which can result in expulsions of up to 10^{13}kg of solar mass at velocities up to 2000 km/s. The mechanisms associated with a CME are still debated; it can be associated with flares and filament eruptions [6].

Solar wind is an extension of the solar atmosphere. To balance the pressure between the solar surface and the interplanetary medium, a supersonic flow of plasma is constantly released from the Sun, governed by the MHD equations (see Appendix A). Based on a typical velocity, two types of solar wind are distinguished: a slower component of the solar wind (250 to 400km/s) originates from streamers associated with coronal loops; a fast solar wind (400 to 800 km/s) comes from the coronal holes. In either case, the solar wind is hot and conductive, carrying the solar magnetic field with it, creating the Interplanetary Magnetic Field (IMF) [1].

1.3   Earth's magnetosphere

The Earth's interior is composed of two layers with extreme pressures and temperatures: the inner and the outer cores. In the outer core, the magnetic field is generated by a dynamo mechanism [18]. It contains liquid metals (electrically conducting) in motion due to thermal convection. The outer core rotates due to the Coriolis effect generated by the Earth's rotation. The rotary motion of the fluid induces the magnetic field (see Equation A.15) [18].

In the absence of the solar wind, the magnetic field around Earth would resemble that created by a bar magnet, a dipole magnetic field, with magnetic field lines entering on the northern and leaving on the southern magnetic pole. The axis of this dipole magnet, as is shown in Figure 1.6, is not aligned with the Earth's rotation axis (making an angle of $\sim 23°$).

Solar plasma, carrying mass, momentum and magnetic field, escapes from the solar corona into the interplanetary space at supersonic speed. It interacts with obstacles like the Earth's magnetic field, (exerting a force on it). The plasma encloses the Earth in a cavity controlled by the magnetic field, the magnetosphere [6].
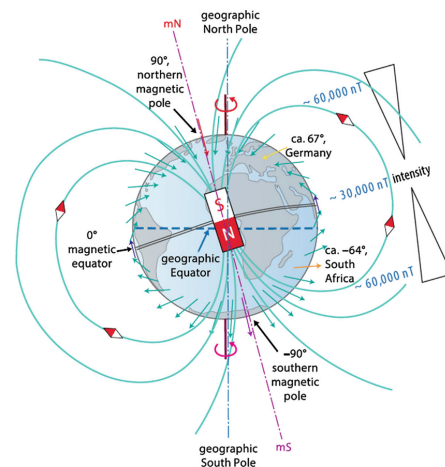
Figure 1.6: Earth's geomagnetic field according to dynamo theory [19].

Structure and currents

The magnetosphere shape is schematically represented in Figure 1.7 where its main structures are identified.

When the supersonic solar wind encounters the Earth's magnetic field, a **bow shock** is created, and the solar wind slows down to sub-magnetosonic flow and has its momentum converted into thermal energy. Sudden variations in the solar wind speed and direction of the embedded magnetic field are associated with disturbances caused by solar events, impacting the shape of the magnetosphere [20].
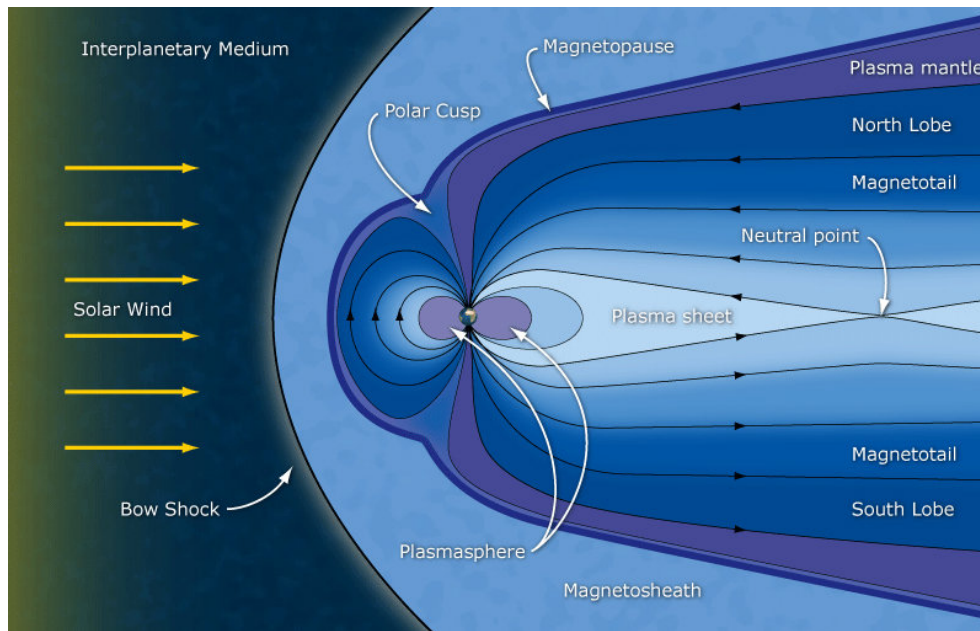
Figure 1.7: Longitudinal cut of the Earth's magnetosphere showing its structure [21].

The slowed plasma forms a region between the bow shock and the magnetosphere, the **magnetosheath**. At the **magnetopause**, the intensity of the magnetic field B increases. The Earth's magnetic field dominates the plasma's motion in the magnetosphere, so it flows along the magnetic lines, reaching the **magnetotail**. The magnetic pressure inside the

magnetopause p_B [20],

$$p_B = \frac{B^2}{2\mu_0} \tag{1.15}$$

must be equal to the outside pressure, which is the dynamic pressure of the solar wind p_{sw}, defined by the solar wind's mass density ρ_{sw} and velocity u_{sw} [20]:

$$p_{sw} = \rho_{\mathrm{sw}} u_{\mathrm{sw}}^2 \tag{1.16}$$

The Earth's magnetic field intensity is inversely proportional to the cube of the radial distance r:

$$B(r) = B_E \left(\frac{R_E}{r} \right)^3 \tag{1.17}$$

where R_E and B_E are the Earth's radius and the magnetic field felt at the equator. The magnetopause changes size and location to balance the pressures. Combining equations 1.15, 1.16 and 1.17, the radius of the magnetopause r_{mp} changes depending on the solar wind conditions.

$$\frac{r_{\mathrm{mp}}}{R_E} = \left(\frac{B_E^2}{2\mu_0 \rho_{\mathrm{sw}} u_{\mathrm{sw}}^2} \right)^{1/6} \tag{1.18}$$

This creates a current that distorts the Earth's dipole magnetic field B_E. As the magnetic field within the boundary is oriented predominantly northward, the magnetopause (or the Chapman-Ferraro) current flows from dawn to dusk across the equatorial magnetopause and from dusk to dawn across the high-latitude magnetopause tailward of the cusp openings (see Figure 1.8).

Magnetic reconnection in the day-side magnetosphere is a process that connects the interplanetary magnetic field (IMF) to the geomagnetic field and allows mechanical energy of the flow to be transmitted into the magnetosphere and ionosphere. If the direction of the

15
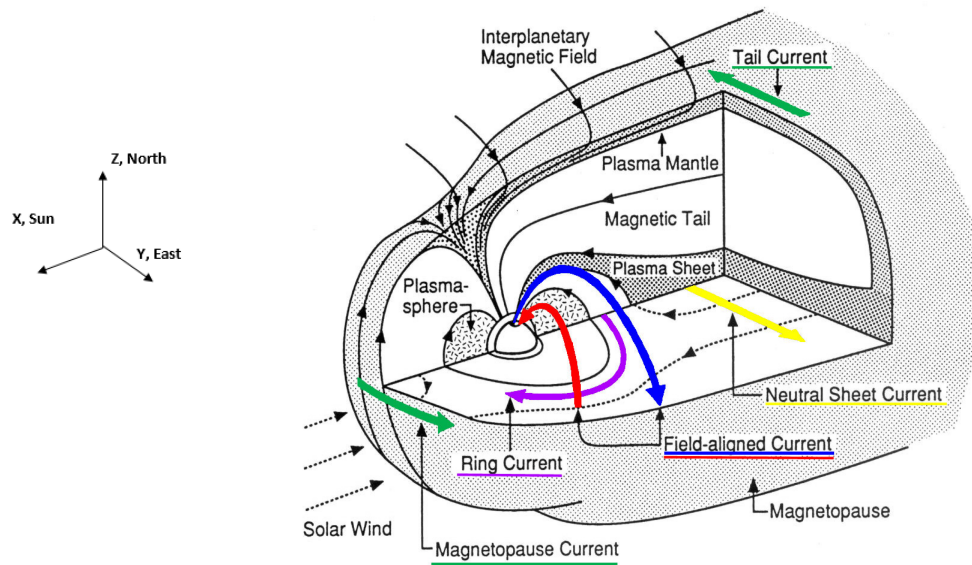
Figure 1.8: Cut diagram of Earth's magnetosphere: magnetic topology of the main structures, the coupling to the magnetosheath, and main current system (adapted from [6]).

solar wind's magnetic field is opposite to that of the Earth's magnetic field, the reconnection between a magnetic field line of the solar wind and a magnetic field line of the magnetosphere occurs at the front or in the lobes. This process is represented in Figure 1.9 (on the left side of the picture). Reconnection allows the magnetic fields to relax to a lower energy configuration, and the energy released enters the system through the plasma.
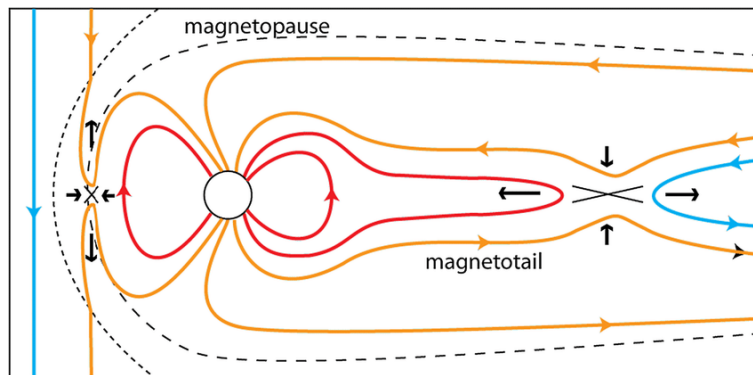
Figure 1.9: Magnetic reconnection in the magnetopause, day side magnetosphere (left cross) and in the magnetotail, night side magnetosphere (right cross) [22].

The magnetic field is pulled antisunward after interacting with the magnetosphere in the front. The magnetotail comprises two adjacent magnetic flux lines of antiparallel field (south and north lobes). The lobes are separated by a **plasma sheet**, an area where the magnetic field is weaker, and reconnection may occur in the **neutral point** between different polarity horizontal field lines (Figure 1.9, right side of the picture). In the tail, two currents cross the magnetopause, one above and one below the regions of the tail. A **neutral sheet current** flows in the centre of the magnetotail and crosses the plasma sheet from dawn to dusk. Reconnection in the tail causes substorms and geomagnetic disturbances registered mainly in the polar regions. Induced kinetic motion in the magnetospheric plasma creates current or enhances the already existing currents [6].

The **plasmasphere** is located inside the magnetosphere and contains dense cold plasma of ionospheric (atmospheric) origin. The areas where the magnetic field lines leave the Earth, and change their configuration from the dayside to the night side are called **polar cusps**, here the field lines bend due to the stress. Spiralling charged particles around magnetic field lines create the **field-aligned currents**. The pressure of the solar winds is transmitted from the magnetosphere to the ionosphere. When an intense dayside reconnection event occurs, the polar cusps' field lines move to lower latitudes [2].

Particles trapped in the dipole magnetic field gyrate around the magnetic field lines, bouncing from north to south. The particles drift because the magnetic field lines are curved and do not have the same magnitude everywhere. Protons or other positive ions drift westward, and electrons drift eastward (see Section 1.1). This creates an equatorial **ring current** system that strongly affects the magnetic field variations. This system has at least two ring currents (the electron and the proton ring currents). However, there is a local time asymmetry: some of the plasma stays on the night side, and a partial ring current is formed, Figure 1.10. The partial ring current exhibits the most drastic intensification as the disturbances

increase. The net current flows around the Earth clockwise and depresses the main magnetic field at the Earth's surface [23].
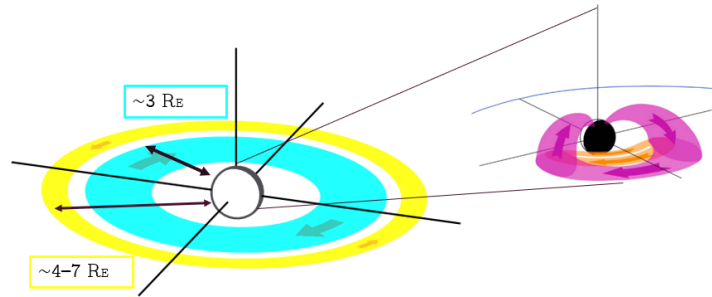
Figure 1.10: The two symmetric ring currents (eastward and westward, in yellow and blue, respectively), including their relative mean radius. Partial ring current that connects to the field-aligned currents (in pink) (adapted from [23]).

1.3.1 Geomagnetic storms

Geomagnetic storms are related to events originating in the Sun, namely CMEs, solar flares, and coronal holes (referred to in section 1.2), that release fast and dense plasma (increased solar wind speed). The pressure from the flow causes considerable compression on the dayside magnetosphere, moving the magnetopause closer to the Earth. Due to this process, the magnetopause current is enhanced. A geomagnetic storm often starts with a sharp increase of the horizontal geomagnetic field's component (H), a so-called sudden storm commencement.

When the solar wind's magnetic field is intense and southward for several hours [24], reconnection is more effective and prolonged. Strong reconnection combined with intense and long-lasting solar wind parameters (solar wind speed, pressure, and density of the flow) drive more energy to the tail, heating the plasma on the magnetosphere [25]. The charged particles entering the inner magnetosphere enhance the ring current, inducing a decrease in

the H component of the magnetic field, which defines the main phase of a geomagnetic storm. The main phase lasts several hours, after that, the Earth's magnetic field returns to its initial conditions during the recovery phase, when the energy is lost by charge exchanging with the neutrals [20]. The last phase can take several hours to several days, depending on the solar wind and magnetospheric conditions.

The Dst index as an indicator of a geomagnetic storm

The disturbance storm time index (Dst) is a geomagnetic index used to monitor perturbations of the H component of Earth's magnetic field. The currently accepted procedure to calculate Dst requires four (N) observatories at quasi-equatorial latitudes. It is calculated using the measured H component of the magnetic field, an averaged value of H for the quietest time periods, H_q and the magnetic latitude of the stations, ϕ [6]:

$$\text{Dst} = \frac{1}{N} \frac{\sum (\text{H} - H_q)}{\cos(\phi)} \tag{1.19}$$

Figure 1.11 (bottom) shows the typical Dst variations during a geomagnetic storm. The large depression of Dst is the most prominent feature of a storm and coincides with the southward Bz of the IMF(Figure 1.11, top).

Besides Dst, there are other geomagnetic storm indicators. A more recent index, SYM-H, is similar to Dst in its calculation, however, it has a 1-min resolution [6]. The Kp index is a three-hour index calculated using geomagnetic data from 13 mid-latitudinal stations [27]. AE (auroral electrojet intensity), AL (auroral low), and AU (auroral upper) are 1-minute indexes from stations at the auroral regions [28]. They are often used for the characterization of substorms.
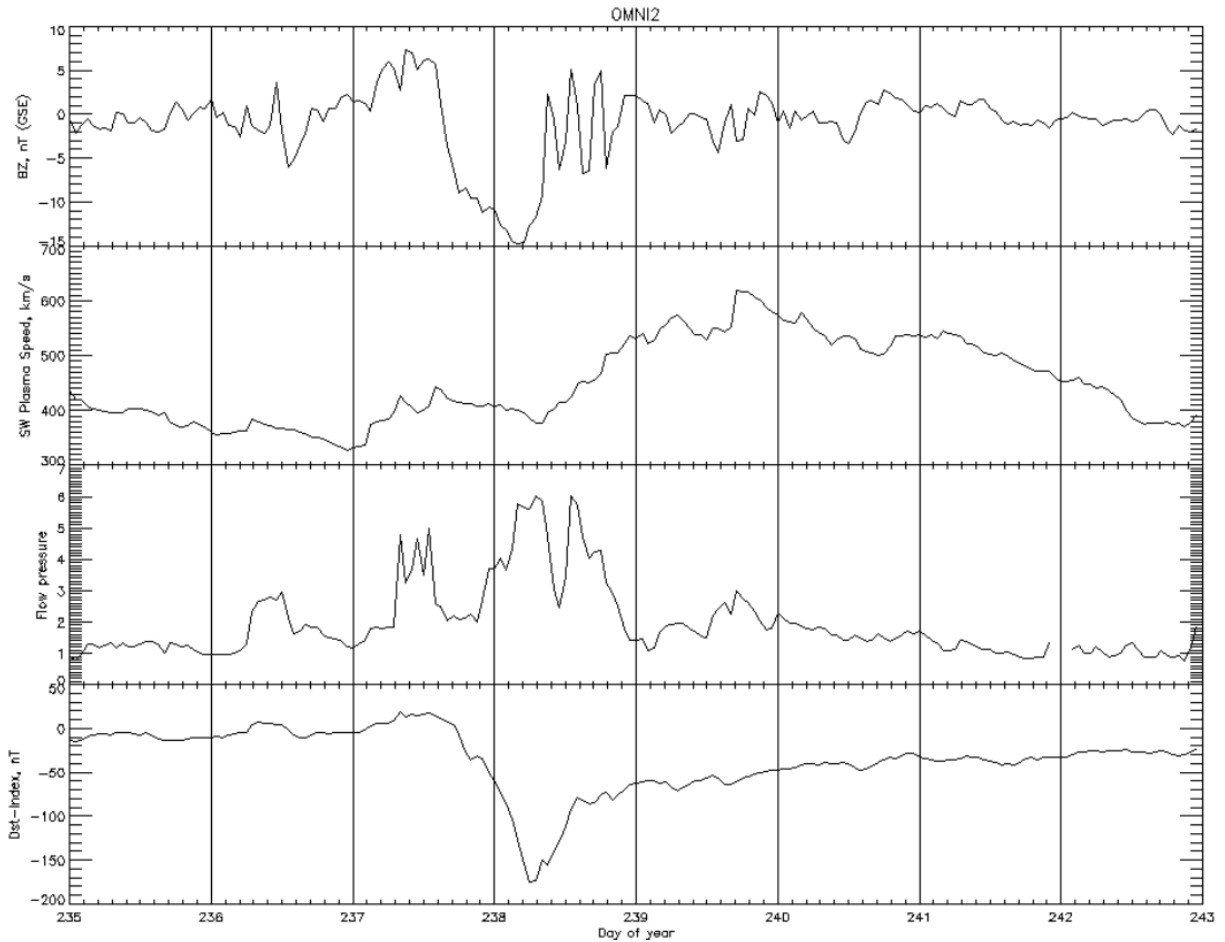
Figure 1.11: Example of a geomagnetic storm occurring on August 26th 2018. Z coordinate of the IMF in nT (first plot), speed of the flow in km/s (second plot), pressure of the flow in nPa (third plot), Dst index in nT (fourth plot) [26].

1.4 The ionosphere

The ionosphere is the region of an atmosphere where free electrons and ions are present. It is a conducting region with a system of electric currents high above the ground. The Earth's ionosphere is located between the middle mesosphere and the beginning of the exosphere, from ~ 60 to more than 1000 km. [1]

The air molecules and atoms are ionised mainly by the solar radiation, thus, the iono-

20

sphere is constantly changing. At sunrise, energetic photons from the Sun split molecules into electrons and ions. At around solar noon, the density of electrons and ions is at its maximum. At night, the ionosphere thins out as the ionised particles from the day recombine into neutrals, creating daily electron density changes. Since the ionosphere is a part of the Earth's atmosphere, it is affected by atmospheric winds, waves and tides. Furthermore, the ionosphere reacts to changes in the magnetic and electric conditions outside the Earth's atmosphere. Thus, regular weather and space weather impact the ionosphere, making it difficult to forecast the conditions in this region at a given time.

1.4.1 Formation of an ionosphere

Any planetary body with a neutral atmosphere and an ionisation source may have an ionosphere. The main processes for ionisation to occur are photoionisation (photons from the Sun), particle precipitation (ionising particles from the Sun, magnetosphere, or cosmic rays), and collisions between ions, electrons, and neutrals [2].

Photoionisation

Photoionisation dominates the dayside ionospheric production. Assume an atmosphere with only one chemical species, gravitationally distributed, and where the absorption of solar radiation is the dominant process. The solar flux penetrates this atmosphere in a straight line s (Figure 1.12), which is the line of sight, and it is absorbed by the neutral species. Its intensity I is attenuated along s following the em-
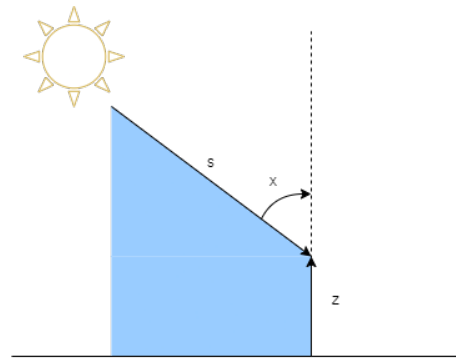
Figure 1.12: Illustrating the solar zenith angle x, line of sight s, altitude z and the atmospheric column density along s in blue (adapted from [2]).

pirical relationship (Beer-Lambert law) [6]:

$$dI(s, \lambda) = -\sigma_a(\lambda)n(z)I(s, \lambda)ds \tag{1.20}$$

where $\sigma_a(\lambda)$ is the absorption cross section and $n(z)$ is the density of that species with height z. Introducing the solar zenith angle x (Figure 1.12), Equation 1.20 is integrated over z:

$$I(z, \lambda) = I_\infty(\lambda)e^{-\tau} \tag{1.21}$$

where I_∞ is the intensity of the flux at the top of the atmosphere and τ is the optical depth.

$$\tau = \int_\infty^{z'} \sigma_a(\lambda)n(z)\frac{ds}{dz}dz \tag{1.22}$$

$$= \sigma_a n(z) Chap(z, x, H_i) \tag{1.23}$$

The parameter τ can be seen as the power of the solar flux radiation to produce ionisation at an altitude z. The Chapman function $Chap(z, x, H_i)$ is equivalent to the ionisation produced along the column density from Figure 1.12 (blue area). H_i is the neutral gas scale height.

The components of the atmosphere are separated by their mass m_i in a uniform gravity field $g(z)$. The density $n(z)$ at altitude z is given by the barometric equation at temperature T_i [6]:

$$n(z) = n(z_0) \exp - \left(\frac{z - z_0}{H_n} \right) \tag{1.24}$$

Thus, $n(z)$ decreases exponentially with altitude at a constant characteristic length given by the neutral gas scale height $H_i = \frac{k_B T_i(z)}{m_i g(z)}$ (k_B is the Boltzmann constant).

The integration of Equation 1.22 is not easily analytically solvable in spherical geometry. If we assume a plane and horizontally stratified atmosphere ($dz = -cos(x)ds$) a simple expression for the Chapman function appears: $Chap(z, x, H_i) = H_i/cos(x)$. In this case, Equation 1.22 reduces to [6]:

$$\tau(z, \lambda, x) = sec(x) \sum_i n_i(z)\sigma_{ia}(\lambda)H_i \tag{1.25}$$

which is valid for latitudes $< 85°$. The expression accounts for an atmosphere with more than one species i. The production function of ions due to photoionisation is given by [6]:

$$P_c(z, x) = I(z, x)\eta\sigma_a n(z) = I_\infty\eta\sigma_a n(z)e^{-\tau} \tag{1.26}$$

here η is the probability of an absorbed photon result in the production of an ion-electron pair.

The ion production function, in terms of τ and $n(z)$, is given by the Chapman production function [6]:

$$P_c(z, x) = P_{c_0} \exp\left[1 - \frac{z - z_0}{H_i} - exp\left(\frac{z_0 - z}{H_i}sec(x)\right)\right] \tag{1.27}$$

P_{c_0} is the production function P_c for an altitude corresponding to the unit optical depth (τ = 1, and $x = 0°$). The plot of the Chapman production function for different x can be seen in Figure 1.13.

Electrons are created through photoionisation and are lost in recombination reactions with neutrals or other ions. Assuming a quasi-neutral plasma ($n_e = n_i$), Equation 1.27 can be written as linearly dependent on its electron density. The electron density expression

predicts the layers of the ionosphere resulting from photoionisation:

$$n_e(z, x) = \left(\frac{P_{co}}{k_d}\right)^{1/2} \exp\left\{\frac{1}{2}\left[1 - \frac{z - z_0}{H} - \exp\left(\frac{z_0 - z}{H}\right)\sec(x)\right]\right\} \tag{1.28}$$

here k_d is the ion–electron recombination rate.
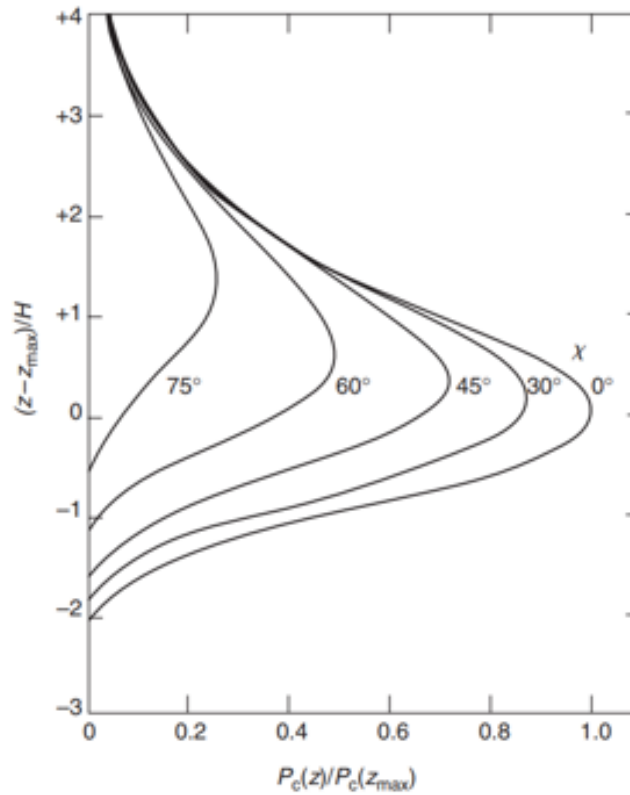
Figure 1.13: Plot of the normalized Chapman production function vs z/H [1]. Different x present different maximum rates.

Ionization through particles (particle precipitation and collisions)

The ionospheric layers thin out at night but do not entirely vanish due to other processes, such as, the transport of energetic particles through the atmosphere.

Particle interactions occur through Coulomb collisions, elastic ion-neutral collisions, and collisions between neutral species. These collisions cause ionisation by impact. The ionospheric properties are best described using the Vlasov equation 1.8, with the additional collision term $\delta f/\delta t$ (Boltzmann Equation). Integrating the Boltzmann equation over the velocity space gives the transport equations [1].

When an electron-ion pair is created, the electron absorbs most of the energy exceeding the ionisation threshold $\Delta\epsilon$ (35 eV is usually the mean value for electron precipitation). An electron with energy E produces E/$\Delta\epsilon$ ion-electron pairs before its energy is fully depleted.

Proton precipitation is rare because protons are stopped at higher altitudes. Electrons may trigger a cascade mechanism where secondary (and more) ionisation occurs as the electron from the new pair has enough energy to precipitate. Particles can come from the magnetosphere, where they are trapped in a region called the Van Halen radiation belts.

Ionization by precipitating energetic particles is an important ionization source at higher latitudes, while at middle latitudes, the region of interest of this work, the photoionisation is dominant.

1.4.2 Structure and dynamics of the ionosphere

During the daytime, electrons are produced by photoionisation and lost in recombination reactions. The electron density varies with height and solar zenith angle. It is expected a parabolic shape of the density as a function of the altitude because the maximum production coincides with the peak density of the layer (a Chapman layer approximation) [1, 2, 6, 29].

Ionospheric Layers

The ionosphere is vertically divided into four regions (see Figure 1.14):

1. *The D layer (60-90km):* Below 90 km, the atmosphere is denser, and the ionosphere is formed by chemical reactions and strong solar radiation (XR and Lyman α emission line, 121.5 nm). NO^+ and O_2^+ are dominant ions, but there are also negative and hydrated ions. The mixture of positive and negative ions and electrons ensures quasineutrality in this region. In quiet conditions, the electron density is below 10^{10} m^{-3}.

2. *The E layer (90-140 km):* In this region, the production of the main ions and constant recombination rates are in equilibrium. The expression for Chapman layers (Equation 1.28) describes the E layer very well. In this region, the peak in O_2^+ concentration occurs at ∼120 km due to the ionization by, mainly, 100-150 nm UV radiation, resulting in an electron density maximum. The E layer decays rapidly at night due to fast recombination rates.

3. *The F1 layer (140-200 km):* Photons in the 17 to 91 nm wavelength range produce the primary ion, NO^+. The ion production peak corresponds to the electron density peak (Chapman layer) at ∼150 km. However, this peak is often blended with the maximum electron density in the ionosphere (F layer [1] peak). At night, scattered solar radiation, starlight, and particle precipitation maintain the layer.

4. *The F2 layer:* At upper altitudes (above 200km), transport processes dominate, as the atmosphere is low in density. Atomic ions dominate in this region (O^+ concentration peaks between 250 and 400 km), and photoionisation occurs in the UV continuum (see Figure 1.15).

---

[1]The F2 layer, together with the F1 layer can be addressed as the F layer.

At upper altitudes (F layer), the chemical distribution of the ionospheric constituents is very heterogeneous, as the air molecules and atoms are separated by their mass (Equation 1.24). However, at lower altitudes (D layer), the atmospheric constituents are mixed due to turbulent processes (from lower atmospheric layers), and the regions are more homogeneous [1]. This chemical composition separation is represented by Figure 1.15, as well as all the ionization sources presented in this Section.
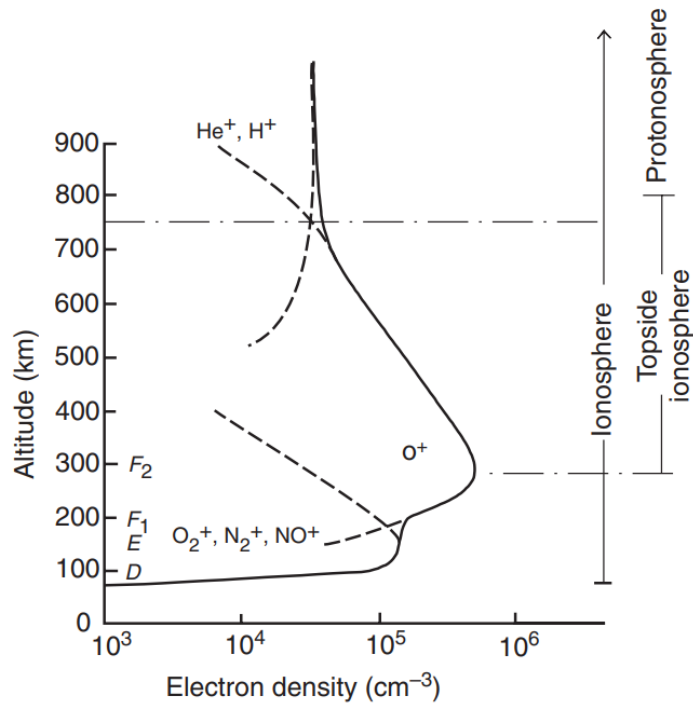
Figure 1.14: Representative layered structure of the ionosphere with ion density profiles for the daytime at middle latitude [1].
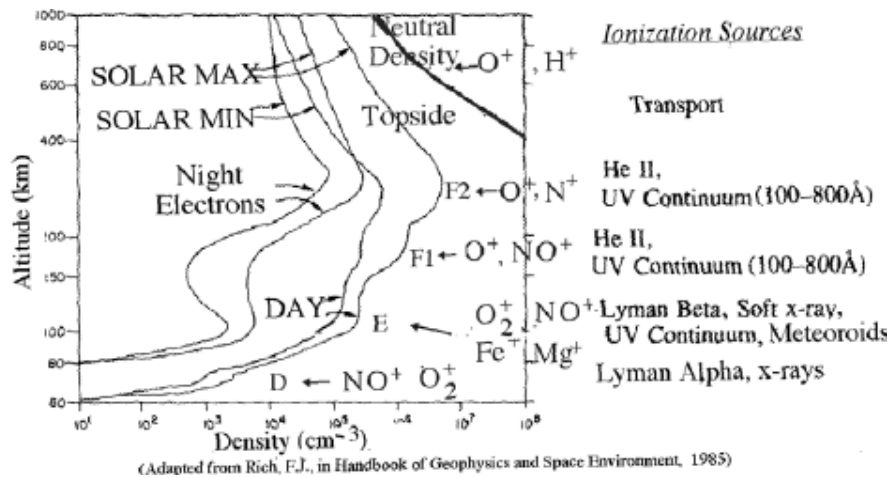
Figure 1.15: Representation of ionospheric layers on Earth showing the composition of major ions and main ionisation sources for each layer [30].

Ionospheric Currents

Three current systems flow in the ionospheric E region: Sq (solar-quiet) at middle latitudes, EEJ (equatorial electrojet) near the equator and the auroral electrojet (AE) in the polar regions (see Figure 1.16). The electric currents are generated because particles are dragged by the Earth's electric and magnetic fields. Solar EUV shapes Sq, therefore solar influence (due to diurnal and semi-diurnal tides, seasonal changes of the insolation and the solar activity cycle) is very strong in this current system. The Sq current system generates magnetic field variations. The EEJ at the magnetic equator is a much stronger current because the Earth's magnetic field lines are almost parallel to the Earth's surface. The energy transferred from the solar wind through the field aligned currents controls the behaviour of the AE, therefore, during geomagnetic storms, it is pushed equatwordly and intensified [6].
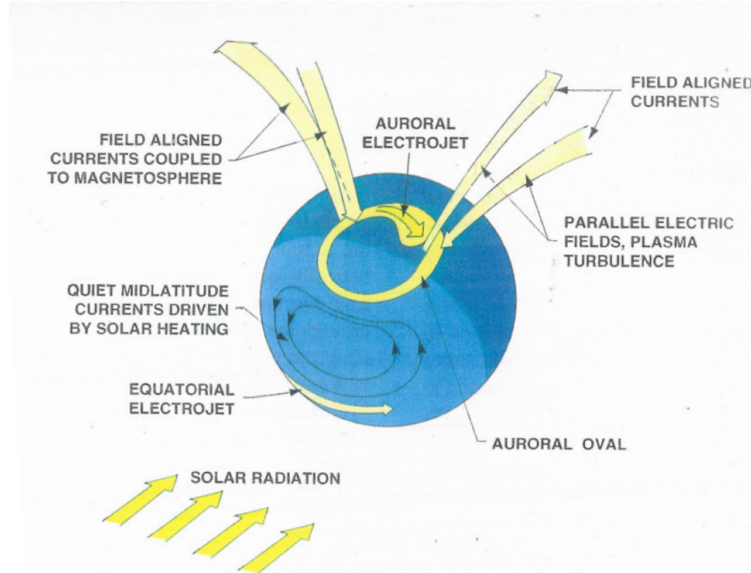
Figure 1.16: Ionospheric currents: Sq (dayside, in yellow), EEJ (dayside, in black) and auroral electrojet (connected to the field aligned currents, in light yellow) [31].

Ionospheric Irregularities

Solar infrared radiation heats the atmosphere. The heating of neutral components generates tides that propagate upwards to the ionosphere. Tides and gravity waves from the mesosphere can affect the electron densities and trigger plasma irregularities.

At night, plasma instabilities may cause inhomogeneities in the E region of the ionosphere. These are called **plasma bubbles**, elongated regions of lower-density plasma that may drift along large distances. Other irregularities are the **traveling ionospheric disturbances** (TIDs) that usually result from atmospheric waves (air motions). These perturbations have long wavelenghts ($\sim$1000 km) and travel horizontally ($\sim$ 250 m/s) [1].

Geomagnetic activity changes the thickness of the ionospheric layers. Instabilities in the plasma and enhanced currents in the magnetosphere may heat the components of the ionosphere. Recombination decreases with a temperature increase, leading to an increase in

electron density [6]. Particle precipitation will also increase during a storm, mostly in high latitudes. Waves propagating equatorwardly enhance ionization at middle and low latitudes.

The total electron content

The total electron content (TEC) is an integral parameter:

$$TEC = \int n_e(s)ds \tag{1.29}$$

which gives the total number of electrons along a line of sight (s) from the ground up to the upper boundary of the ionosphere in a tube of $1\ m^2$. TEC is measured in TEC units (TECu): 1 TECu $= 10^{16}$ electrons/m^2. During a day, TEC varies with the changes in the insolation. After the sunrise, it increases rapidly and reaches its peak around noon, and at sunset, the ionization source disappears and TEC decays. Seasons affect TEC's behaviour during a year since changes in solar zenith angle affect photoionization. Changes in the radiation flux from the Sun also affect TEC, which happens during the solar cycle. TEC is usually higher during the solar maximum, as the solar EUV emission increases [24]. On average, TEC values are smaller during solar minimum.

The TEC response to SW events (flares and geomagnetic storms) usually consists of changes in the amplitude and shape of the daily TEC variation. Changes in ionospheric electron density, identified by TEC variations, can perturb the GNSS signal and interfere with its precision in the affected area, thus, TEC is a good parameter to monitor ionospheric conditions.

Ionospheric storms (ionospheric disturbances caused by geomagnetic storms) may be classified as positive or negative, whether TEC increases or decreases during the event. A negative ionospheric storm is caused by an O/N_2 density ratio decrease as temperature increases [32].

A positive ionospheric storm is usually caused by a more complex mechanism: electron density increases because the F2 layer is lifted. That happens when the vertical plasma drift is weakened by storm-induced heat circulation, causing the plasma to stay in upper altitudes [33].

Ionosphere measurements

Plasma parameters in the ionosphere are measured by a number of techniques. These can be direct or remote, and they use the proprieties of plasma (for example, reflective or dispersive properties). From the properties of electromagnetic wave propagation, described in Section 1.1, there is a critical frequency which limits the frequencies used in, for example, radio communications. This property is used in the measurement of ionospheric densities. The most well-known ionospheric sensing device is the ionosonde. It transmits a slant or vertical radio pulse and calculates the altitude of the reflection using the time delay between the sent and reflected signals. Then, the corresponding electron density is calculated with the received frequency. The layers' peaks are measured with the highest frequency signal that is reflected to the ionosonde. The topside ionosphere is measured using remote techniques similar to an ionosonde: a satellite transmitter sends signals downwards, these are reflected to the satellite to calculate the electron density profile above the F2 peak.

2

MATHEMATICAL METHODS

This chapter describes the method used for the data analysis: basic statistics and the principal component analysis.

2.1 Statistical data analysis

Considering a sample of a variable $x(x_1, x_2, ..., x_n)$ of size n. The mean of that sample is given by:

$$\bar{x} = \frac{1}{n} \sum_{i=1}^{n} x_i \tag{2.1}$$

In this work, two types of means are calculated using Equation 2.1 [34]. The sample mean of a specific variable for n measurements (for example, TEC value for the same hour of a day, during the entire month) and the average value of n different variables (for example, the mean of TEC during an entire month).

The uncertainty of the means is given by the standard deviation σ:

$$\sigma = \sqrt{\frac{1}{n} \sum_{i=1}^{n} d_i^2} \tag{2.2}$$

where $d_i = x_i - \bar{x}$ is the deviation between each value x_i and the mean of the variable x. This uncertainty will be used to calculate:

1. the error bars ($+\sigma$,-σ) with respect to the mean of a variable x.

2. the statistical significance interval $\pm 2\sigma$ for a calculated value of a variable x.

For dealing with gaps (NaN values) in the analysed data sets, a polynomial interpolation function is used:

$$y = a_0 + a_1(x - x_0) + a_2(x - x_0)(x - x_1) \tag{2.3}$$

Coefficients a_0, a_1, a_2 are obtained in an incremental way. From a known data point (x_0, y_0), $a_0 = y_0$. From a following data point (x_1, y_1), $a_1 = \frac{y_1 - y_0}{x_1 - x_0}$. With a third data point (x_2, y_2), $a_2 = \frac{\frac{y_2 - y_1}{x_2 - x_1} - \frac{y_1 - y_0}{x_1 - x_0}}{x_2 - x_0}$. The (x_i, y_i) are the points where interpolation is performed and (x, y) is the interpolated value (previously a NaN value).

2.2   Principal component analysis

The principal component analysis (PCA), also known as the empirical orthogonal function (EOF) expansion, aims to analyse the variability of time series, finding patterns in the data. This method is also used for smoothing data using fewer variables, filtering noise and revealing the main features of complex, multi-variable data without using biased parametrisation.

Considering two sets of data, each from one particular measurement of a variable, with null mean, A=$a_1, a_2 \cdots a_n$ and B=$b_1, b_2 \cdots b_n$ written in row vector shape:

$$\mathbf{A} = \begin{bmatrix} a_1 & a_2 & \cdots & a_n \end{bmatrix} \tag{2.4}$$

$$\mathbf{B} = \begin{bmatrix} b_1 & b_2 & \cdots & b_n \end{bmatrix} \tag{2.5}$$

one defines the covariance between the two datasets as follows:

$$cov_{AB} = \frac{1}{n} \sum_i a_i b_i \tag{2.6}$$

$$cov_{\mathbf{AB}} = \frac{1}{n} \mathbf{AB}^T \tag{2.7}$$

which expresses the degree of linearity between variables A and B. $\mathbf{B}^T$ is the transpose of matrix B (hereafter).

Generalising from two datasets to an ensemble of m datasets, it is possible to define a matrix containing n columns of the values of each of the m datasets (rows).

$$\mathbf{X} = \begin{bmatrix} x_{11} & x_{12} & \cdots & x_{1n} \\ x_{21} & x_{22} & \cdots & x_{2n} \\ \vdots & \vdots & \ddots & \vdots \\ x_{m1} & x_{m2} & \cdots & x_{mn} \end{bmatrix} \tag{2.8}$$

Each dataset of $\mathbf{X}$ (or column) can be seen as a vector in an m-dimensional vector space [35]. An orthogonal basis generates this space. It is composed of linearly independent orthogonal pairs of vectors of unitary norm. Any vector of $\mathbf{X}$ can be expressed as a linear combination of the set of this basis [36]. The method described below will find a suitable orthonormal basis $\mathbf{E}$, by doing a change of basis using the identity matrix (m x m) $\mathbf{I}$ as the original basis [35]:

$$\mathbf{EX} = \mathbf{IY} \tag{2.9}$$

$\mathbf{E}$ relates the original data $\mathbf{X}$ to a "rotated" version of the data $\mathbf{Y}$. The vectors $\mathbf{E}_i$ of $\mathbf{E}$ are called the **Empirical Orthogonal Functions**, and the vectors $\mathbf{P}_i$ of $\mathbf{Y}$ will be the

Principal Components. The covariance matrix gives the covariance between all possible combinations of two datasets in the ensemble:

$$\mathbf{cov}_X = \frac{1}{n}\mathbf{XX}^T \tag{2.10}$$

Keeping in mind equation 2.10, the goal is to optimise the covariance matrix of the new data, $\mathbf{cov}_Y = \frac{1}{n}\mathbf{YY}^T$. Obtaining the largest variances and minimising the covariances allows the new data to be expressed in fewer datasets, containing the main features [35].

Writing $\mathbf{cov}_Y$ in terms of $\mathbf{E}$:

$$\mathbf{cov}_Y = \frac{1}{n}\mathbf{YY}^T = \frac{1}{n}\mathbf{EXX}^T\mathbf{E}^T = \mathbf{E cov}_X\mathbf{E}^T \tag{2.11}$$

Since $\mathbf{cov}_X$ is a symmetric matrix, it is orthogonally diagonalisable, therefore, $\mathbf{E}$ should satisfy the condition:

$$(\mathbf{EDE}^T)^T = \mathbf{EDE}^T \tag{2.12}$$

where $\mathbf{D}$ is a diagonal matrix. Assuming that $\mathbf{E}$ is also orthogonal ($\mathbf{E}^{-1} = \mathbf{E}^T$):

$$\mathbf{cov}_Y = \mathbf{D} = \begin{bmatrix} \lambda_1 & 0 & 0 & \dots & 0 \\ 0 & \lambda_2 & 0 & \dots & 0 \\ 0 & 0 & \lambda_3 & \dots & 0 \\ \vdots & \vdots & \vdots & \ddots & \vdots \\ 0 & 0 & 0 & \dots & \lambda_m \end{bmatrix} \tag{2.13}$$

This becomes an eigenvectors problem, solved by finding the eigenvectors of $\mathbf{cov}_X$ using the

following equation [35]:

$$\mathbf{cov}_X \mathbf{E} = \mathbf{cov}_Y \mathbf{E} \tag{2.14}$$

$$\mathbf{cov}_X \mathbf{E} = \mathbf{DE} \tag{2.15}$$

The eigenvectors are the EOFs (matrix $\mathbf{E}$). The eigenvalues will be the diagonal values of $\mathbf{cov}_Y$ representing the variances.

The principal components $\mathbf{P}_i$ are obtained using Equation 2.9. Finally, data can be presented as a combination of eigenmodes:

$$X = \sum_{i=1}^{m} \mathbf{P}_i \mathbf{E}_i \tag{2.16}$$

Equation 2.16 shows how the PCs and respective EOFs will decompose dataset X. Vector $\mathbf{P}_1$ will have the largest variance. Vectors $\mathbf{P}_2...\mathbf{P}_m$ will be orthogonal to this one and with decreasing variances.

PCA was used in this work to analyse TEC datasets. A description of the implementation of the method within the analysis of TEC is given in Section 4.2.

Data sources and description 3

3.1 TEC data

The ionospheric TEC used in this work covers the time interval between December 2014 and November 2018, corresponding to the descending phase of the solar cycle 24, whose maximum was in 2014. TEC data were collected at three different Portuguese locations (see the map from [4] in Figure 3.1):

1. Continental Portugal: For the area around Lisbon, there were two data sources,

   1.1 $(38,70°$ N, $9,14°$ W) A SCINDA GNSS receiver in the area of the Lisbon airport [37] (data from November 2014 to November 2018 [38]).

   1.2 $(38,70°$ N, $9,40°$ W) A RENEP (Rede Nacional de Estações Permanentes GNSS, [39] (accessed on 26 April 2023)) geodetic GNSS receiver in Cascais (Lisbon), (data from February 2015 to June 2015 and from January 2017 to November 2018).

2. Archipelago of the Azores: For the Azores, there were two data sources,

   2.1 $(37,80°$ N, $25,30°$ W) A RENEP geodetic GNSS receiver at Furnas (São Miguel island), (data from January 2015 to June 2015 and from January 2017 to November 2018).

   2.2 $(36,80°$ N, $26,60°$ W) A RAEGE-Az (Associação Rede Atlântica de Estações Geodinâmicas e Espaciais—Açores, [40] (accessed on 26 April 2023)) geodetic GNSS receiver at Santa Maria island (data for May 2017).
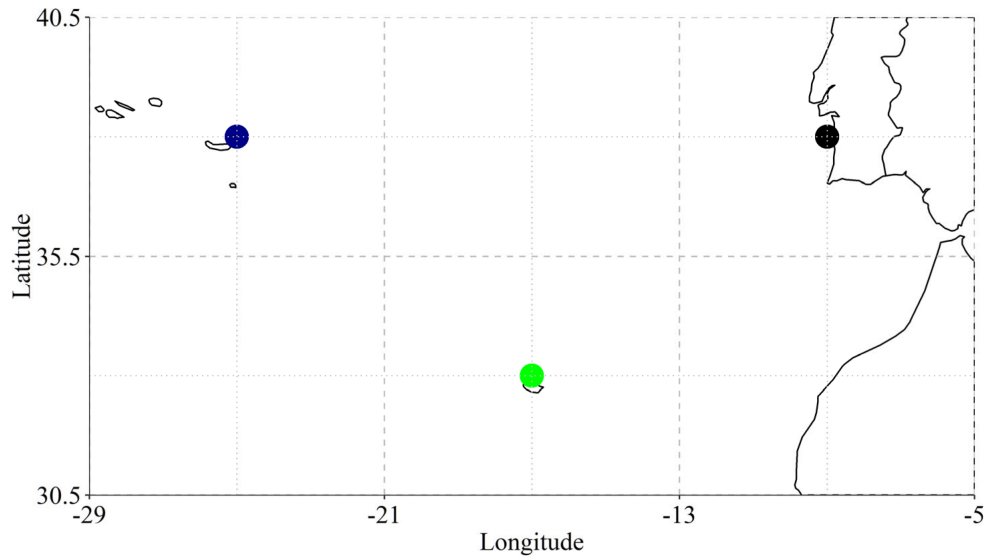
Figure 3.1: Circles show the approximate location of GNSS receivers at Continental Portugal (black), Azores (blue) and Madeira (green) archipelagos [4].

3. Archipelago of Madeira: For Madeira, there was one data source,

   3.1 $(32,70°$ N, $16,90°$ W) A RENEP geodetic GNSS receiver at Funchal (data from January 2015 to June 2015 and from January 2017 to November 2018).

All of the data used were processed and calibrated to TECu (10^{16} electroms/m^2) (as described in [4, 37, 38, 41–43]. TEC series used in this work have a 1-hour time resolution for all the receivers. Small data gaps were interpolated as described in Chapter 2. Time is given in Coordinated Universal Time (UTC). For the Continental Portugal and the Madeira archipelago, this corresponds to Local time (LT); for the Azores, LT = UTC - 1.

3.2 Space weather data

Geomagnetic storms were identified by the Dst index (1-hour time resolution) obtained from the OMNI database [26]. The threshold to define a geomagnetic storm is Dst ≤ -50 nT as it is the generally accepted criterion [6].

The solar flare data (time of the flare beginning, duration, and the flare type) are from the NOAA (National Centers for Environmental Information), GOES (Geostationary Operational Environmental Satellites) solar flare list, which includes data from 1975 to 2017 [44]. Solar flares are classified according to their intensity (electromagnetic flux) on a 5-level logarithmic scale: A, B, C, M and X, from the weakest to the strongest. There is also a sub-scale of intensities from 1-9. The A, B and weak C (C1 to C4) class flares are not strong enough for their effects to be noticed on Earth. Strong C (C5 to C9), M, and X flares may cause radio blackouts and radiation storms [45], thus, flares of these classes were used for the TEC variations' analysis. Only flares that started during local daytime (from the local sunrise to the local sunset) were studied.

The solar MgII emission, from the chromosphere, is a proxy for the UV solar radiance. The UV flux is given by a MgII composite series [46, 47] based on the measurements of the emission core of the MgII doublet (280 nm). The MgII index data are from the Institute of Environmental Physics, University of Bremen, http:/www.iup.uni-bremen.de/gome/gomemgii.html (accessed on 18 June 2023) (see [47] for more information).

As a proxy for the solar XR irradiance, the Solar EUV Experiment (SEE) - solar ultraviolet full-disk irradiance for the NASA TIMED mission (wavelength of 0.5 nm) were used. The data on the variations of the solar XR flux (XR (1e5) in $W/m^2/nm$) are from the LASP Interactive Solar Irradiance Data Center (LISRD), http:/lasp.colorado.edu/lisird/ (accessed on 18 June 2023).

DAILY TEC VARIATIONS 4

The main goal of this chapter is to describe how the daily TEC variations were obtained and analysed. These regular variations are due to the insolation variability. In terms of time, those are variations with the time of a day (this kind of variation is studied below, hereafter, the quiet daily variations or just daily variation), with seasons (time of a year) and the solar cycle. Spatially, TEC varies with longitude but mostly with latitude. The daily variations are calculated per month and location: each month will have a regularly varying daily curve of the typical quiet variations.

4.1   Quiet day analysis (QDA)

The standard procedure to calculate the quiet daily TEC variations is described below. The Dst index is used to identify geomagnetically quiet days (Dst > -50 nT) for each studied month. For each hour (H), from 0 to 23h, the quiet TEC values (TEC_{QD}) are calculated as an average of TEC values for this hour for all quiet days of the month.

The uncertainties of the quiet TEC values $TEC_{QD}(H)$ were computed using the standard deviation σ, where $\overline{TEC_{QD}}$ is the mean of $TEC_{QD}(H)$ for the 24 hours:

$$\sigma = \text{std} = \sqrt{\frac{1}{24} \sum_{H=0}^{23} (TEC_{QD}(H) - \overline{TEC_{QD}})^2} \tag{4.1}$$

This method relies deeply on the correct selection of all the quiet days and the availability of the observational data for these days.

The TEC_{QD} (Figures 4.1 to 4.3) calculated for all three locations shows the typical quiet day TEC variation. From 0:00 to about 6:00 UTC, TEC values are the lowest (at night, with no insolation, a non-zero number of free electrons can only be maintained by transport processes in the ionosphere). As the Sun rises, TEC starts to increase. A maximum of TEC is usually seen between 12:00 UTC and 15:00 UTC as a result of the ionisation during the solar midday. Sometimes, a second peak can be spotted in this time interval. Starting from about 15:00 UTC, TEC starts to decrease during dusk time as insolation decreases.
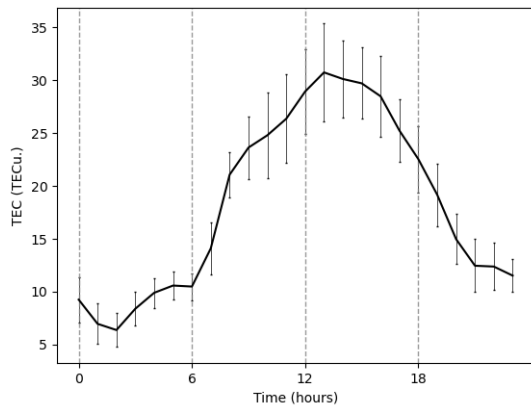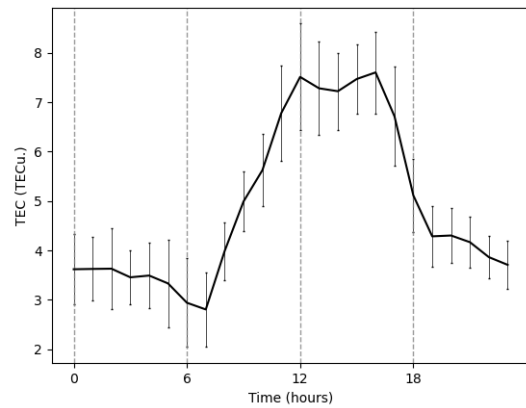
(a) Average daily curve for February 2015. (b) Average daily curve for January 2018.

Figure 4.1: Daily TEC variations for Lisbon for February 2015 (a) and January 2018 (b). Error bars represent the standard deviations from the mean value.
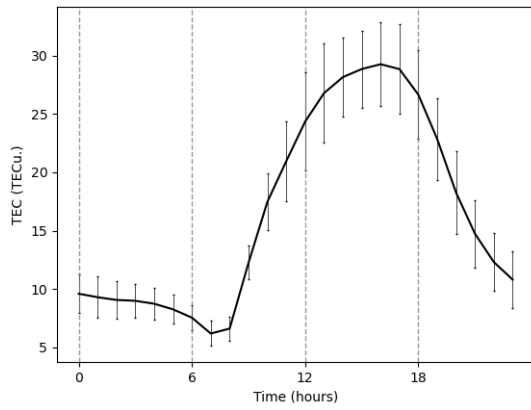
(a) Average daily curve for February 2015.
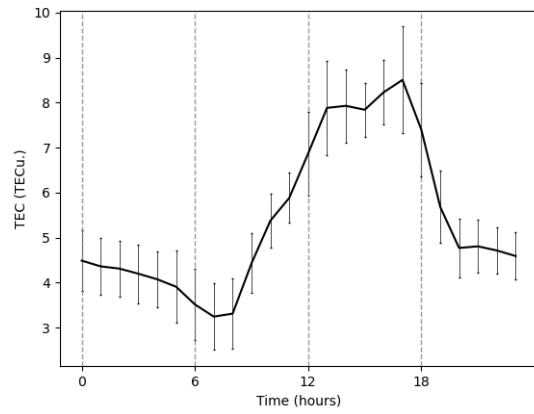
(b) Average daily curve for January 2018.

Figure 4.2: Same as Figure 4.1 but for the Azorean archipelago.
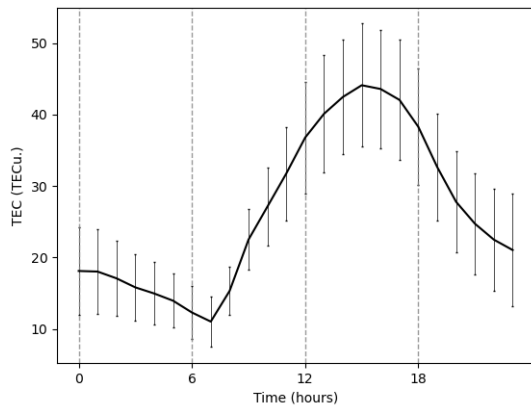
(a) Average daily curve for February 2015.
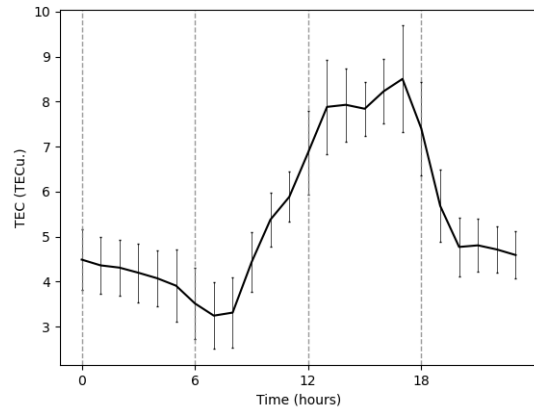
(b) Average daily curve for January 2018.

Figure 4.3: Same as Figure 4.1 but for Madeira.

4.2   Principal component analysis (PCA)

As was said above, the standard procedure to define TEC_{QD} is based on selecting the geomagnetically quiet days of the month. Sometimes, this approach is complicated by gaps in the observations or a low-quality data. One of the goals of this work was to study the performance of another method to obtain TEC_{QD}: a decomposition method called the principal component analysis (see [48–50] as examples of the application of this method to geomagnetic field data).

The principal component analysis is used here to extract the regular variations of TEC by decomposing the data and expressing the daily variations in terms of eigenmodes. The procedure from [51] described below was implemented in a Python routine (see also Chapter 2 for the mathematical description of PCA):

1. The TEC data for each of the studied months are arranged into a matrix $X_{H,D}$, where H is the hours from 0 to 23 and D is the days from 1 to the last day of the month (28, 29, 30 or 31 depending on a month and a year) (e.g. 24x30 for April).

$$
\mathbf{X}_{H,D} = \begin{bmatrix} x(0,1) & x(0,2) & \ldots & x(0,30) \\ x(1,1) & x(1,2) & \ldots & x(1,30) \\ \vdots & \vdots & \ddots & \vdots \\ x(23,1) & x(23,2) & \ldots & x(23,30) \end{bmatrix}
$$

2. In the data matrix $\mathbf{X}$, the mean values are removed from each of the columns (each day of the month):

$$
x(H,D) = X(H,D) - \bar{D} \tag{4.2}
$$

43

$$\bar{D} = \frac{1}{24} \sum_{H=0}^{23} X(H, D)$$

and each column of $\mathbf{X}$ will have zero mean. This step is needed for the correct interpretation of the covariance matrix.

3. The covariance matrix $\mathbf{cov}_X$ of $\mathbf{X}$ is build as:

$$\mathbf{cov}_X = \mathbf{X}^T \mathbf{X} \tag{4.3}$$

where $\mathbf{X}^T$ is the transposed matrix of $\mathbf{X}$. Then the eigenvalue problem appears as:

$$\mathbf{cov}_X \mathbf{E} = \Lambda \mathbf{E} \tag{4.4}$$

where Λ is the diagonal matrix containing all the eigenvalues λ_i of $\mathbf{cov}_X$ and $\mathbf{E}$ is the matrix containing the eigenvectors e_i for the ith mode. The λ_i are the eigenvalues that give the degree of variance in $\mathbf{cov}_X$, and the EOFs correspond to the eigenvectors e_i found. When normalized (the sum of the normalized λ_i is equal to 1), the eigenvalues show a part of the original series's variability related to the *ith* mode. Tables with the first three λ_i for all the studied months and all the locations are displayed in Appendix B.

4. The PCs are obtained by doing the dot product of the data matrix $\mathbf{X}$ (e.g. 24x30) with each EOF (in this case 30x1) :

$$PC_i = \mathbf{X} \cdot EOF_i \tag{4.5}$$

The PCs correspond to the daily variations of TEC, while the EOFs correspond to the amplitudes of those variations. If the eigenvalues λ_i are ordered from highest to

lowest, then PC1 and EOF1 correspond to the main (1st) mode. As one can see from Appendix B, this mode accounts for 78-99% of the variability of TEC depending on a month, a year and a location.

5. Finally, it is possible to reconstruct the monthly mean daily TEC variation $TEC_{PC}(H)$ by multiplying PC (24x1) by the mean of the corresponding EOF (1x1) followed by adding the daily means, removed in step 2.

$$TEC_{PC}(H) = \left(PC_1 \cdot \sum_{D=1}^{30} EOF_1(D) \right) + \bar{H}D \qquad (4.6)$$

As one can see from Figures 4.4, 4.5 and 4.6, the 1st mode (PC1 and EOF1) represents a variation that resembles the quiet daily TEC variations. Figures 4.7, 4.8 and 4.9 show examples of the daily TEC variations obtained by the standard procedure (TEC_{QD}) and the PC1 scaled by the corresponding EOF1s (TEC_{PC}).
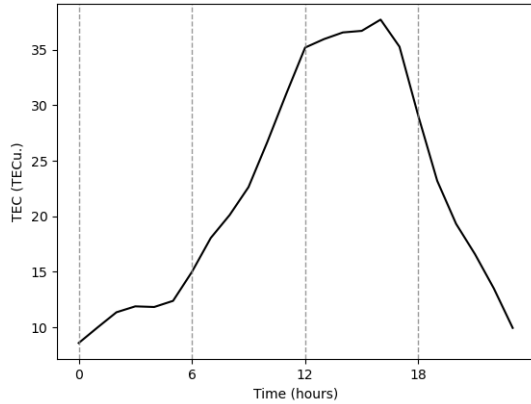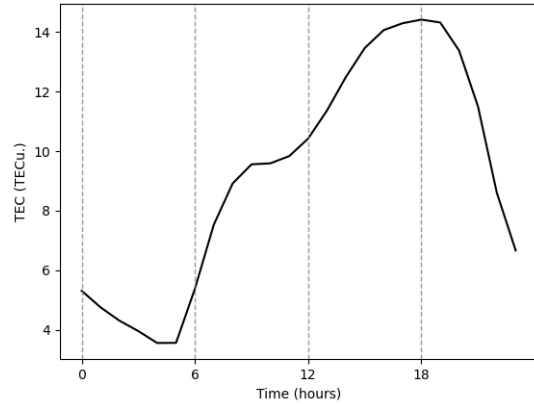
(a) TEC_{PC} curve for March 2015.   (b) TEC_{PC} curve for May 2017.

Figure 4.4: TEC_{PC} for Lisbon (as in Equation 4.6 for March 2015 (a) and May 2017 (b).
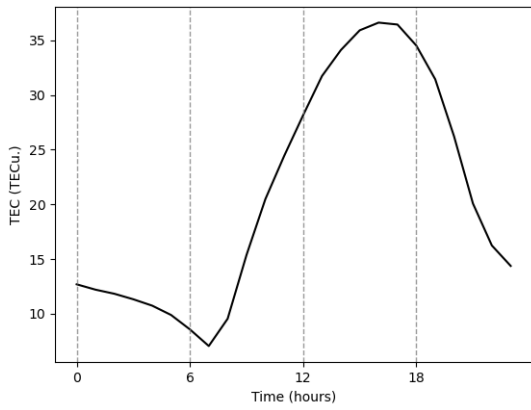
(a) TEC_{PC} curve for March 2015.
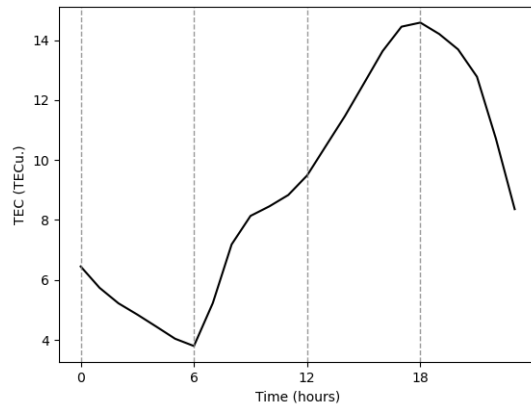
(b) TEC_{PC} curve for May 2017.

Figure 4.5: Same as Figure 4.4 but for the Azores.
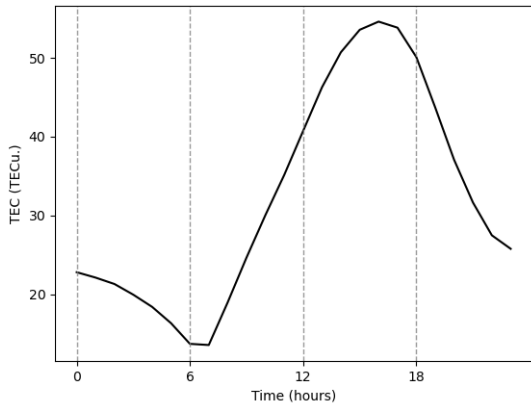
(a) TEC_{PC} curve for March 2015.
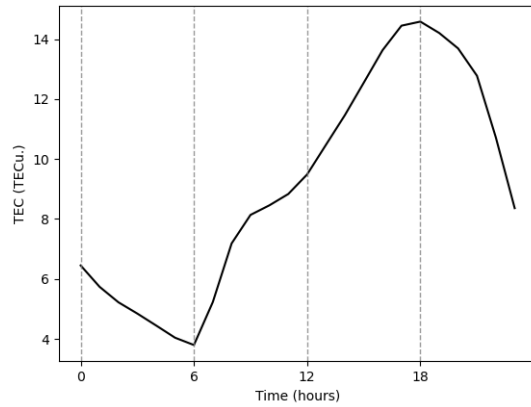
(b) TEC_{PC} curve for May 2017.

Figure 4.6: Same as Figure 4.4 but for Madeira.
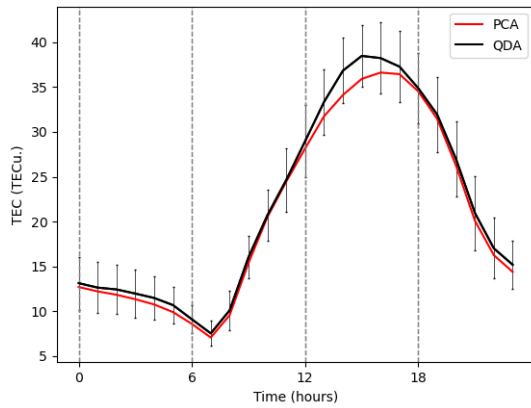
(a) PCA vs QDA curves for March 2015.
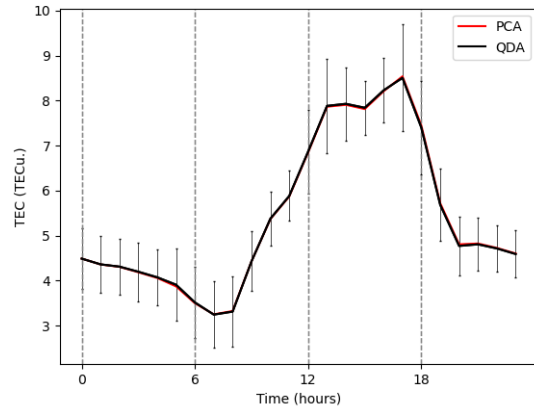
(b) PCA vs QDA curves for January 2018.

Figure 4.8: Same as Figure 4.7 but for the Azores.
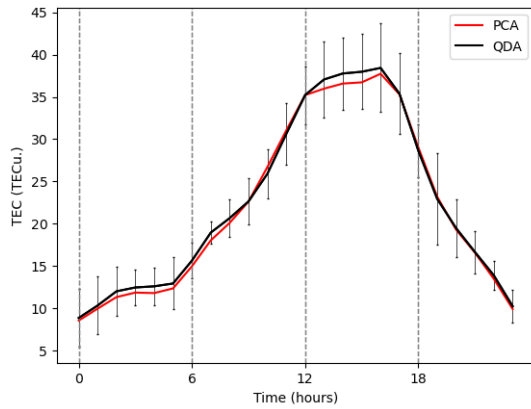
(a) PCA vs QDA curves for March 2015.
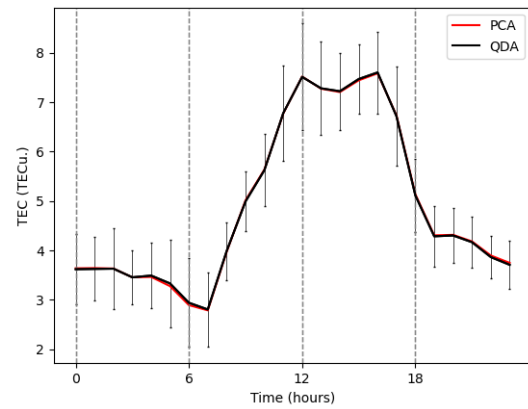
(b) PCA vs QDA curves for January 2018.

Figure 4.7: Examples of the daily TEC variations obtained using both methods for Lisbon for March 2015 (a) and January 2018 (b).

As one can see, for March 2015, the differences between daily TEC variations obtained by the studied methods are noticeable but much smaller than the uncertainties defined by the standard deviation. For January 2018, PC1 and QD1's curves perfectly overlap for all three locations.
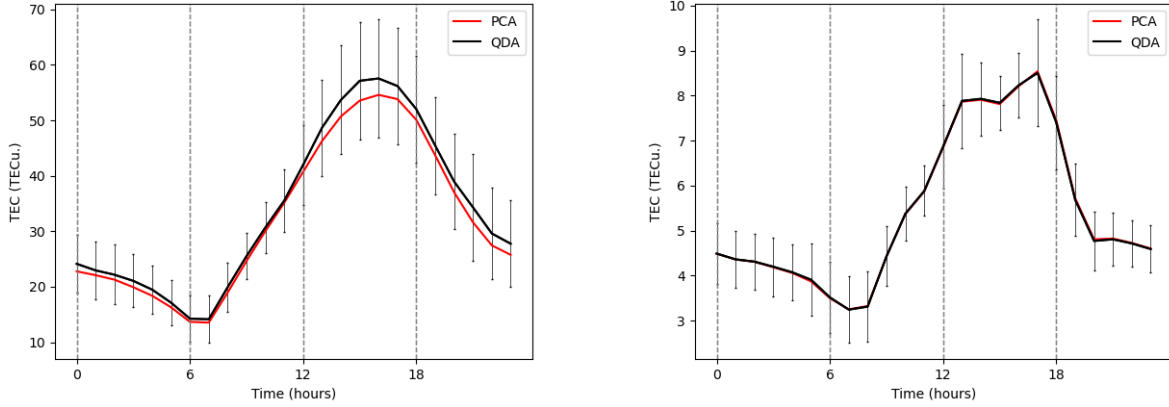
(a) PCA vs QDA curves for March 2015.

(b) PCA vs QDA curves for January 2018.

Figure 4.9: Same as Figure 4.7 but for Madeira.

A statistical analysis was performed to study the differences between TEC_{QD} and TEC_{PC}. The absolute difference Dif_{TEC} between TEC calculated from QDA and PCA is given by:

$$Dif_{TEC} = |TEC_{PC} - TEC_{QD}| \tag{4.7}$$

This difference was calculated for each hour of the daily variations. These differences averaged for six-hour intervals for some of the already mentioned months can be seen in Figures 4.10 to 4.12.

It is seen that the largest differences are observed during the periods between 12:00-18:00 UTC and 18:00-0:00 UTC. These correspond to periods where TEC varies the most, as can be deduced from the size of the error bars in Figures 4.10 - 4.12.

For all the studied months and locations, the TEC daily variations obtained by these two methods (QDA and PCA) are very similar. The differences between them are small: even if $Dif_{TEC} > 1$ TECu, it is still much smaller than the uncertainties for TEC_{QD}.

(a)   (b)
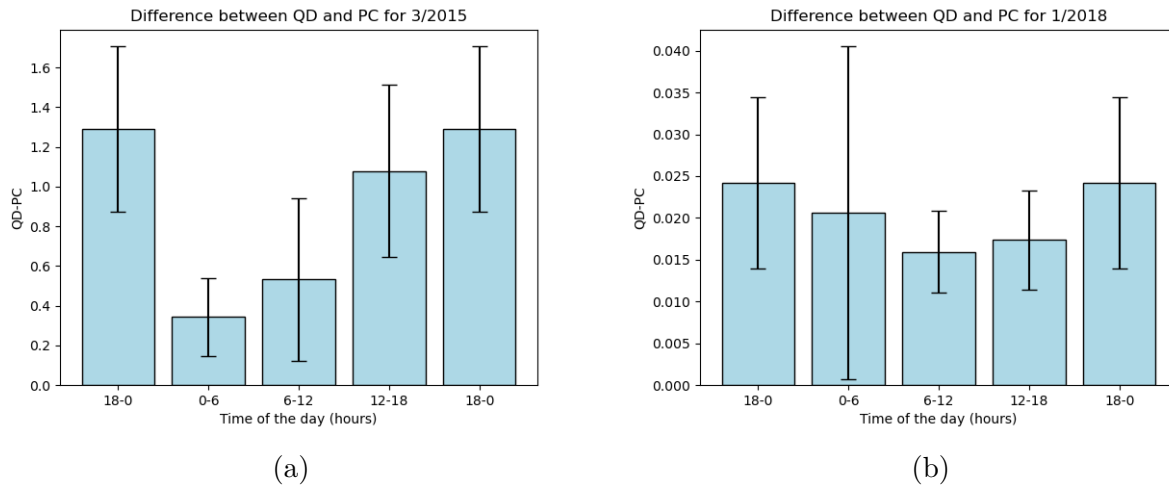
Figure 4.10: Absolute differences between the daily TEC variations calculated using PCA and QDA for Lisbon for four-time intervals of a day (from 00:00 to 6:00 UTC, from 6:00 to 12:00 UTC, from 12:00 to 18:00 UTC, and from 18:00 to 00:00 UTC) for March 2015 (a) and December 2018 (b). Error bars are 1σ. The first and last column bars are the same and correspond to the time interval 18:00-00:00 UTC.

(a)   (b)
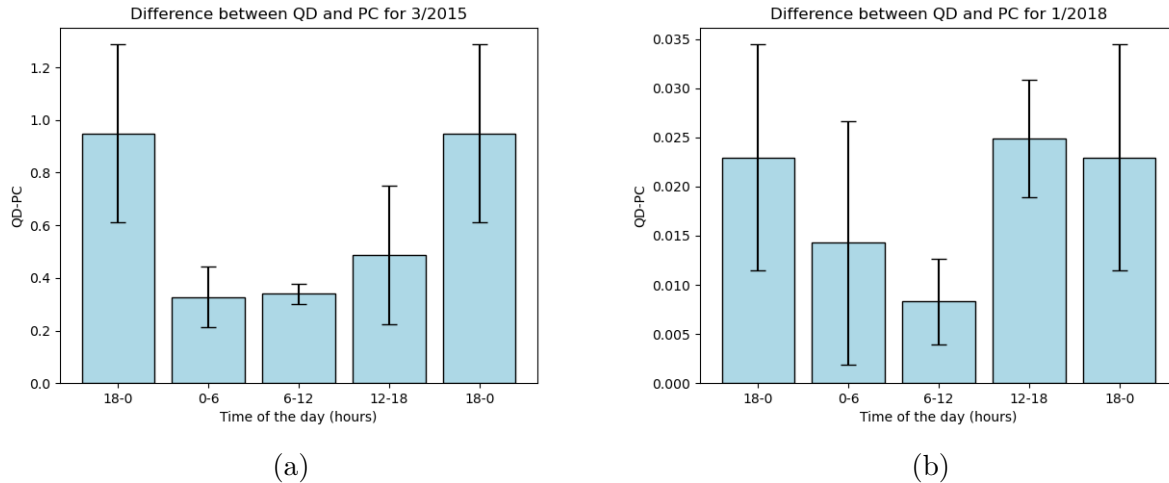
Figure 4.11: Same as Figure 4.10 but for the Azores.

For the studied time interval (December 2014 to November 2018), March of 2015 was the month with the largest maximum difference between TEC_{QD} and TEC_{PC}. It was a month with high geomagnetic activity and had only 18 quiet days. For QDA, this means

(a)

(b)
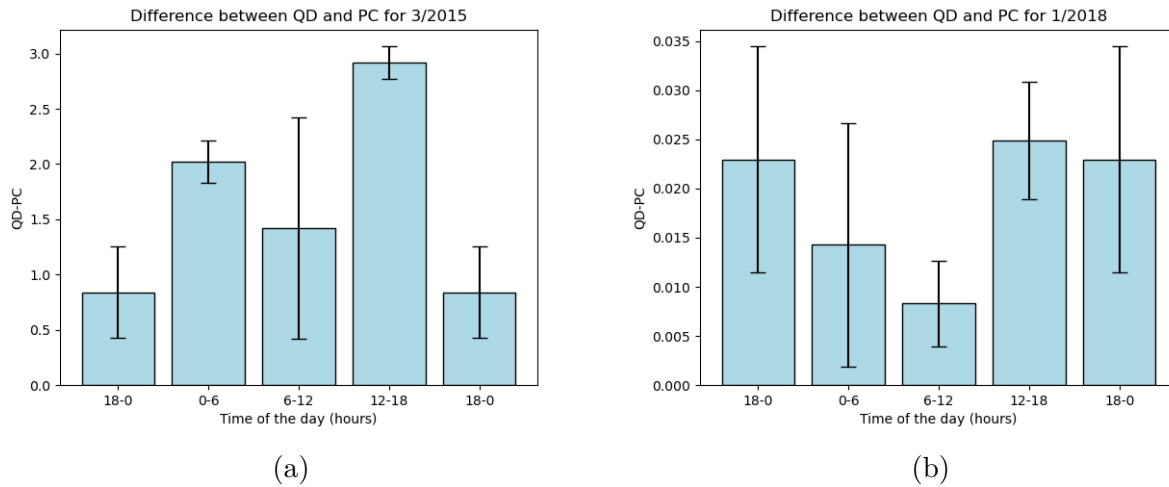
Figure 4.12: Same as Figure 4.10 but for Madeira.

13 fewer days to calculate TEC_{QD}, which may be a concern for the method's accuracy. For this month, the largest difference was obtained for the 12:00-18:00 UTC time interval for Madeira, Figure 4.12a.

Dif_{TEC} values also vary with seasons. Seasonal variations of Dif_{TEC} can be deduced from examples shown in Figure 4.13 - the differences obtained for a certain month for individual years, are averaged for all years available for this month for a studied location.

Lower TEC differences are associated with lower TEC variability. November has the lowest average differences as it is a month with lower TEC variability for the studied time interval (December 2014 - November 2018).

Finally, Dif_{TEC} averaged for all months and all years are shown in Figure 4.14 for the three studied regions: Lisbon, Azores and Madeira. The average differences are below 0.4 TECu. The largest values of Dif_{TEC} are obtained for the Azores data. This may be explained by the Azorean data having more gaps, and therefore, both PCA and QDA can have more uncertainties. Nevertheless, the values of Dif_{TEC} are still low enough even for months with data gaps.

(a)

(b)

(c)

(d)
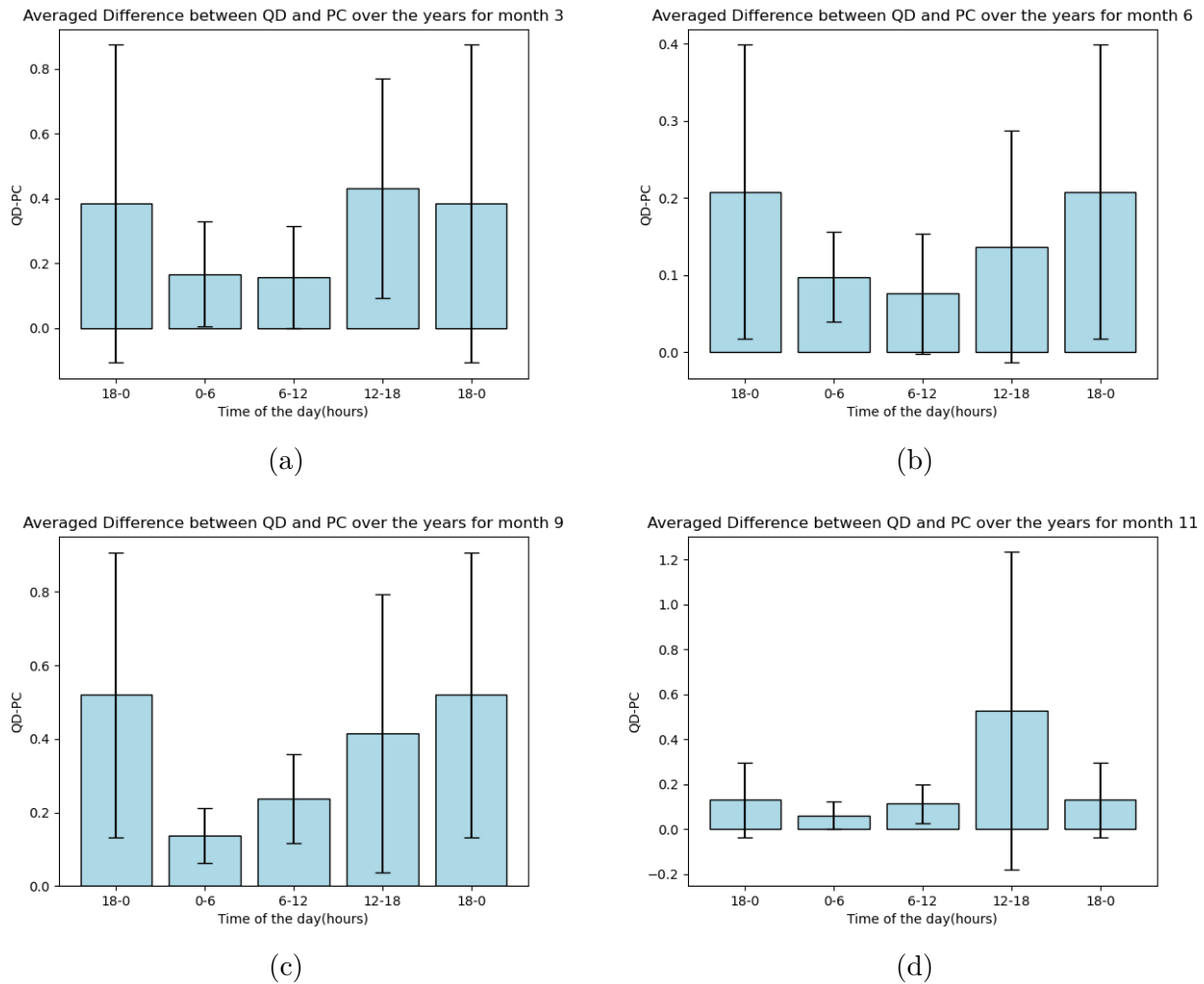
Figure 4.13: Average differences between TEC_{PC} and TEC_{QD} for certain months: March (a), June (b), September (c) and November (d) calculated using data of 2015-2018 for Lisbon. Error bars are 1σ.

The results presented here allow one to take the following conclusions: the daily quiet TEC variation can be obtained using PCA. The differences between the TEC variations obtained by PCA and QDA are small: less than 3 TECu for individual months and smaller than 0.5 TECu on average for the whole studied time interval (from December 2014 to November 2018). PCA usage has several advantages, for example, using PCA, the non-quiet days do not have to be verified individually.

(a)

(b)

(c)
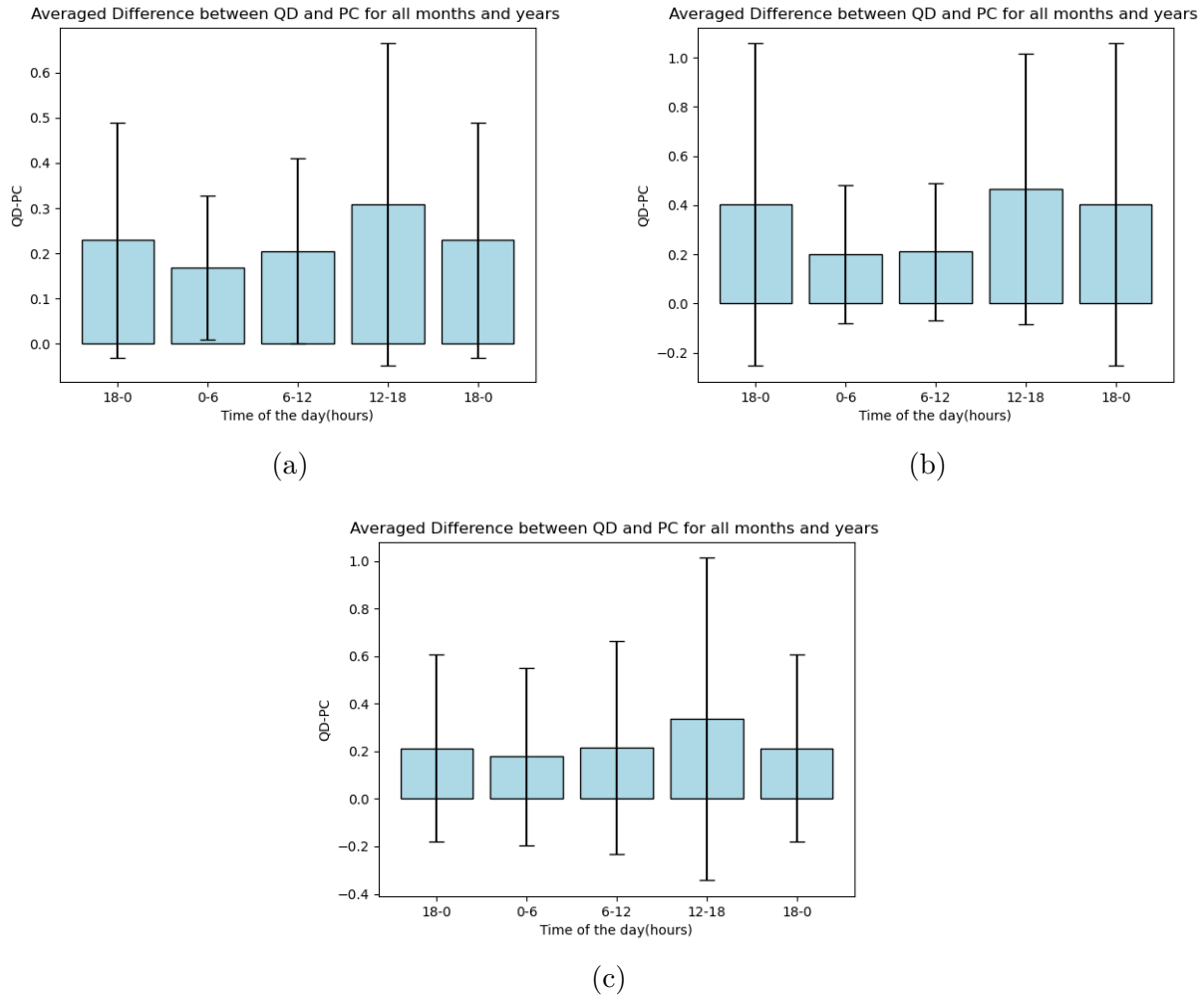
Figure 4.14: Same as Figure 4.13 but averaged for all available months and years for Lisbon (a), Azores (b) and Madeira (c).

As was mentioned before, the daily TEC variations depend on the time of the sunrise/-sunset and the total insolation that change through a year. Figures 4.15 - 4.18 show seasonal variations of the daily quiet TEC variations for the different locations during the year with the largest data availability: 2015 and 2016 for Lisbon, 2017 for Madeira and 2018 for Azores.

There are apparent differences between months. Colder (winter) months generally have lower insolation levels, later sunrises and earlier sunsets. TEC is generally lower and varies

less, the daily maximum (observed after the local noon) and minimum (observed before sunrise) are closer. Warmer months, having more solar time, present higher TEC values during the daytime.
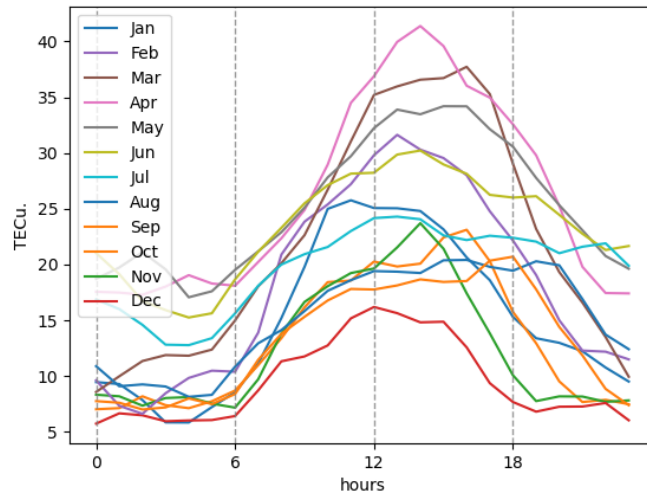
Figure 4.15: TEC_{PC} for the available months of 2015 for Lisbon.
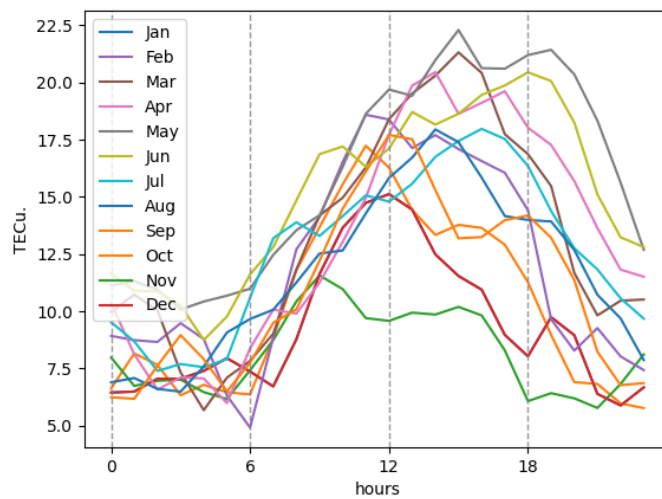
Figure 4.16: Same as Figure 4.15 but of 2016 for Lisbon.
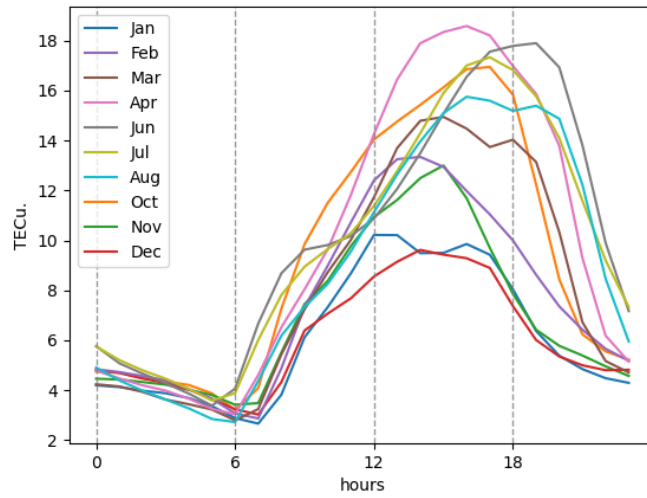
Figure 4.17: Same as Figure 4.15 but of 2017 for Madeira.
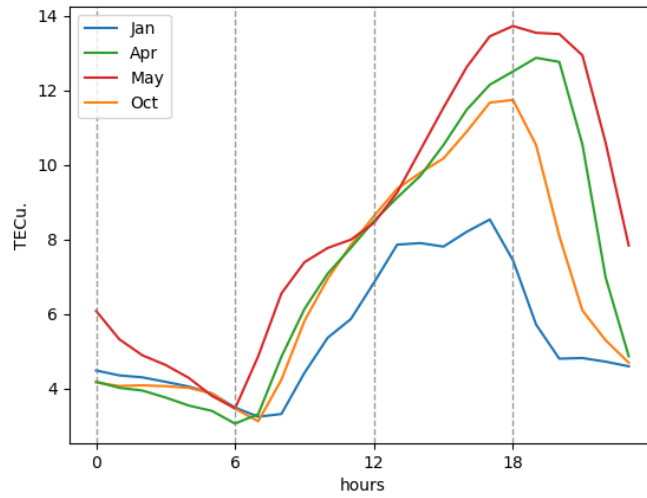
Figure 4.18: Same as Figure 4.15 but of 2018 for the Azores.

TEC RESPONSE TO SPACE WEATHER EVENTS

5

As mentioned in Section 1.4, many factors affect variations of ionospheric parameters during a disturbed period. In this chapter, the effects of geomagnetic storms (Section 5.1) and solar flares (Section 5.2) on the ionospheric TEC are analysed.

Disturbed periods related to geomagnetic storms were selected using the Dst index (days with Dst < -100 nT for severe storms and Dst < -50 nT for moderate storms). To study the effect of the solar flares on TEC, days with M, X, or more than 5 C flares occurring during the local daytime were selected.

Three TEC parameters were used to analyse TEC response to SW events:

1. Variations of TEC (Δ TEC): calculated subtracting the mean quiet values of TEC (TEC_{PC}) from the observed TEC values during the storm period (two days before, day (or two days for long storms) of a storm, two days after).

$$\Delta TEC = TEC - TEC_{PC} \tag{5.1}$$

The ΔTEC values above 2σ or below -2σ are considered statistically significant, where σ is the standard deviation.

$$\sigma = \sqrt{\frac{1}{D}\sum_{i=1}^{D}(TEC_i(H) - TEC_{PCi}(H))^2} \text{ (D = 5 or 6)} \tag{5.2}$$

$$\tag{5.3}$$

2. The daily mean TEC calculated for each day of the month:

$$\text{Daily mean TEC} = \frac{1}{24} \sum_{i=0}^{23} TEC_i(D) \tag{5.4}$$

The uncertainties for the daily mean TEC are given by the standard deviation of the dataset. This parameter was used only to study the effects of geomagnetic storms.

3. The EOF1 (in arbitrary units) from the principal component analysis is used to see how the amplitude of the 1st PCA mode changes through the studied month. This parameter gives the amplitudes of the daily TEC variations for each day. This parameter was used only to study the effects of geomagnetic storms.

5.1   Geomagnetic storms

Geomagnetic storm of 7th of January 2015

Space weather conditions:

A CME directed towards Earth occurred on 3rd of January and was the cause of a geomagnetic storm on 7th of January (Dst = -107 nT in Figure 5.1). Also, during the following days, two coronal holes were seen [4].

TEC response:

For the studied locations, this geomagnetic storm caused a TEC increase on 7th of January after midday. TEC variations between around 10:00 UTC and 13:00 UTC were about 30 to almost 40 TECu.

For Δ TEC, Figure 5.2, it is possible to see a positive increase (Δ TEC $> 2\sigma$) indicating the difference between TEC at the time of the storm and the quiet TEC variations. An increase in TEC after the storm's main phase might have been caused by post-storm activity

in the equatorial ionosphere at the southern location, Madeira. These effects are seen in Figure 5.2.
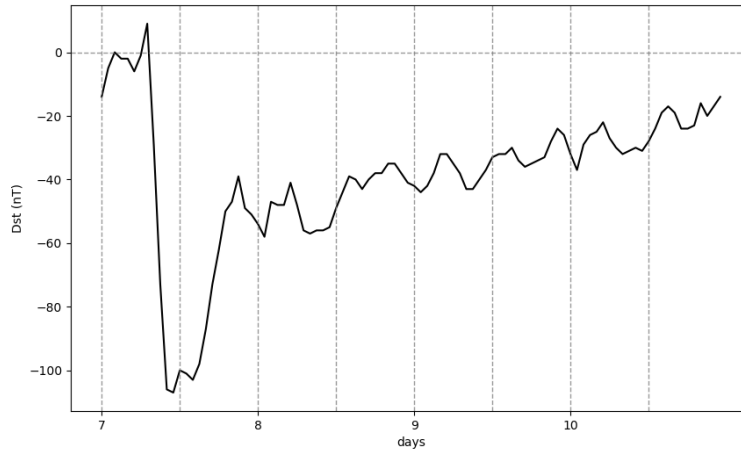
Figure 5.1: Dst over the period of 7-10th of January 2015.

The increase in ionization during this storm had a positive effect on the daily mean TEC on the day of the storm. As it is clearly seen from the plot in Figure 5.3, there was a difference in the overall mean of TEC between the locations studied. The daily mean TEC between 7th (the day of the storm) and 18th of January was bigger in Madeira, which may be related to disturbances in the equatorial electrojet (EEJ), since no similar TEC variations are seen for Lisbon and Azores located about 5° to the north of Madeira [4]. Between 28th and 31st of January, there was also an increase in the daily mean TEC at Madeira, which might have also been caused by disturbances in the EEJ.

The amplitudes of the daily TEC variations during the positive ionospheric storm can be seen using EOF1, presented in Figure 5.4. For all locations, on 7th of January, this parameter increased from 0.35 to 0.40 units. The low values of EOF1 in the Azores (7th,9th, and 10th of January) are due to data quality degradation.
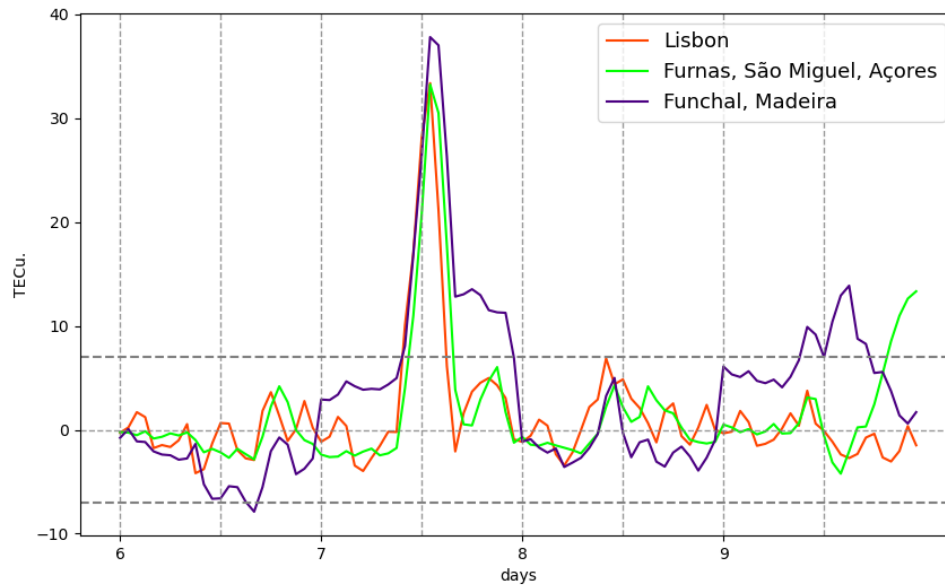
Figure 5.2: Δ TEC values over the period of 7-10th of January 2015, for all the locations studied. Grey dashed horizontal lines represent ± 2 σ.
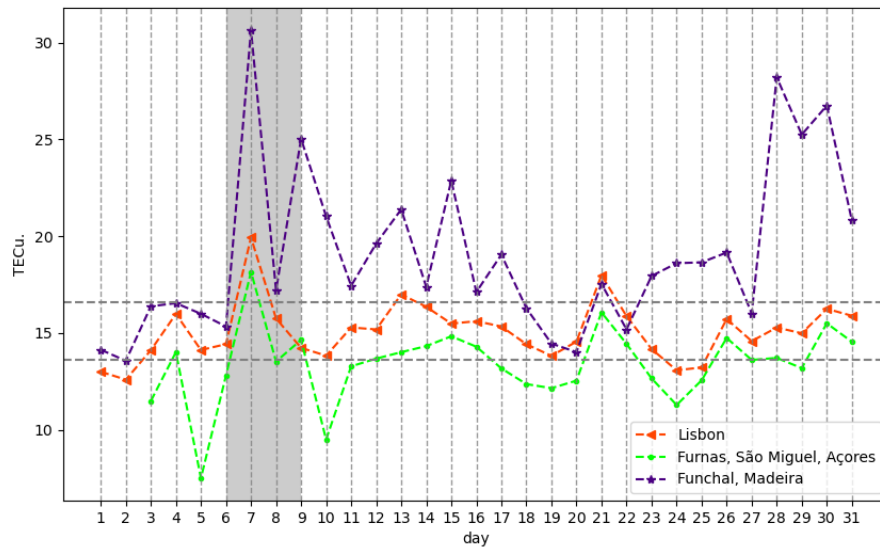
Figure 5.3: Daily mean TEC for January for all the locations. Grey dashed horizontal lines represent (mean of the month ± σ) and vertical grey bar represents the storm period.
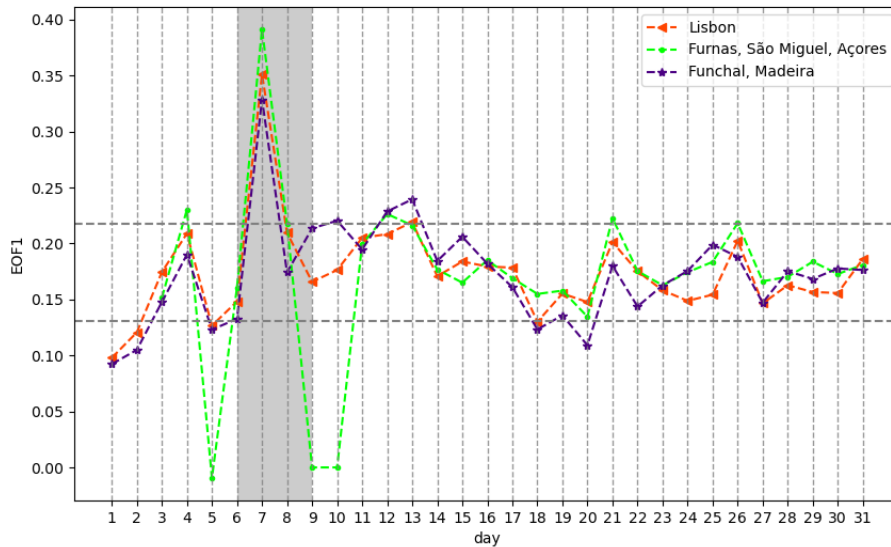
Figure 5.4: EOF1 for January for all the locations. Grey dashed horizontal lines represent (mean of EOF1 $\pm$ σ).

The positive response of the ionosphere to the geomagnetic storm in January 2015 was similar for all the locations studied. The greater TEC values of Madeira, both on Δ TEC and the daily mean TECs, were caused by other events as a consequence of the storm.

Geomagnetic storm of 17-18th of March 2015

Space weather conditions:

The strongest storm of the 24th solar cycle ($\mathrm{Dst}_{min} = -225$ nT, Figure 5.5) is usually called the *St. Patrick's Day storm* because it began on 17th of March 2015, St. Patrick's Day. A CME disturbed the interplanetary conditions on 16th of March and arrived on Earth on the morning of 17th of March. This event resulted in a nine-hour-long geomagnetic storm, [52]. Also, on 20th of March, a partial solar eclipse occurred with the maximal obscuration at 09:00 UT of 66% at Lisbon, 72% at Azores, and 57% at Madeira. This eclipse caused not only a general decrease of the ionization rate due to a decrease of the solar UV and XR fluxes

but also generated atmospheric waves that produced TIDs in the west-to-central Europe [4].
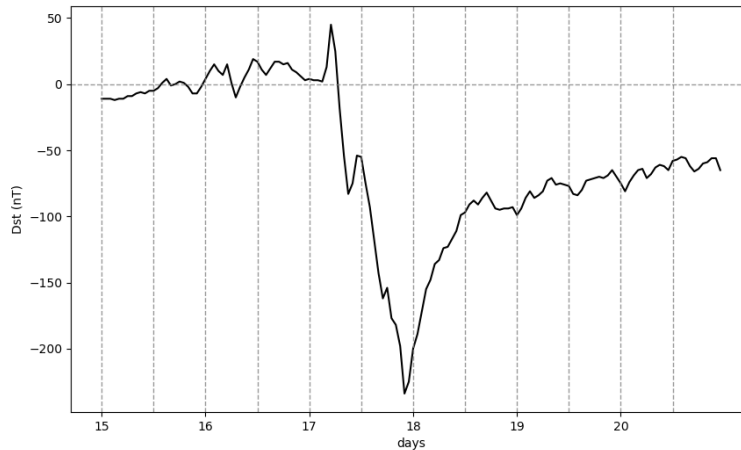
Figure 5.5: Dst over the period of 15-20th of March 2015.

TEC response:

The ionospheric response to this geomagnetic storm consisted of increased electron density resulting in a TEC increase by 20 to 35 TECu depending on the location, as supported by the plot of Δ TEC in Figure 5.6. The positive ionospheric storm in the afternoon of 17th of March was followed by a TEC decrease (Δ TEC < -2σ) in the afternoon of 18th of March (negative ionospheric storm). During day 17th, there was a secondary TEC daily peak at around 19:00 UTC. The increase of TEC on 17th of March began sooner in Lisbon, then in the Azores and Madeira, while the negative phase was synchronous for all the studied locations. The recovery phase occurs during 19th of March. On the day of the eclipse (20th of March), a decrease in TEC was observed, lasting longer for the locations at lower latitudes as is shown in [53] and in Figure 5.6).

The daily mean TEC for March, in Figure 5.7, has a significant difference between the region of Madeira and the other analysed locations. EEJ may be the cause for higher TEC values in the southern region [4]. The TEC mean is larger on 17th of March than during
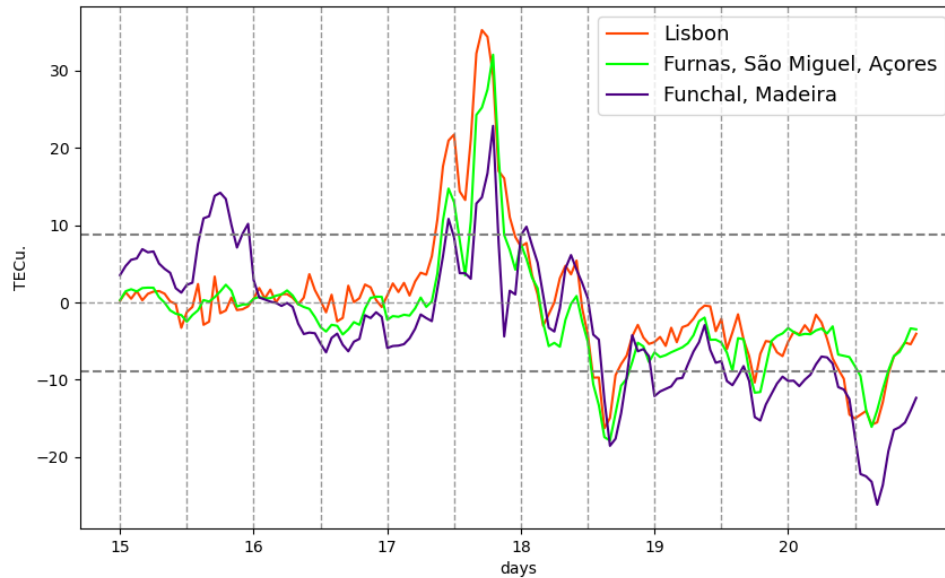
Figure 5.6: Δ TEC values over the period of 15-20th of March 2015, for all the locations studied.

the rest of the month for Lisbon and Azores. During the second day of the geomagnetic storm, every region shows a coherent TEC mean decrease as a consequence of the negative ionospheric storm. Two days after the eclipse, the mean of TEC returned to the quiet values (20<TECu<30). The amplitude of the daily TEC variation (represented by the EOF1, Figure 5.8) increased to about 0.25 in Madeira and 0.33 in Lisbon and Azores during the first day of the storm. On the day of the negative phase of the storm, daily amplitudes were as low as 0.10 for all the locations. After a recovery of the normal amplitudes (0.14 < EOF1 < 0.21), on the day of the eclipse, there was another decrease in the daily amplitude (EOF1 ∼ 0.10).

The studied geomagnetic storm caused a positive-negative ionospheric storm at all studied locations, which is seen in Figures 5.6 - 5.8. The positive TEC variations (Figure 5.6) were stronger in Lisbon and weaker in Madeira. The negative phase was similar for the three
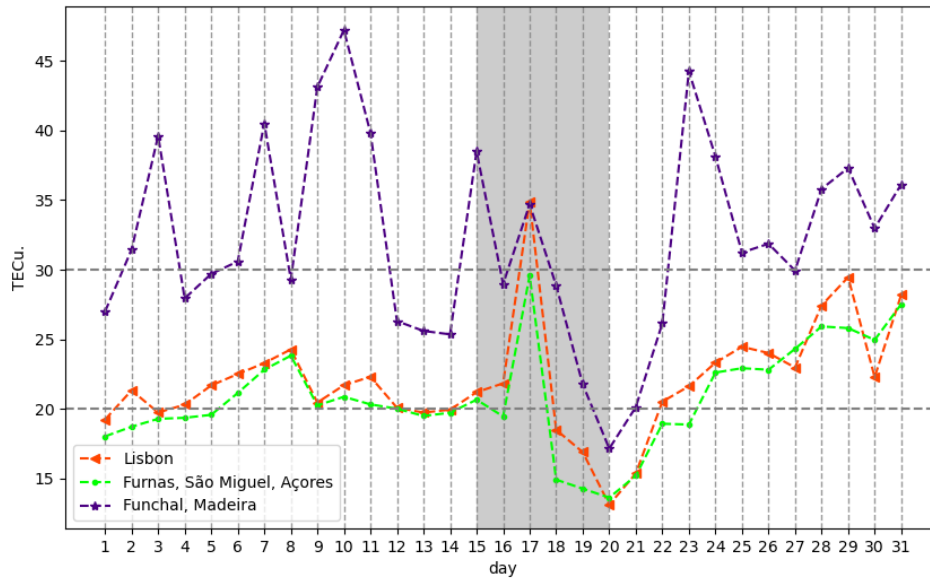
Figure 5.7: Daily mean TEC for March for all the locations.
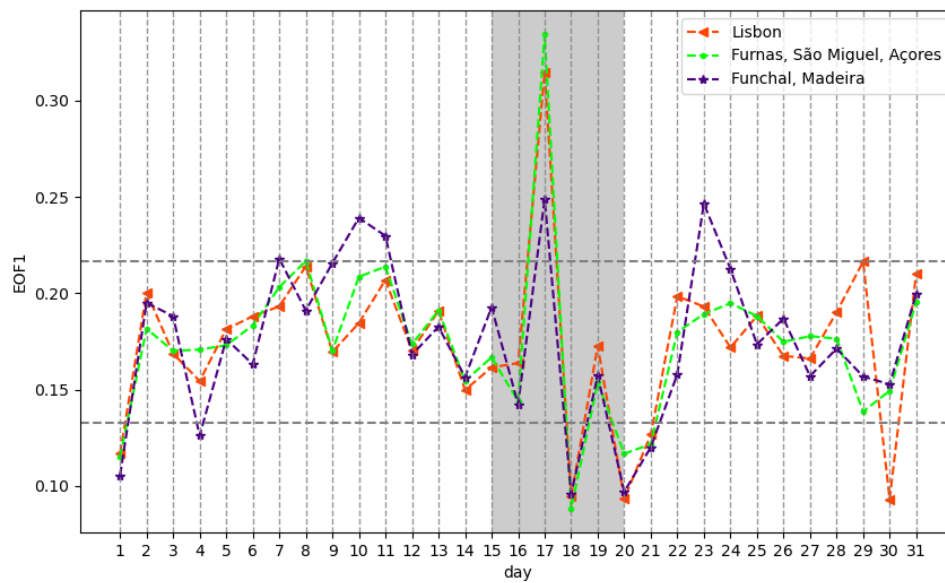
Figure 5.8: EOF1 for March for all the locations.

regions. The effect of the eclipse on TEC on 20th of March was also similar for Lisbon, Madeira, and Azores.

Effects on infrastructure:

According to [4], authors point this storm as the cause for the observed degradation of the position quality and accuracy of GNSS Also, there were long-distance radio communication disruptions [52].

Geomagnetic storm of 22nd-23rd of June 2015

Space weather conditions:

The second most severe storm of this solar cycle ($Dst_{min} = -198$ nT, Figure 5.9) occurred in June. The eruption of a sunspot's filament on the first day of the storm may be the cause of an M-class solar flare and two CMEs followed by a third one [4]. The geomagnetic storm arrived at Earth in the afternoon of 22nd of June. During the recovery phase of this storm another disturbance (Dst=-70 nT seen in Figure 5.9) started around midday of 25th of June. It was caused by a CME that occurred on 21st of June [54].
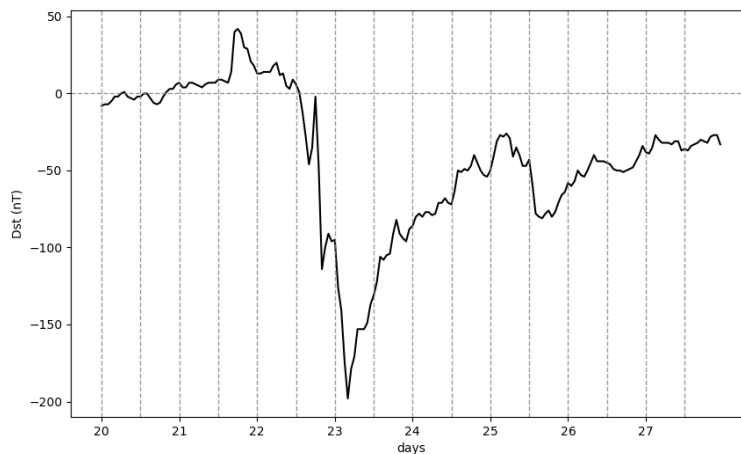
Figure 5.9: Dst over the period of 20-25th of June 2015.

TEC response:

TEC variations were regular until the arrival of the storm when there was a TEC increase (10 to 23 TECu in Δ TEC from Figure 5.10). The storm first affected Madeira and Lisbon (19:00 UTC) and later the Azores (23:00 UTC). During the next day, TEC had a decrease of around 20-40 TECu, the negative phase of the ionospheric storm. The ionospheric disturbance from 25th of June is seen in the plot for Δ TEC, Figure 5.10 as a positive ionospheric storm.
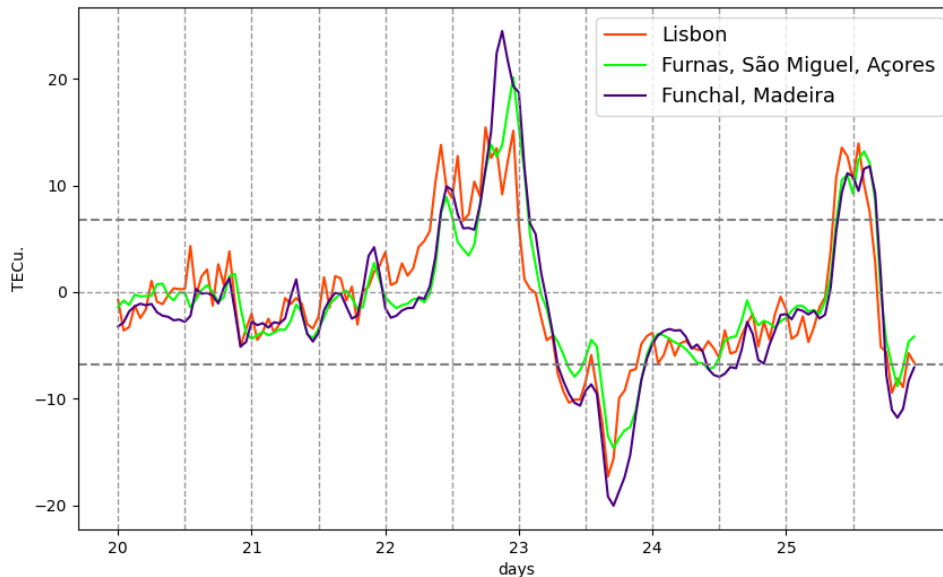
Figure 5.10: Δ TEC values over the period of 20-25th of June 2015, for all the locations studied.

The daily mean TEC variations in June are coherent for the three studied locations, as one can verify by Figure 5.11. Also, during the first two weeks of this month, there was an increase in the UV flux [55], which caused an increase in the ionization and has affected daily mean TEC values. However, the 22nd of June has a higher mean of TEC value, and the 23rd has the lowest mean of the month as a consequence of the geomagnetic storm. The day

of the second storm presented a smaller increase of the daily mean TEC (TEC mean $< \sigma$, Figure 5.11) since the ionosphere was still in the recovery process from a negative storm.
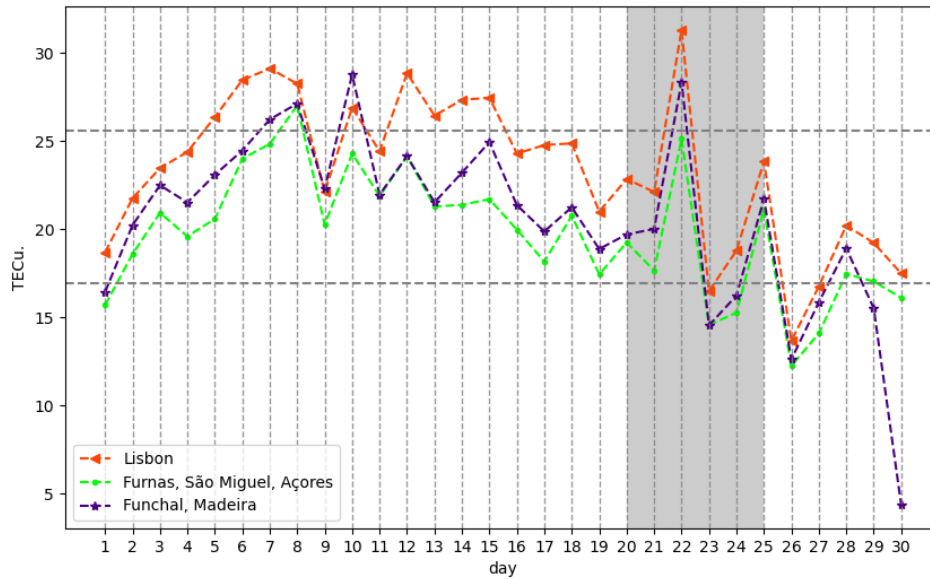
Figure 5.11: Daily mean TEC for June for all the locations.

The amplitudes of the daily TEC variation (EOF1) increased during the positive storm phase (22nd of June), decreased during the negative phase, to negative values ~ 0.04, and increased again during the secondary (25th of June) storm, as one can see from the EOF1 plot in Figure 5.12. The second storm's amplitude was larger at Lisbon, as it is seen also in Figure 5.12.

It is noticeable from the Δ TEC plot, Figure 5.10, that the southern region of Madeira presents a stronger variation during the two days of the storm, but the daily mean TEC was higher at Lisbon (Figure 5.11).
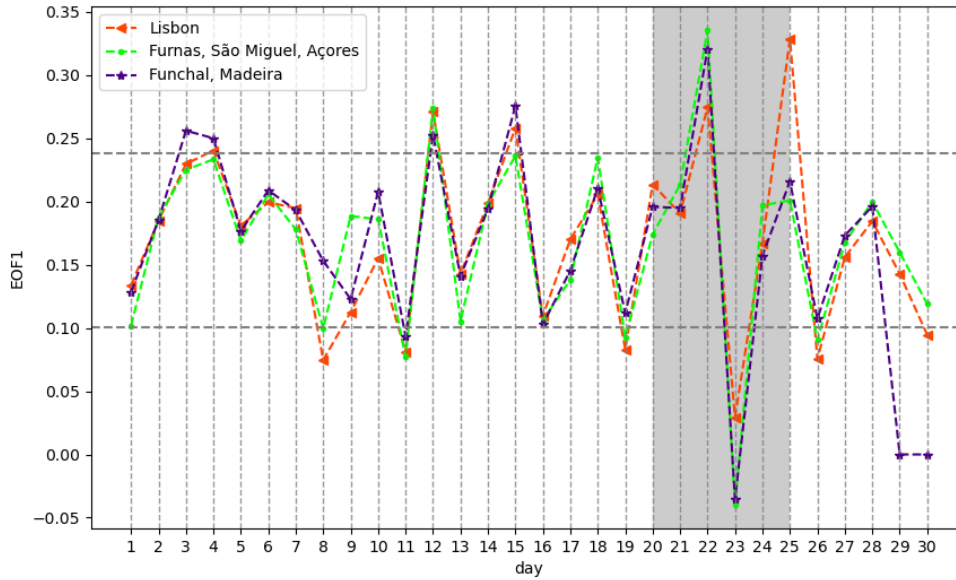
Figure 5.12: EOF1 for June for all the locations.

Geomagnetic storm of 5-10th of October 2015

Space weather conditions:

Fast solar wind speed from a coronal hole disturbed the geomagnetic field, causing a storm on 4th and 5th of October that was not a very strong one (Dst ∼ -65 nT, Figure 5.13). Another coronal hole caused the geomagnetic storm on 7th of October [54]. Dst reached its minimum of -130 nT on 7th of October (Figure 5.13).
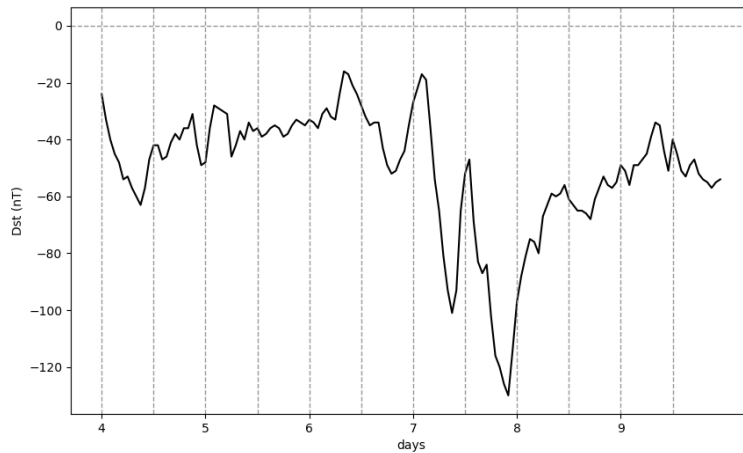
Figure 5.13: Dst over the period of 5-9th of October 2015.

TEC response:

Due to the absence of the RENEP and RAEGE-Az data for the second half of 2015 and the whole 2016, the effect of the geomagnetic storms on the ionosphere during this time interval was studied using only TEC data for Lisbon.

These two geomagnetic storms caused a decrease in the ionisation, and therefore, the ionospheric storms were negative. Analysing Δ TEC in Figure 5.14, it is possible to see that during 5th of October, there was a decrease in TEC (Δ TEC $\sim$ -9 TECu), but for 7th of October, the decrease was larger (Δ TEC $\sim$ -12,5 TECu) and prolonged to the following day.

The daily mean TEC during this month was low (11 < TEC mean < 16 TECu). During the first storm, on 4th of October, the daily mean TEC decreased to $\sim$ 11 TECu and was between 10-12 TECu during the following five days. The daily mean TEC plot is shown in Figure 5.15, and it reaches its minimum value on the day of the strongest storm, 7th of October. The recovery phase of this storm lasted about seven days. The amplitudes of the daily variations are shown by the EOF1 plot in Figure 5.15. The EOF1 confirms the
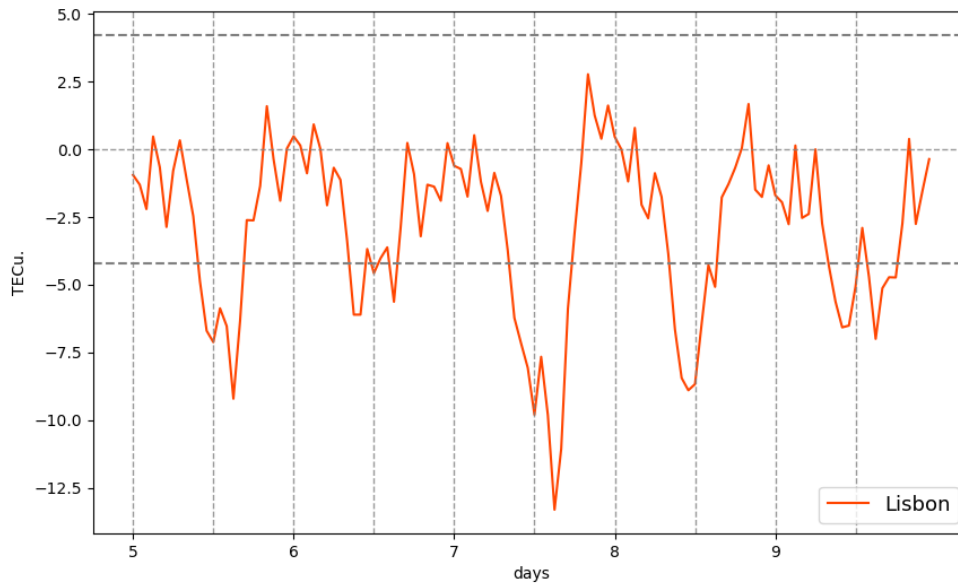
Figure 5.14: Δ TEC values over the period of 5-9th October 2015, for Lisbon.
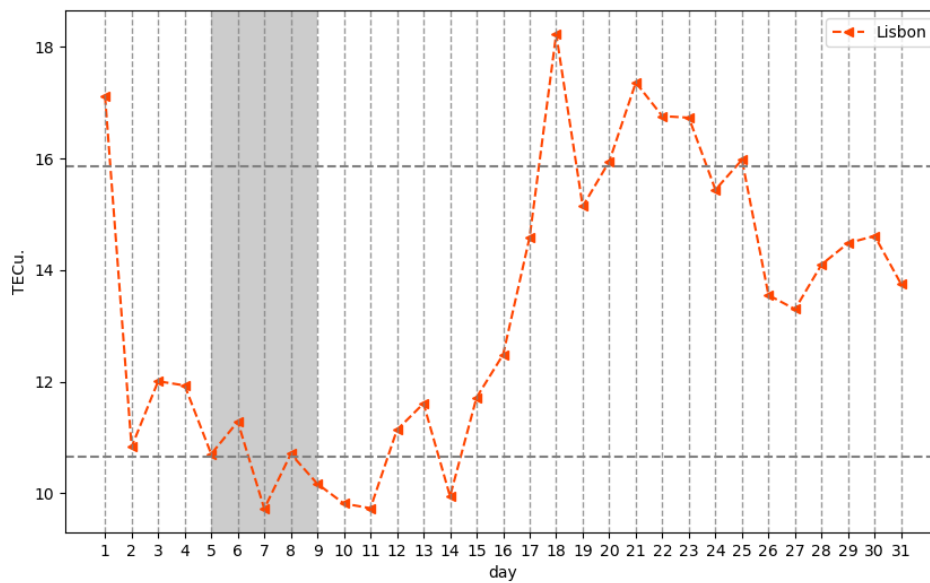
Figure 5.15: Daily mean TEC for October for Lisbon.

negative ionospheric storm of 7th of October, and its changes through the month are similar to the daily mean TEC (Figure 5.15). By the end of the third week of the month, the daily amplitudes values were higher (EOF1 > 2σ) even though the geomagnetic field was not very disturbed (Dst = -56 nT).
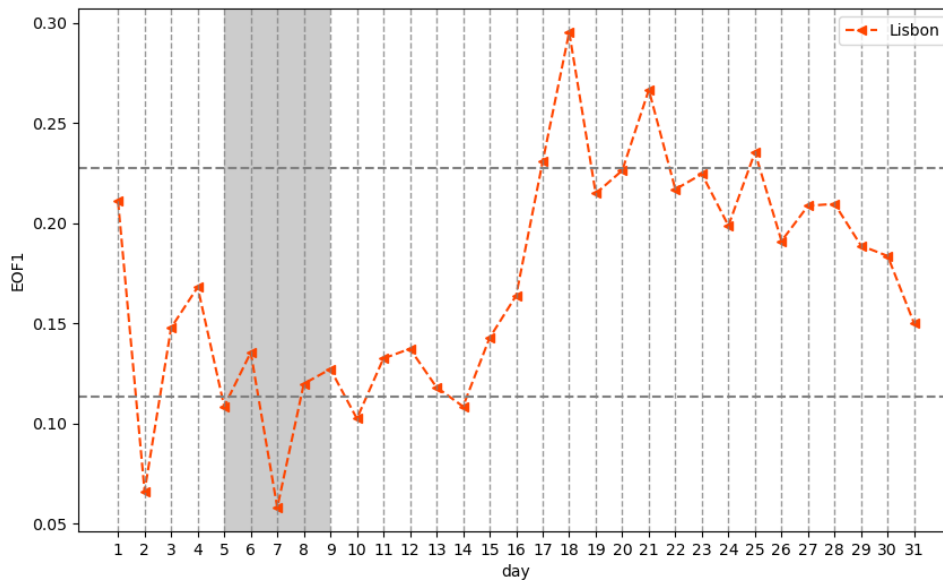
Figure 5.16: EOF1 for October for Lisbon.

Geomagnetic storm of 20th of December 2015

Space weather conditions:

The last big storm (Dst=-166 nT, as in Figure 5.17) of 2015 was in December and caused by a CME from 19th of December that hit Earth on 20th of December [52].

TEC response:

On the day of the storm, TEC increased by several TECu. From the analysis of Δ TEC shown in Figure 5.18, the ionospheric storm was positive and characterized by an increase in 11 TECu. It had a quick recovery since there were no significant geomagnetic disturbances

in the days before and after the storm.
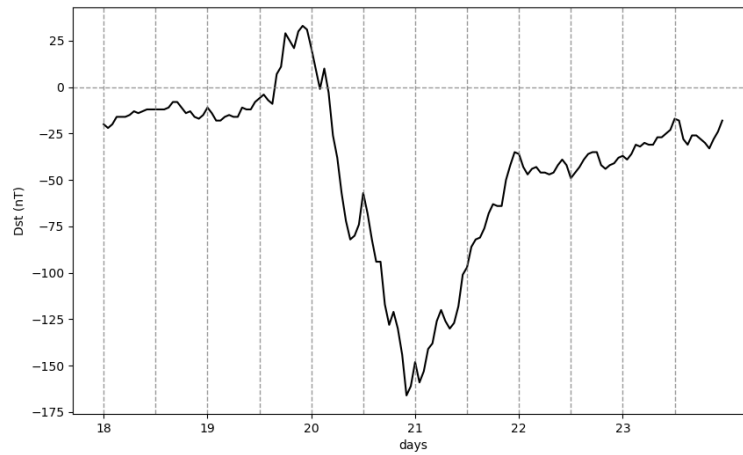
Figure 5.17: Dst over the period of 18th-23rd of December 2015.

Figure 5.18: Δ TEC values over the period of 18th-23rd of December 2015, for Lisbon.
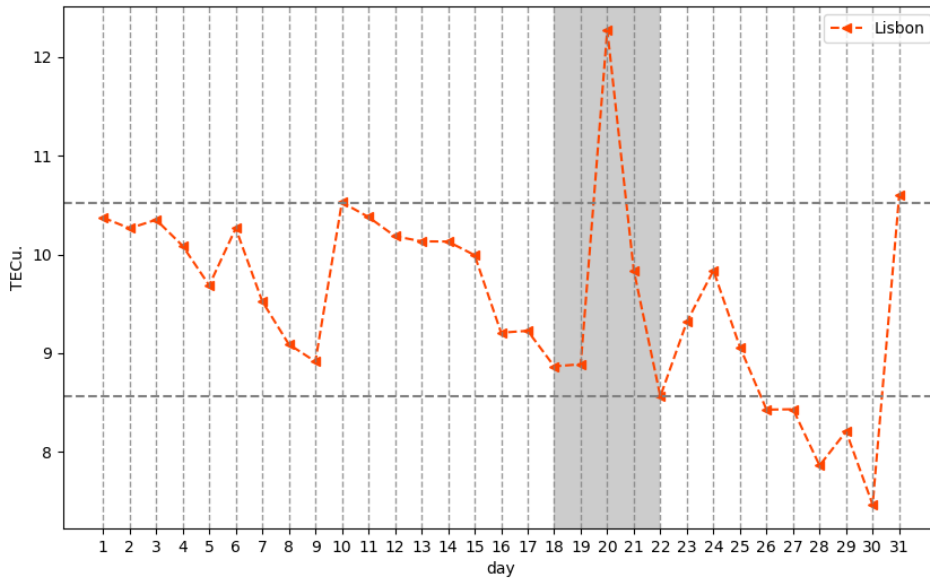
Figure 5.19: Daily mean TEC for December for Lisbon.
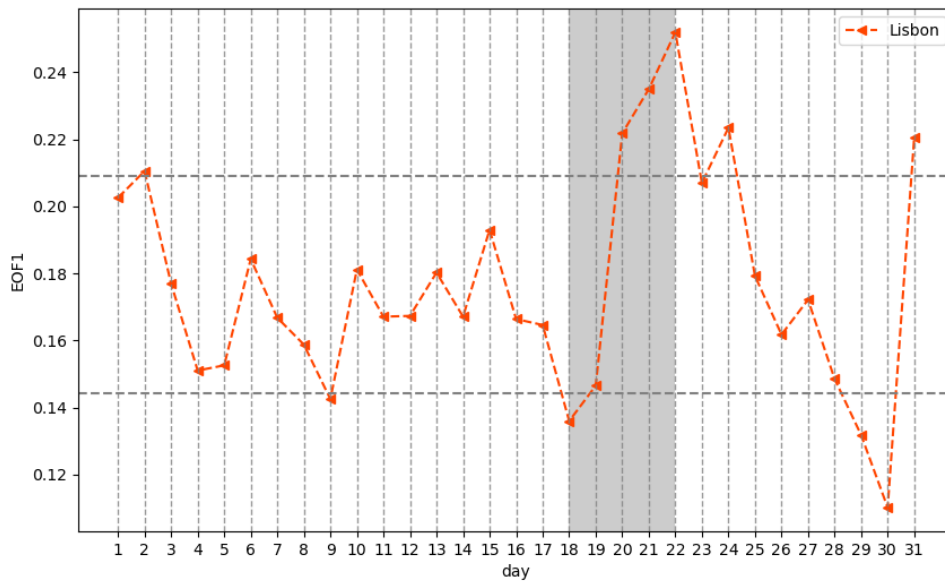
Figure 5.20: EOF1 for December for Lisbon.

The daily mean TEC was about 12 TECu on the day of the storm, the highest value during the entire month, as it can be seen in Figure 5.19. On the other hand, EOF1, in Figure 5.20 increased consecutively during 20th, 21st and, 22nd of December.

Geomagnetic storm of 20th-21st January 2016

Space weather conditions:

A fast solar wind from a coronal hole caused a geomagnetic storm on 20th of January and the following day [54]. Dst variations during these days are shown in Figure 5.21.
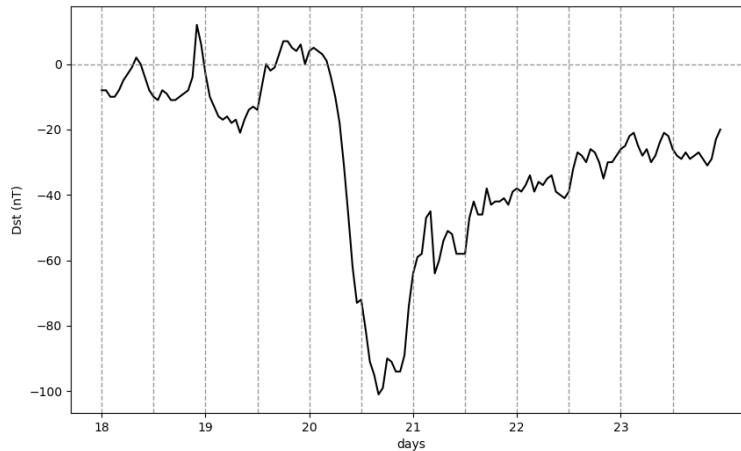
Figure 5.21: Dst over the period of 18th-23rd of January 2016.

TEC response:

An increase of 12 TECu (see Δ TEC in Figure 5.22) on 20th of January is the consequence of this geomagnetic storm. On the previous day, around 23:00 UTC, TEC started to increase. The recovery of TEC to the quiet level (-3 < Δ TEC < 3 TECu) lasted only about three hours on 21st of January.

The daily mean TEC was always between 7 and 10.5 TECu, with the exception of 20th of January, when it reached 14 TECu. The TEC means can be seen in Figure 5.23.
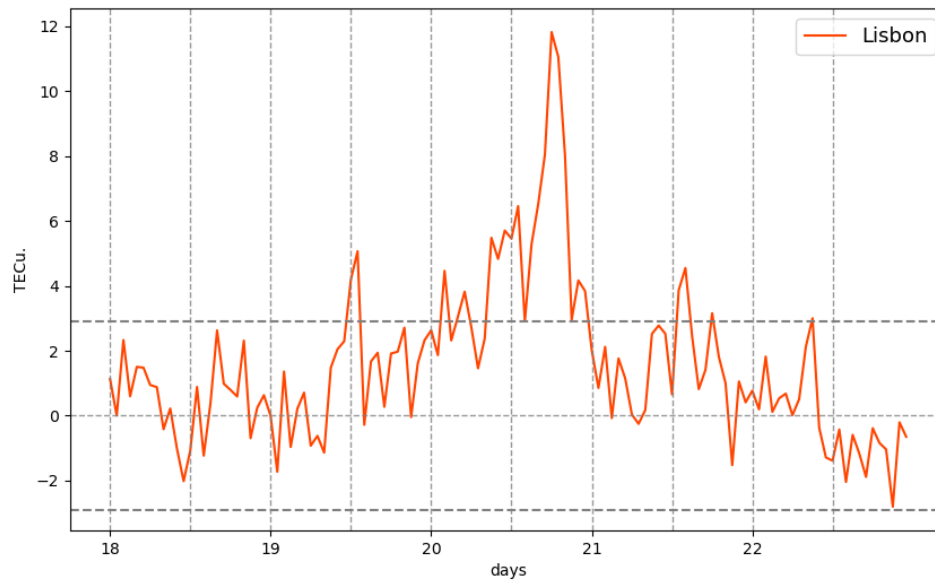
Figure 5.22: Δ TEC values over the period of 18th-23rd of January 2016, for Lisbon.
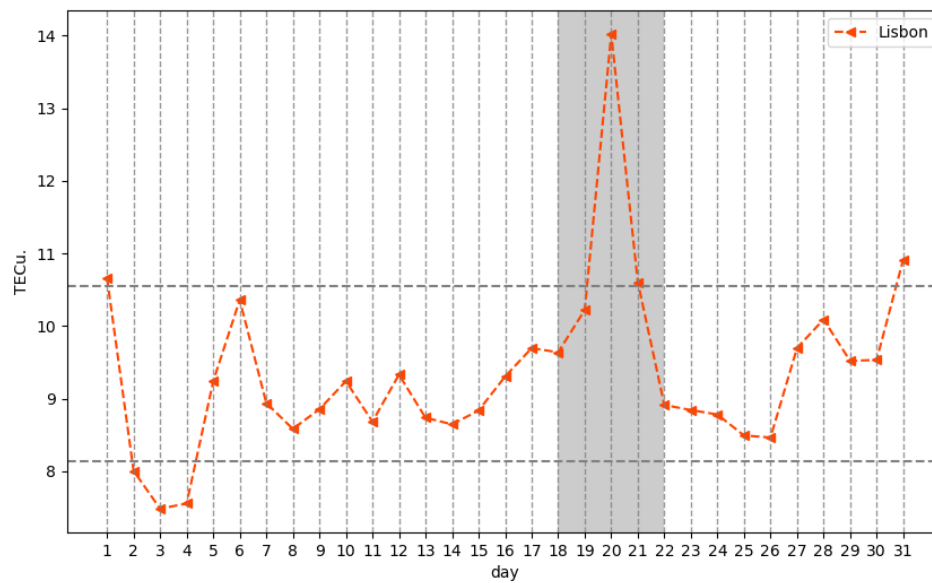
Figure 5.23: Daily mean TEC for January for Lisbon.

The amplitudes of the daily variation increased on 19th, 20th, and 21st of January (EOF1 ∼ 0.23). The EOF1, seen in Figure 5.24, also increased on the 13th, however, there was no disturbance in the geomagnetic field on that day.
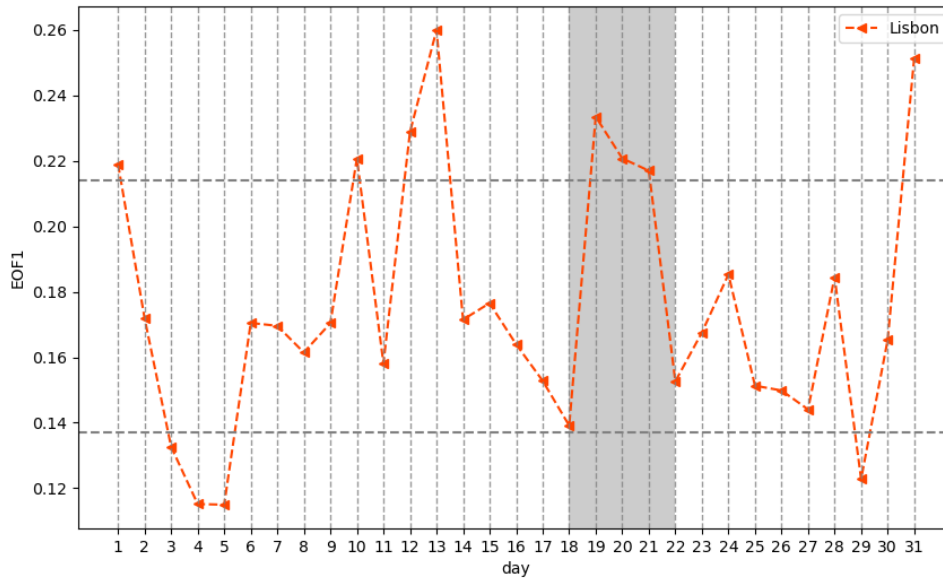
Figure 5.24: EOF1 for January for Lisbon.

Geomagnetic storm of 6th of March 2016

Space weather conditions:

A geomagnetic storm occured (Dst = -95 nT as seen in Figure 5.29) after the day a coronal hole was spotted on the Sun, [54]. On 10th of March, a small (Dst ∼ -30 nT) geomagnetic storm was detected, caused by another coronal hole.
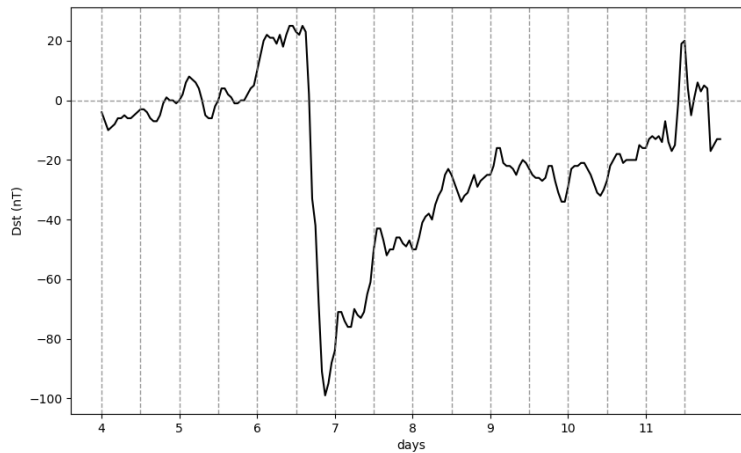
Figure 5.25: Dst over the period of 4-8th of March 2016.

TEC response:

The variations of TEC are above the quiet TEC values (-2.7 < Δ TEC < 2.7 TECu) as seen in the Δ TEC plot shown in Figure 5.26 on 6th of March. TEC started to increase before 6th of March and reached Δ TEC = 12.5 TECu in the late afternoon of this day, leading to a positive ionospheric storm.

The daily mean TEC's largest value was on 6th of March, the day of the geomagnetic storm, as is seen in Figure 5.27. Later, there was another increase of the daily mean TEC on 10th of March, probably caused by the second and much smaller geomagnetic storm. The amplitudes of the daily variation for 6th of March are small, however, the effects on TEC during 10-11th of March are seen in Figure 5.28 by an increase of the EOF1.
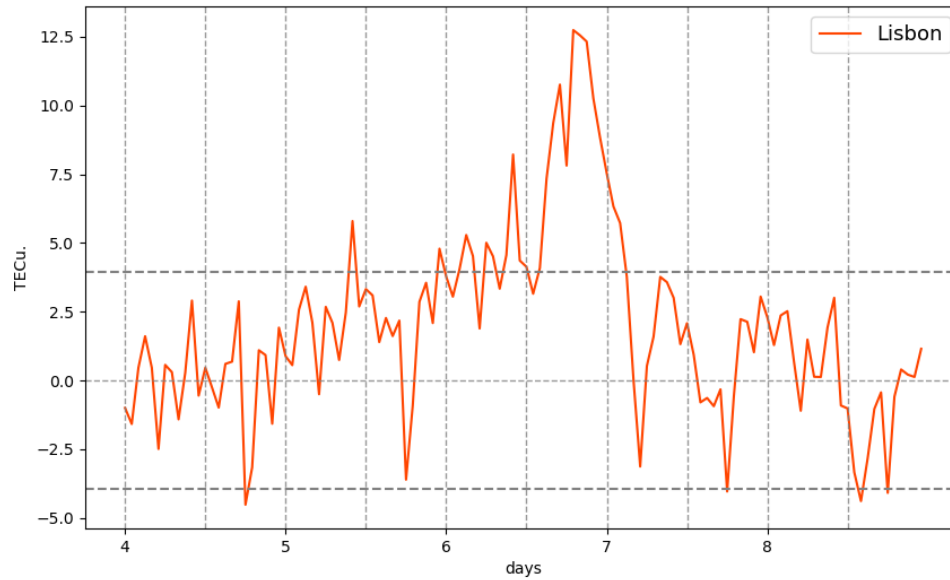
Figure 5.26: Δ TEC values over the period of 4-8th of March 2016, for Lisbon.
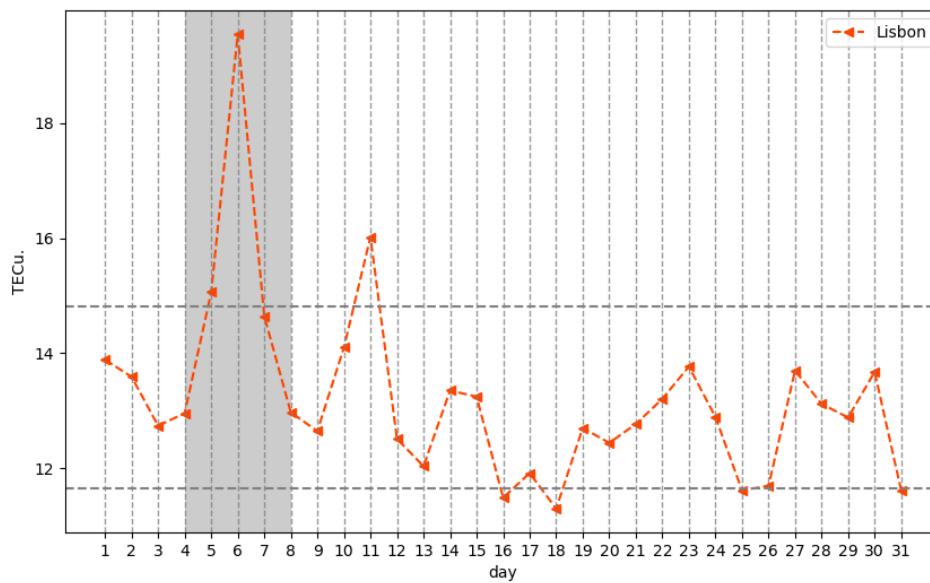
Figure 5.27: Daily mean TEC for March for Lisbon.
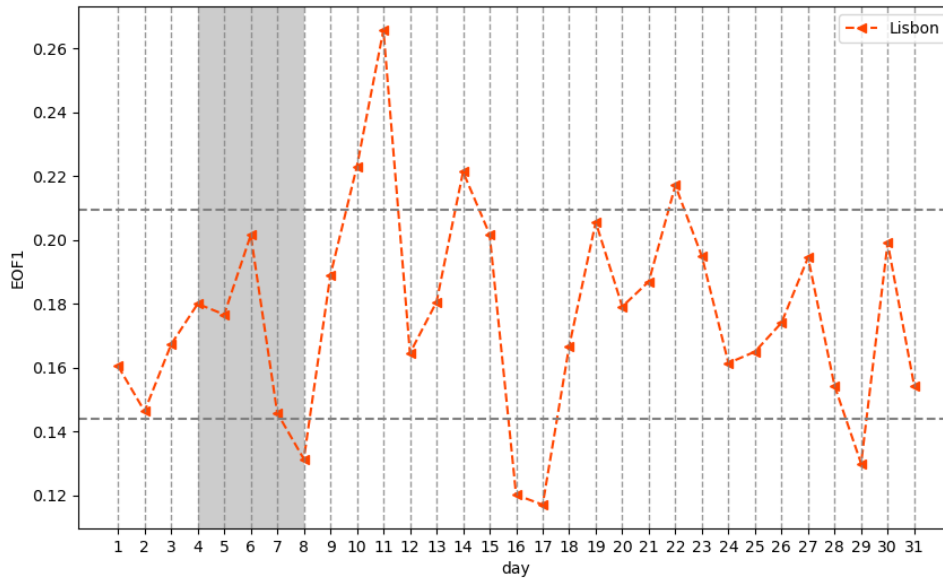
Figure 5.28: EOF1 for March for Lisbon.

Geomagnetic storm of 4th of April 2016

Space weather conditions:

This storm was caused by high-speed solar wind from a coronal hole [54], and the Dst index reached values < -50 nT during the night from 2nd to 3rd of April 2016 (Figure 5.29).

TEC response:

Ionospheric disturbances were only seen on 4th of April and consisted of a decrease in TEC, Figure 5.30. The storm was characterized by a Δ TEC = -8 TECu decrease. On 5th of April, ionization was still low, and Δ TEC < -2σ.

The decrease in TEC is also seen in the overall TEC means for this month as a daily mean TEC = 10 TECu for 3rd of April, which is seen in Figure 5.31, and a decrease of around 0.100 in EOF1, as shown by Figure 5.32.
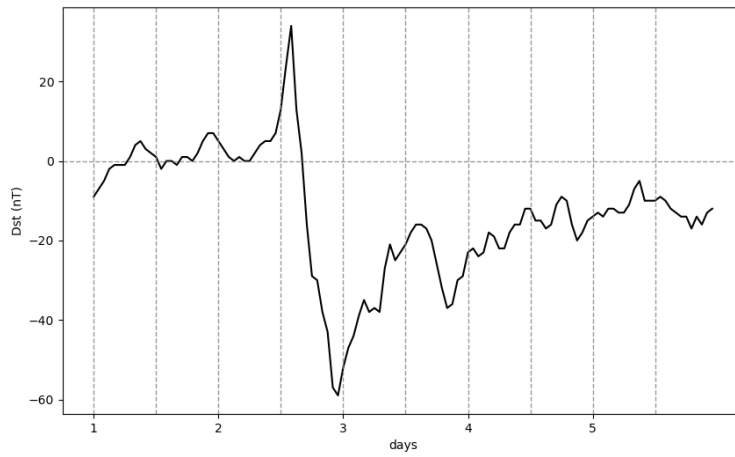
Figure 5.29: Dst over the period of 1st-5th of April 2016.
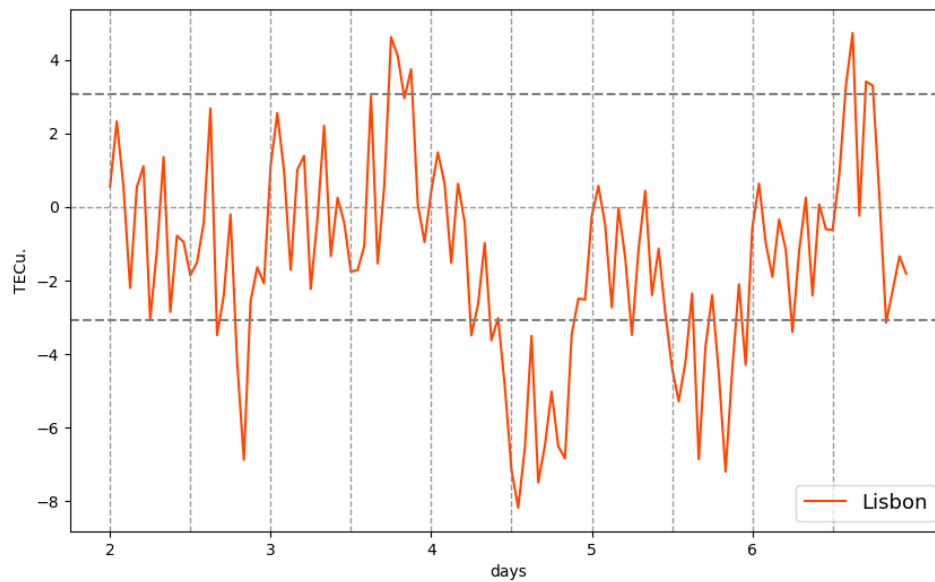
Figure 5.30: Δ TEC values over the period of 1st-5th of April 2016, for Lisbon.
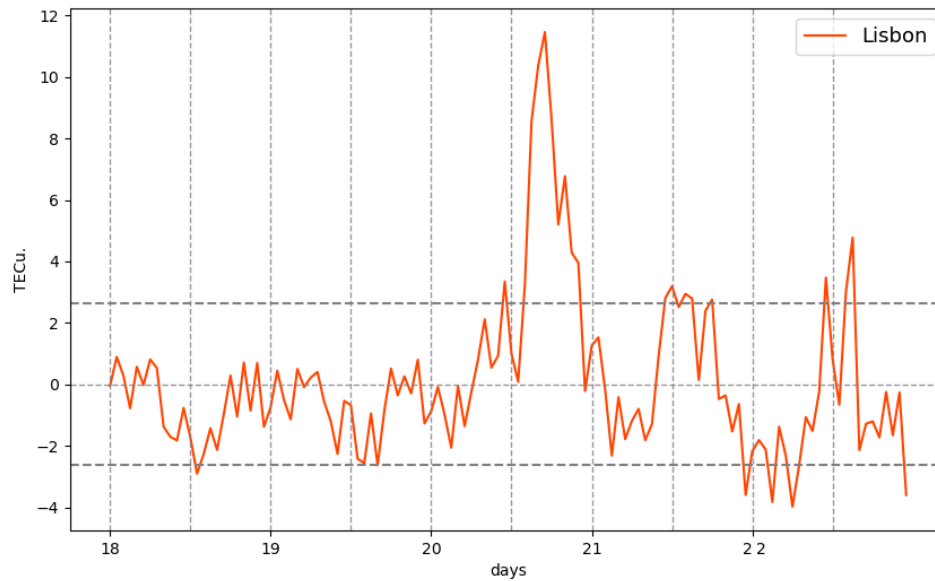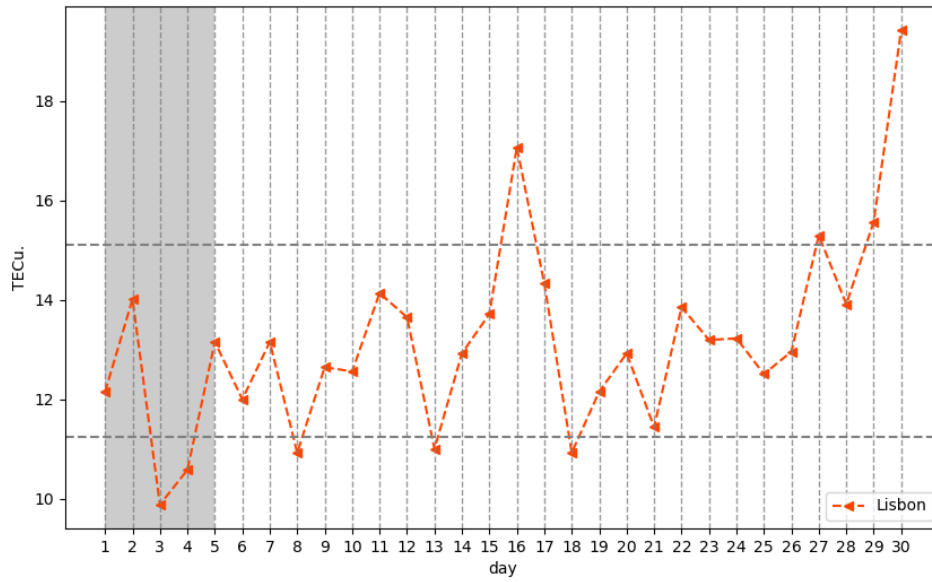
Figure 5.31: Daily mean TEC for April for Lisbon.
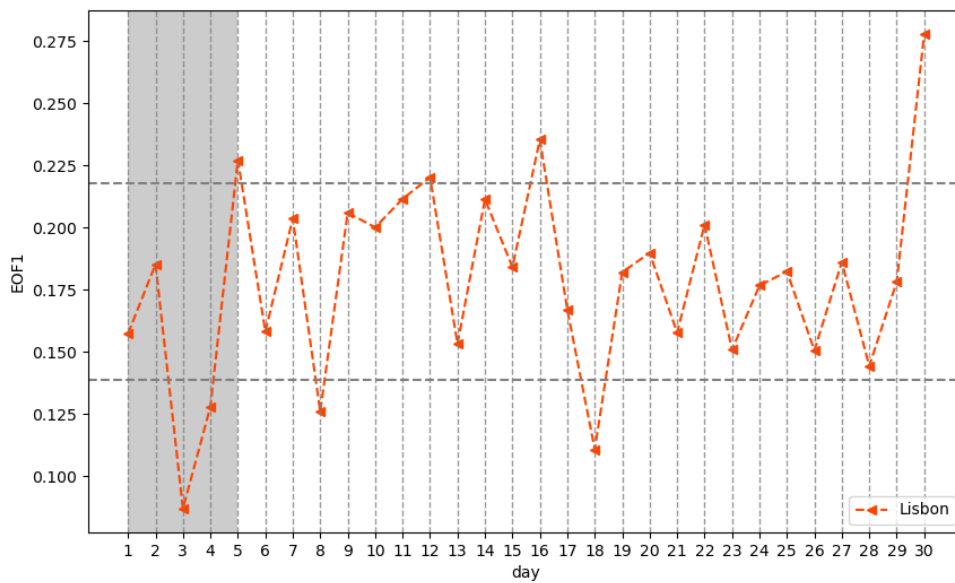
Figure 5.32: EOF1 for April for Lisbon.

Geomagnetic storm of 27-28th of May 2017

Space weather conditions:

The geomagnetic storm from 27th to 29th of May 2017 was caused by a CME on 23rd of May [4] that disturbed the geomagnetic field (Dst = -125 nT, Figure 5.33).

TEC response:

The daily TEC variations during this storm are different from the previously analysed storms, as they are characterized by a negative part occurring first on the afternoon of 28th of May, followed by a positive storm on the afternoon of the 29th. This might have occurred due to the fact that the geomagnetic storm took place during the night of 27th of May when TEC is usually low, and when the ionospheric storm peaked, it was already the next day [4].
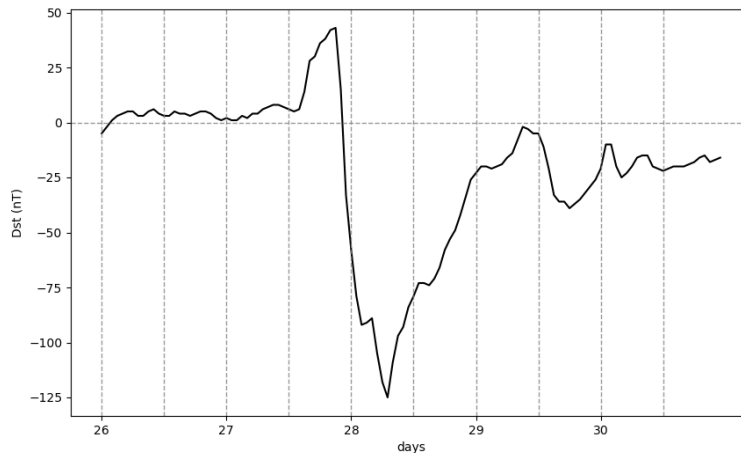
Figure 5.33: Dst over the period of 26-30th of May 2017.

Δ TEC ploted in Figure 5.34 shows the negative storm, Δ TEC < -2σ on 28th of May, and the positive storm, Δ TEC > 2σ on 29th of May. The decrease in TEC is larger for Madeira (Δ TEC ∼ -8 TECu) than for the other two locations (Δ TEC ∼ -5 TECu). For the positive phase of the storm, the increase is similar for the three locations, however, the

TEC increase started first at Lisbon, then at the Azores, and only after at Madeira.
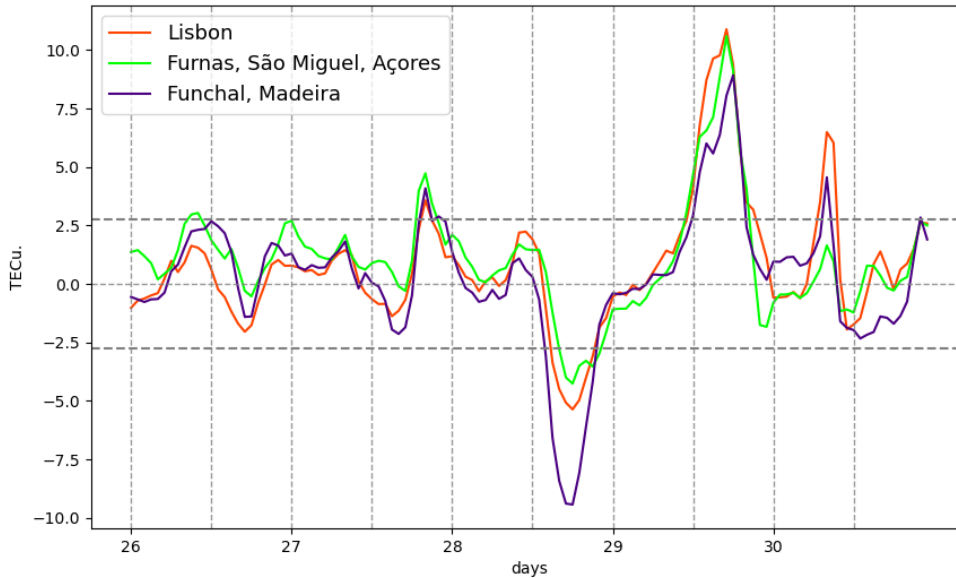
Figure 5.34: Δ TEC values over the period of 26-30th of May 2017, for all locations.

The daily mean TEC was high during the middle of May, which might have been caused by an increase in the UV flux. During the two days of the storm, represented by the grey area of the daily mean TEC in Figure 5.35, there is a quick variation between a low value for the mean of the day of the storm and a high value on the next day. These correspond to the negative phase, TEC mean ∼ 7 TECu, and positive phase, TEC mean ∼ 12 TECu, for all the locations studied.

The amplitudes of the daily variations are coherent with the occurrence of a negative-positive storm. EOF1, which represents these amplitudes, is plotted in Figure 5.36 It shows an amplitude variation from 0.08 at the negative phase to 0.25 (Madeira) and 0.33 (Lisbon and Azores).
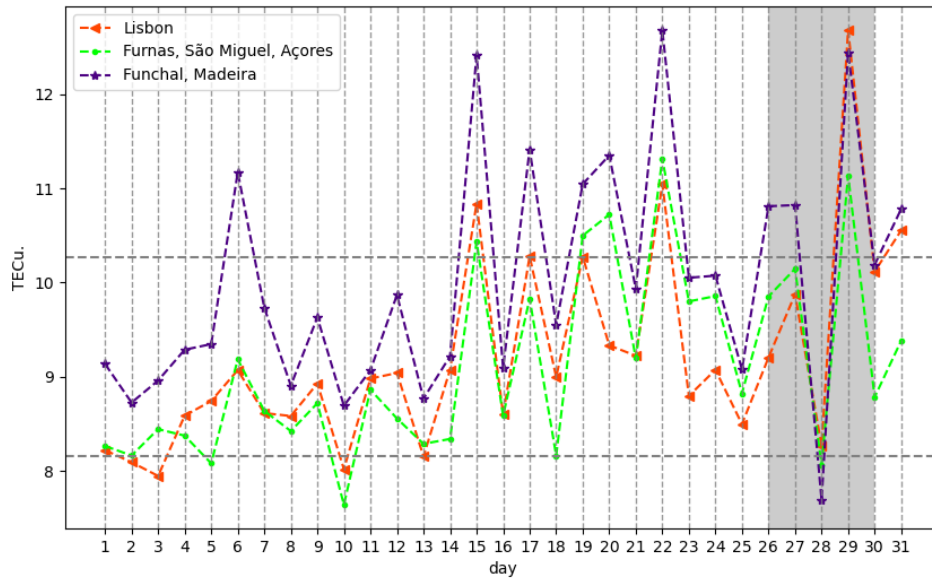
Figure 5.35: Daily mean TEC for May for all locations.
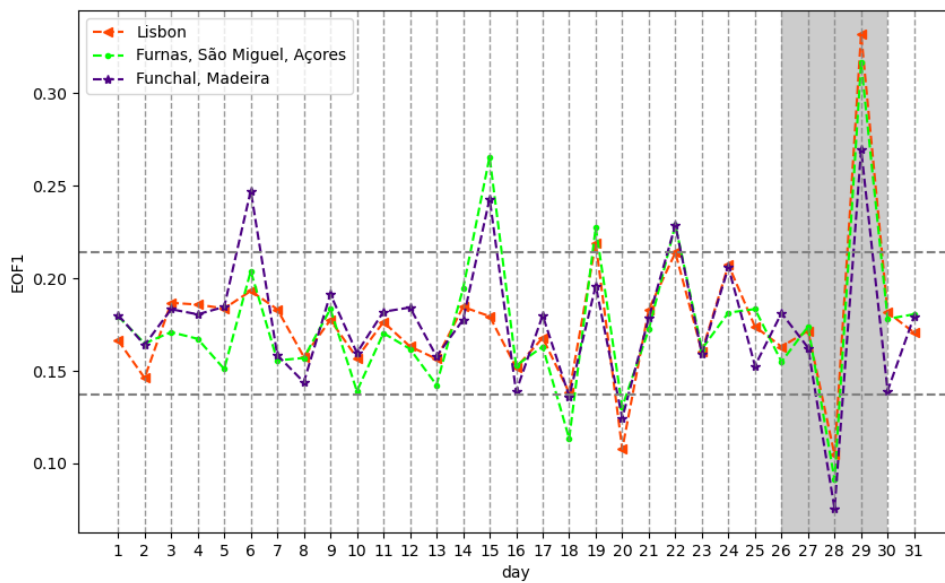
Figure 5.36: EOF1 for May for all locations.

The negative part of the storm was stronger at Madeira (ΔTEC > -3σ), and the positive ionospheric storm was stronger for the Azores and Lisbon (ΔTEC < 3σ). The locations in an eastern longitude show an increase in TEC for 30th of May, although geomagnetic conditions were quiet (Dst > - 50 nT), so it is probably related to long-living post-sunset equatorial plasma bubbles that moved northward [4].

Geomagnetic storm of 7th of September 2017

Space weather conditions:

This geomagnetic storm (minimum Dst = -122 nT, as it is seen in Figure 5.37) was caused by a series of events on the Sun, including M and X flares and CMEs [4].
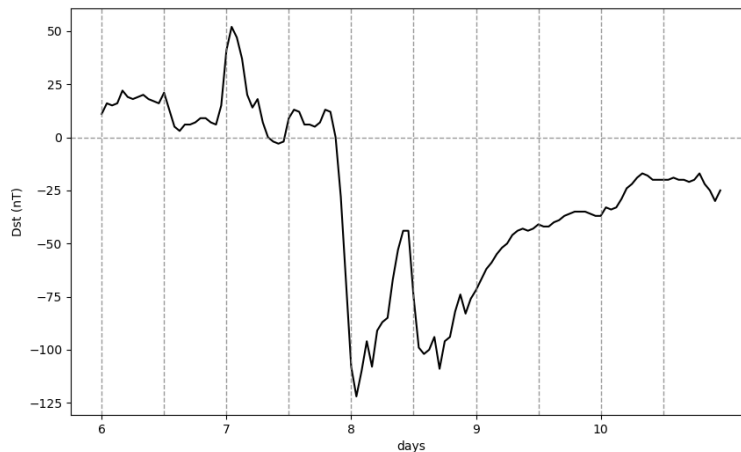
Figure 5.37: Dst over the period of 6-10th of September 2017.

TEC response:

The daily TEC variations are characterized by an increase of TEC on 7th of September afternoon and evening. During the night, TEC returned to lower (quiet) values (Dst also increases, as it is clearly seen in figure 5.37), but in the morning of 8th of September, ionization began to rise again. This TEC increase was followed by a decrease during the afternoon

of 8th of September. These variations are well illustrated by Δ TEC, plotted in Figure 5.38. The increase of the 7th of September was a positive ionospheric storm, much stronger at Madeira (Δ TEC $\sim$ 14 TECu) than at Azores and Lisbon (Δ TEC $\sim$ 10 TECu). The second increase is a new positive ionospheric storm, Δ TEC $\sim$ 7 TECu in Madeira and Lisbon, and lower, Δ TEC $\sim$ 5 TECu in the Azores. The negative phase of this ionospheric storm was similar for the three locations, Δ TEC $\sim$ -3 TECu. The daily mean TEC, in Figure 5.39,
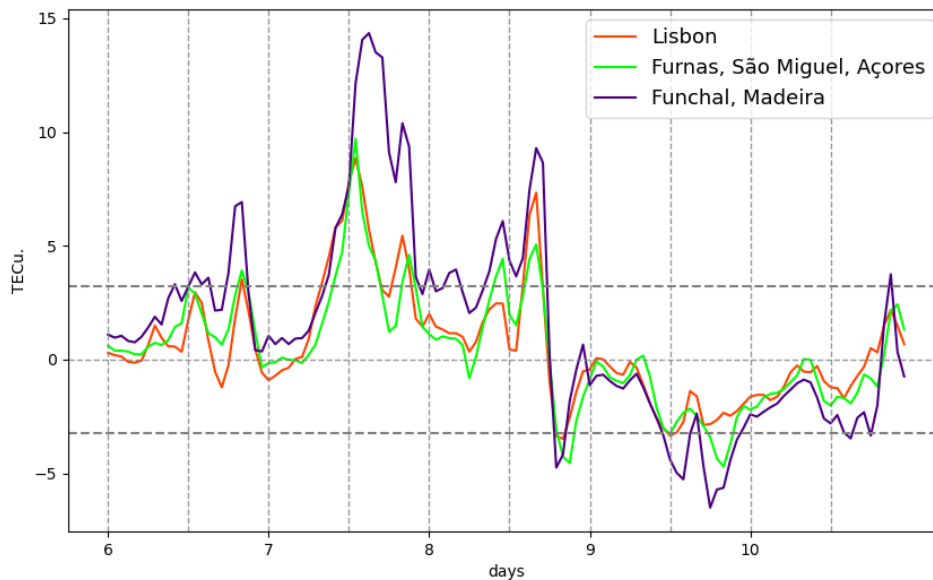
Figure 5.38: Δ TEC values over the period of 6-10th of September 2017, for all locations.

shows the increase during 6th, 7th, and 8th of September. The maximum of the daily mean TEC mean occured on 7th of September and was more than 15 TECu at Madeira and more than 11 TECu at Azores and Lisbon. The negative phase of the storm is seen in the mean values on 9th of September: it is around 7 TECu for all the locations. The amplitudes of daily variations (EOF1) are very similar for the three locations. Figure 5.40 shows that EOF1 was between 0.25 and 0.31 during the positive ionospheric storm, and during the negative
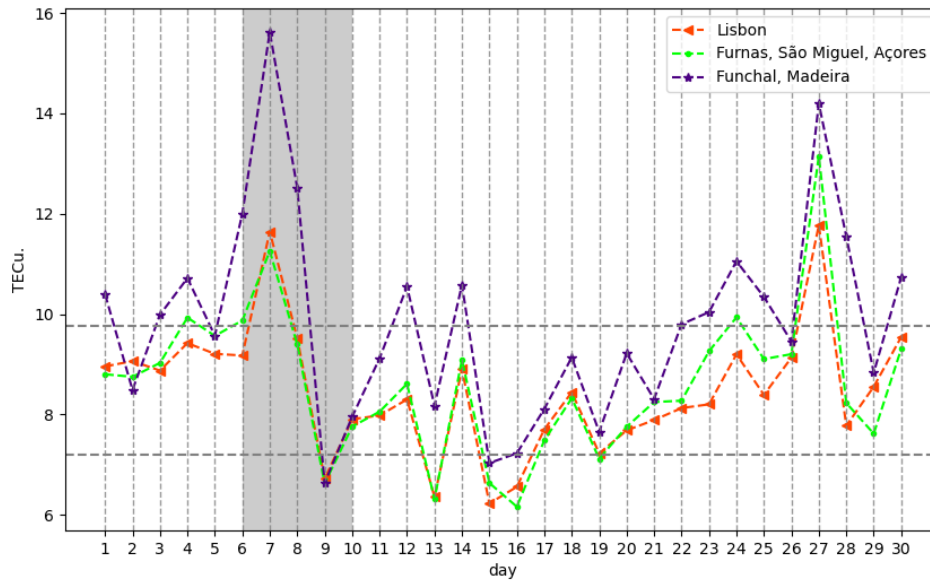
Figure 5.39: Daily mean TEC for September for all locations.

phase of the second storm, EOF1 = 0.14.

From Figures 5.38 to 5.40, one can see that the storm was very different in amplitude for Madeira, Azores, and Lisbon. By the end of the month, both EOF1 and the means of TEC show some variations caused by a minor geomagnetic disturbance (Dst index was ∼ -56 nT).

Effect on infrastructure:

This storm had strong technological effects, affecting the positioning and accuracy of GNSS and the availability of EGNOS [4].
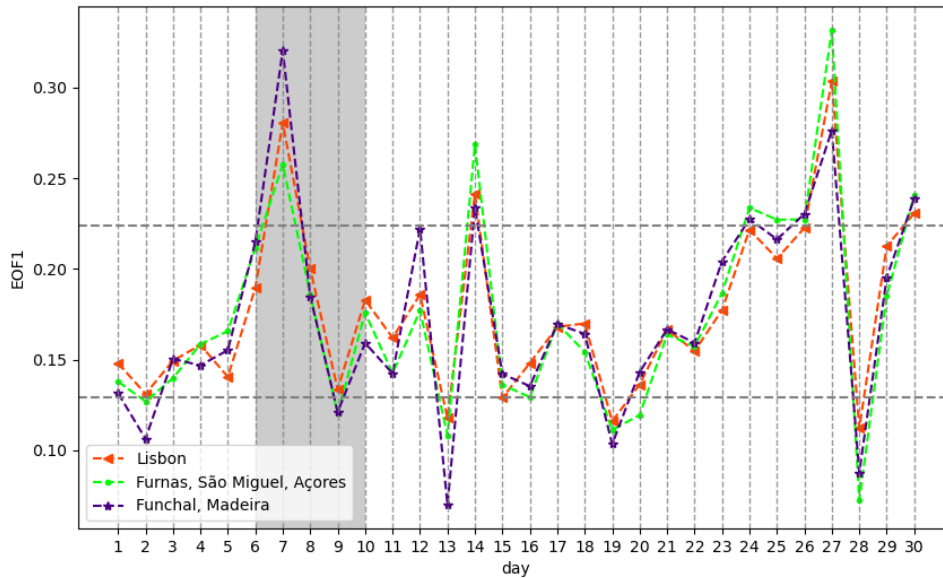
Figure 5.40: EOF1 for September for all locations.

Geomagnetic storm of 26th of August 2018

Space weather conditions:

The final storm (Dst = -175, Figure 5.41) of this analysis occurred due to a CME impacting Earth on 25th of August 2018 [4], and it was the only big geomagnetic storm of that year.

TEC response:

TEC started to increase in the afternoon of 25th of August (this is seen in the plot of Δ TEC, Figure 5.42) and reached its peak at around 00:00 UTC of the 26th. Then TEC decreased, leading to a negative ionospheric storm that peaked late on 26th of August. Both storm peaks were more prominent at Madeira, and the Δ TEC variations for all locations show a double peak. There are two additional ionospheric TEC increases over the quiet level: one on 24th of August, statistically significant only at Madeira, and another on 27th

of August for all regions. These disturbances can be related to disturbances in EEJ [4].
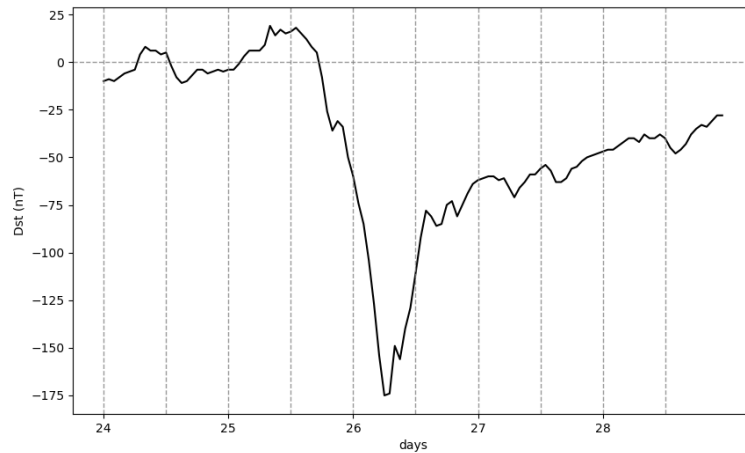
Figure 5.41: Dst over the period of 24-28th of August 2018.
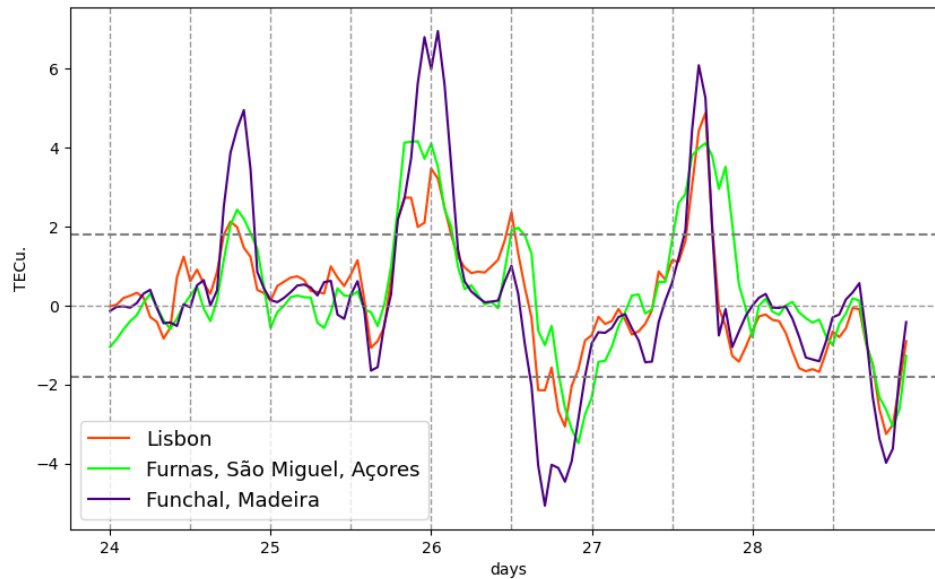
Figure 5.42: Δ TEC values over the period of 24-28th of August 2018, for all locations.

The daily mean TEC and EOF1 (Figures 5.43 and 5.44 respectively) both increased

between 25th and 27th of August. The positive-negative character of this storm is more prominent in the EOF1 variations than in the daily mean TEC. Concerning other days of the month, from 14th to 16th of August, there were significant changes in the daily mean TEC and EOF1, although Dst is above -50 nT. A deep decrease is seen for 12th of August in Madeira and for 21st and 22nd of August in Azores data, which are caused by low data quality and gaps in the observational data.
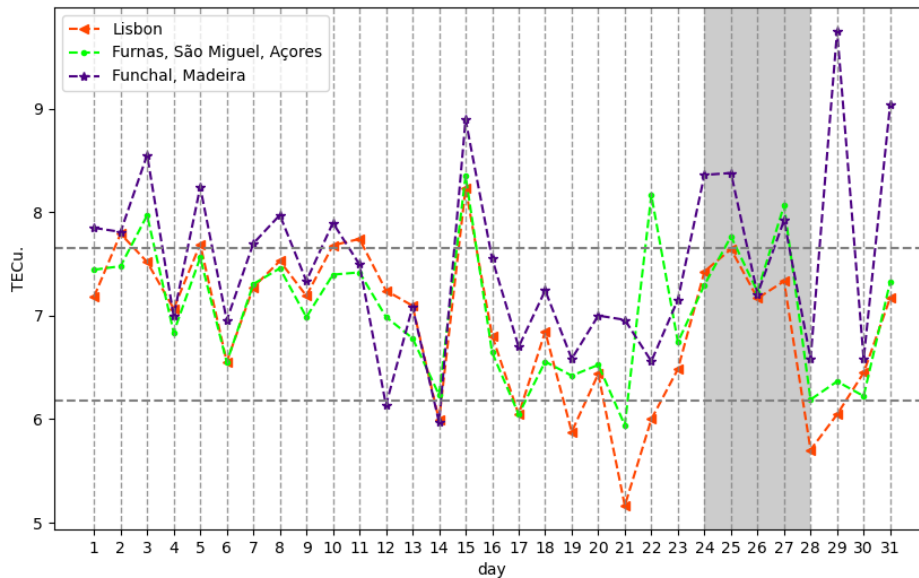
Figure 5.43: Daily mean TEC for August for all locations.
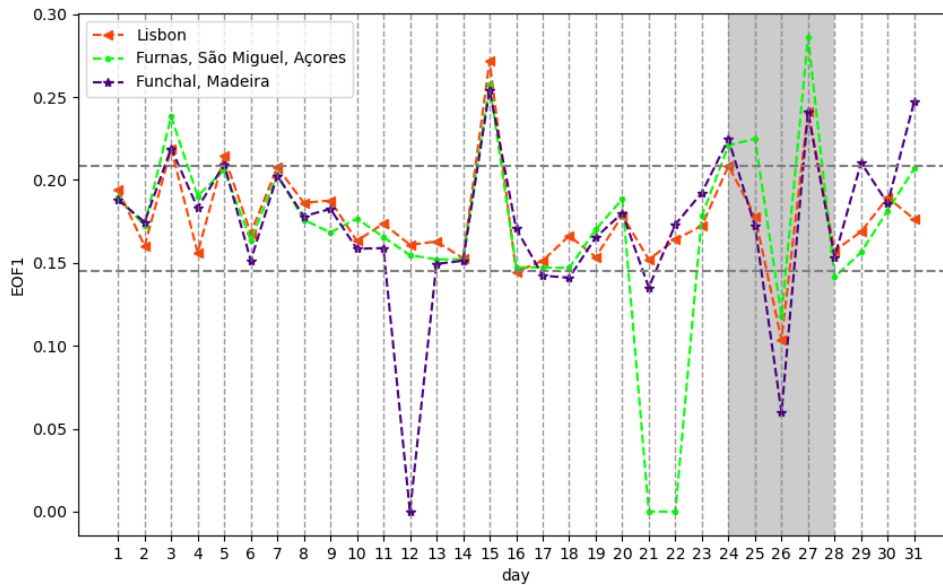
Figure 5.44: EOF1 for August for all locations.

Preliminary conclusions

The analysis of the TEC response to geomagnetic disturbances presented above shows that for most of the studied events, TEC variations were approximately synchronous between the three studied regions: Lisbon, Azores, and Madeira. The differences in time for TEC variations may be due to the one-hour delay in the local (solar) time for the western region (Azores). There are also differences in ionospheric responses between middle-latitude regions (Azores and Lisbon) and a more equatorial region (Madeira). TEC variations at Madeira are, generally, higher due to the larger insolation and proximity to the EEJ. The majority of geomagnetic storms caused positive or positive-negative ionospheric storms. The negative-positive storms (October 2015, April 2016, and May 2017) seem to be related to geomagnetic storms that started during the nighttime. Other events affecting TEC variations, such as a partial solar eclipse on 20th of March 2015, post-sunset equatorial plasma bubbles, and TIDs

[4] affected TEC variations during the studied time interval.

5.2 Solar flares

In the previous section, geomagnetic storms caused by CMEs and/or coronal holes were analysed. These CMEs are often caused or followed by solar flares. Also, flares may occur during geomagnetic storms. Therefore, to study the effect of the solar flares on the ionosphere, it is better to use only flares that took place during geomagnetically quiet time intervals.

The plots for Δ TEC, Figures 5.47 (a) and 5.49 (a), show examples of how ionospheric TEC vary during solar flares that occurred during the local daytime of geomagnetically quiet days (Dst > -50 nT).

Solar flares for March 2015

On 11th of March 2015, three M flares (at 7:18, 7:57, and 18:51 UTC) and an X flare (maximum at 16:22 UTC) were registered and are seen in Figure 5.45. The increase in ionization was observed in TEC for Lisbon, Δ TEC = 10 TECu, and Furnas, Δ TEC = 5 TECu.

The increase (to where the arrows point in Figure 5.47 (a)) is most probably the effect of the X flare and the last M flare (18:51 UTC), respectively. The morning M flares may have happened too early for the ionosphere to react to them. Figure 5.8 of EOF1 for 11th of March shows an increase in the amplitude of the daily variations as well, reflecting the effect of an increased XR flux during that day [55], which is caused by the solar flares (see Figure 5.46). There were three C flares during the morning of 13th of March, these are seen in Figure 5.45 and may be the reason why Δ TEC and TEC (Figures 5.47 (a) and 5.47 (b)) increased after midday of that day.
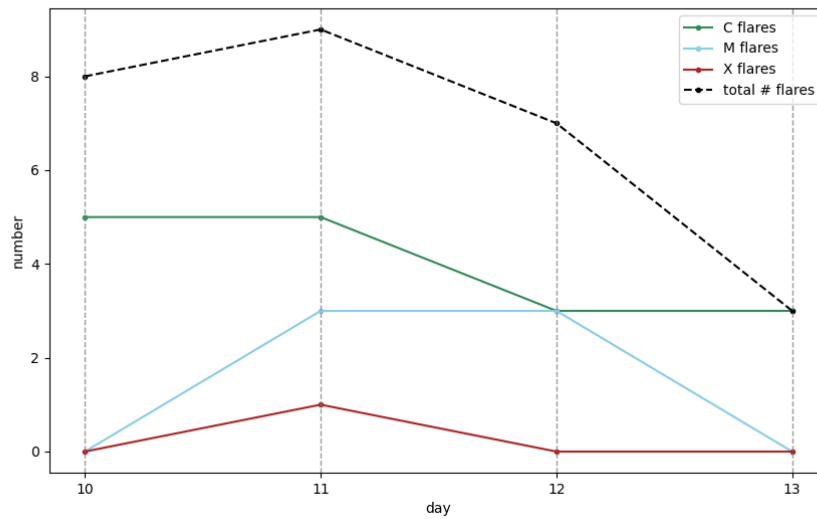
Figure 5.45: Number of flares per day (C,M,X and total) during 10-13th of March 2015.
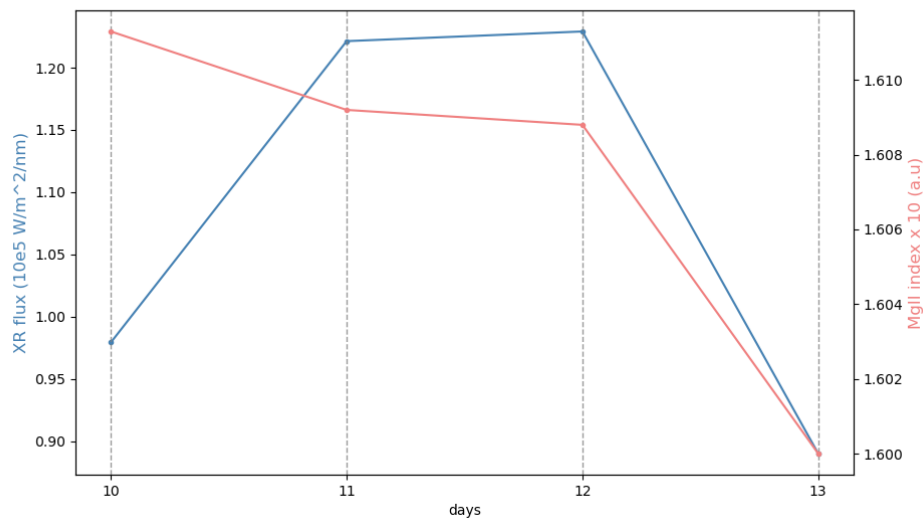
Figure 5.46: UV (MgII) and XR fluxes during 10-13th of March 2015.

(a)   (b)
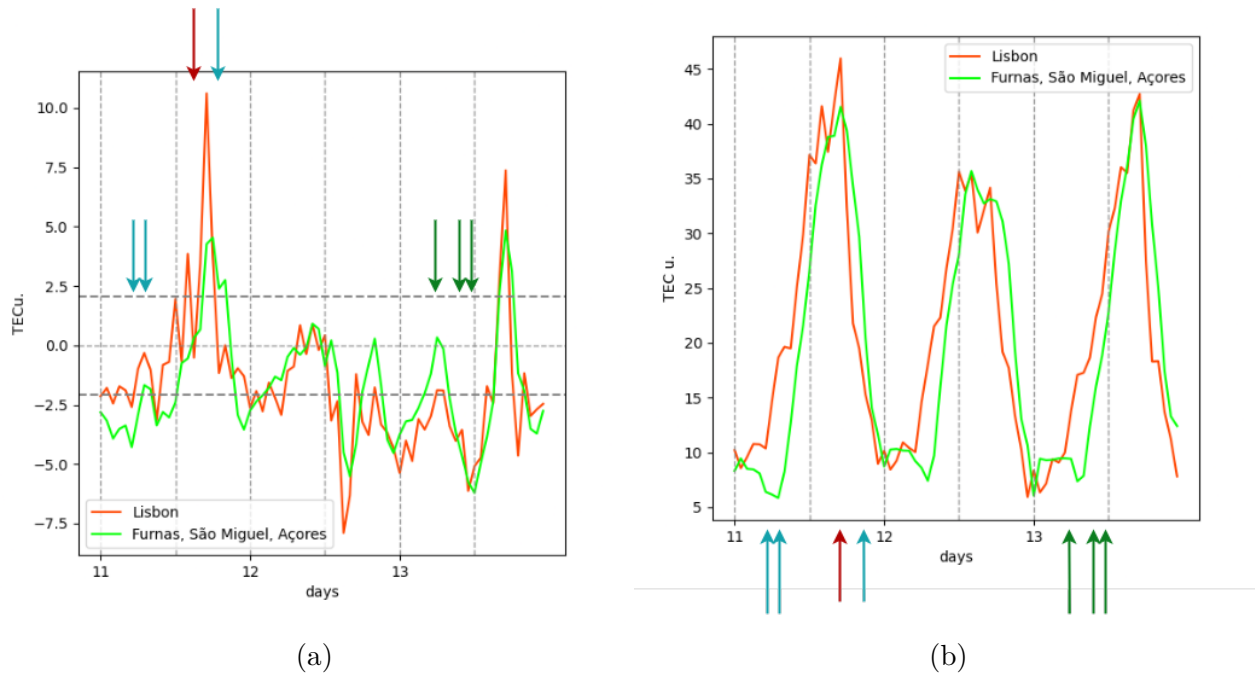
Figure 5.47: ΔTEC (a) and TEC (b) values over the period of 11-13th of March 2015, for Lisbon and the Azores. Red, blue and green arrows correspond to X, M, C flares, respectively.

Solar flares for September 2017

On 4th of September 2017, two M flares occurred (15:30 and 18:00 UTC). One can see, from Figure 5.51, that the XR flux increased to ∼ 0.7 $W/m^2/nm$. On 4th of September, a decrease in ionization followed by an increase occurred. In the late hours of this day, Δ TEC = 7-8 TECu (see Figure 5.48 (a)), as a result of the latest flare at 18:00 UTC. However, this increase in TEC is small, as it is not noticeable on TEC from Figure 5.48 (b).

On 5th of September, another two M flares (at 7:00 UTC and 17:43 UTC) and four C flares (from 10:15 to 17:15 UTC) erupted from the Sun, and the XR flux was at 1 $W/m^2/nm$ (see Figure 5.51). The M flare that occurred at 17:45 UTC had an effect on TEC variation, which is seen as an increase of Δ TEC ∼ 6-7 TECu, in Figure 5.48 (a), around that time. TEC also had a larger maximum (TEC ∼ 20 TECu) during this day than in the previous

days, as it is seen in Figure 5.48 (b).
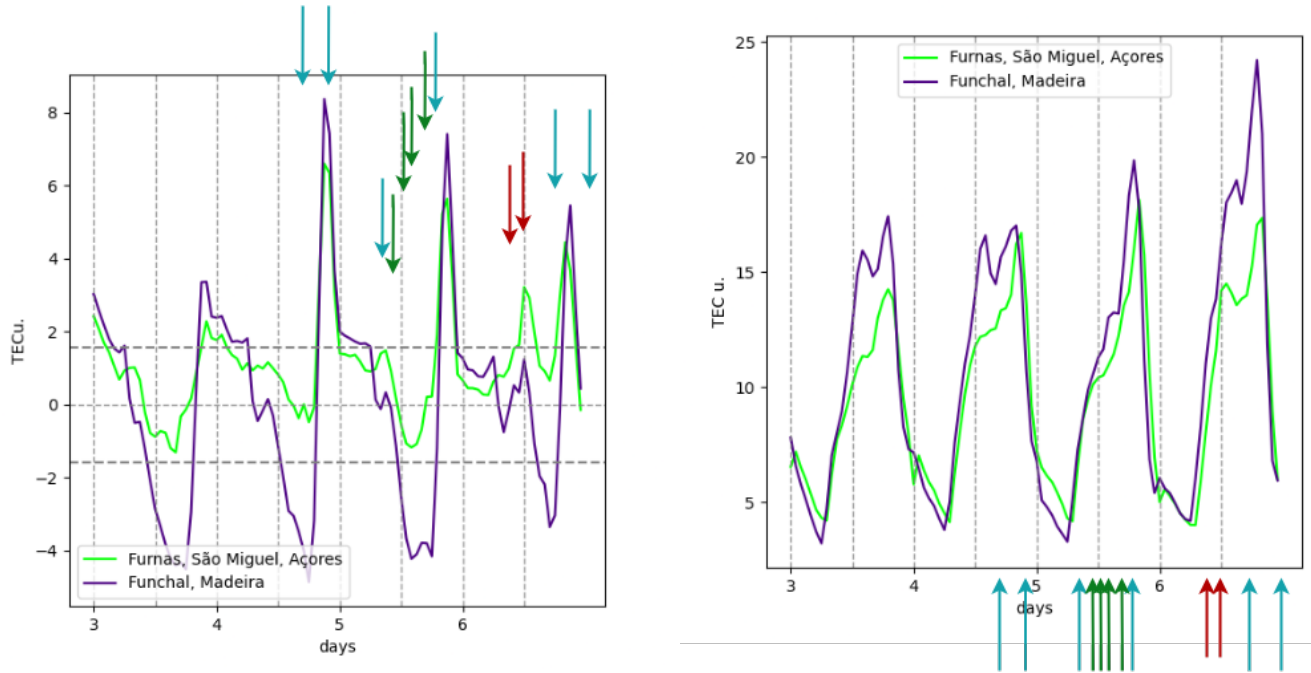
Figure 5.48: Δ TEC (a) and TEC (b) values over the period of 3rd-6th of September 2017, for Madeira and the Azores.

On 6th of September 2017, two X flares (maximum at 9:10 and 12:02 UTC) and two M flares (maximum at 15:56 and 19:30 UTC) were released from the Sun. The X flares affected TEC mostly in the Azores, although the variations are smaller (Δ TEC = 5 TECu, see Figure 5.48 (a)). Although these were stronger flares, the XR flux was not higher than 0.9 $W/m^2/nm$ and UV flux < 1.6 a.u as seen in Figure 5.51. The M flare that occurred at 15:56 UTC seems to have also affected Δ TEC ∼ 5 UTC. The maximum TEC on 6th of September was larger than the previous days, with TEC = 24 TECu in Madeira and TEC = 17 TECu in the Azores (see Figure 5.48 (b)).

On 7th of September, two M flares (maximum at 9:54 and 10:15 UTC) and one X flare (maximum at 14:36 UTC) were also seen. As one can see in Δ TEC from Figure 5.49 (a),

during the 7th of September, ionization increased twice. The two Δ TEC increases, during 12:00 UTC (stronger for the Azores) and 22:00 UTC (stronger for Madeira), were caused by the two M flares that occurred earlier and the X flares that occurred after, respectively. The daily maximum of TEC, seen in Figure 5.49 (b), increased significantly on this day, TEC = 30 TECu for Madeira and TEC = 22 TECu for Azores.

There were observed two M flares (peak at 7:49 and 15:47 UTC) and six C flares (at 9:39, 10:49, 11:27, 12:13, 12:33, and 18:18 UTC) during the entire day time of 8th of September. Flares from the 8th of September were noticed only in Furnas, with Δ TEC = 5 TECu (see Figure 5.49 (a)). However, the daily TEC was high in Madeira during this day, Figure 5.49 (b) shows TEC = 25 TECu, but this can still be due to the increase in TEC in the previous day. From Figure 5.40 of EOF1 for September 2017, from days 6th to 8th there is an increase in the amplitude of the daily variations. Since there is no significant increase in EOF1 for 4th, 5th, 9th, 10th, or 11th of September, this increase (from 6th to 8th) can be due to the geomagnetic storm that occurred on 7th of September.

One M flare (maximum at 11:04 UTC) was spotted on 9th of September. There is no increase of Δ TEC or TEC seen in Figures 5.49 (a) or 5.49 (b). Therefore, it is presumed that this flares had no significant effect on the ionospheric ionization.

An X flare (peak at 16:06 UTC) was seen on 10th of September. On this day, the XR flux increased to 1 a.u (see Figure 5.51). From Figure 5.49 (a), one can see that, after the time of the flare, there is an increase in Δ TEC = 5 TEC in Madeira. The Δ TEC, Figure 5.49 (a) shows a decrease that might not have been caused by the flares but is from other features such as regular post-sunset decreases during days 8th, 9th, 10th, and 11th of September, since all of them occurred after $\sim$ 18:00 UTC and were more noticeable on Madeira. During 7th, 8th, and 10th of September, there was a decrease in XR flux, and the UV flux started to decrease from day 7th, as seen in Figure 5.51.
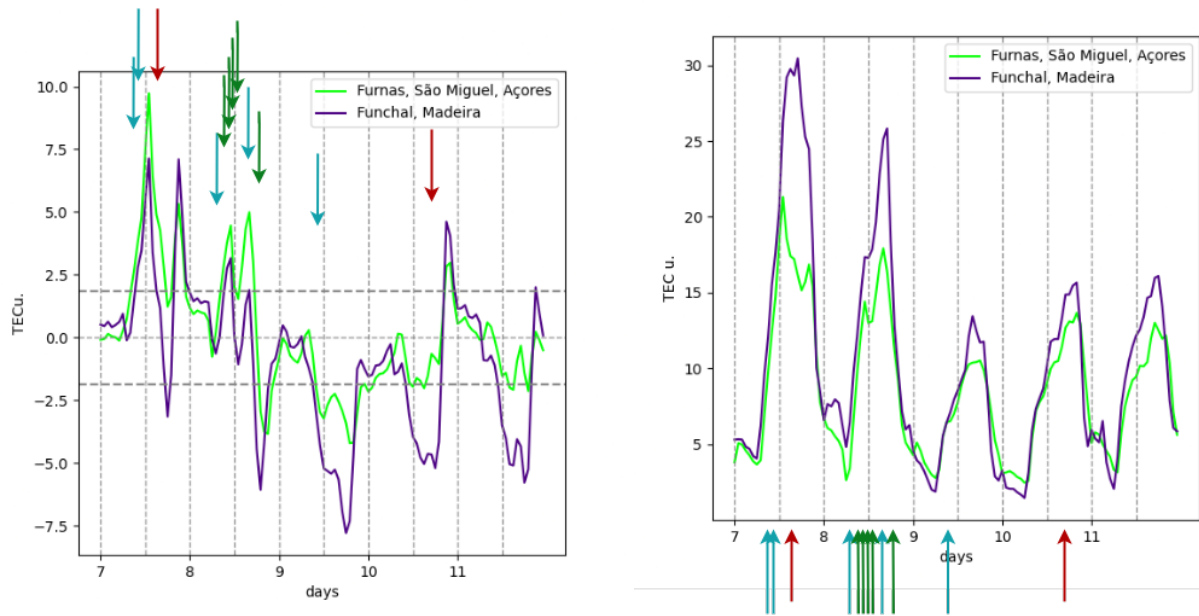
Figure 5.49: Δ TEC (a) TEC (b) values over the period of 7-11th September 2017, for Madeira and the Azores.
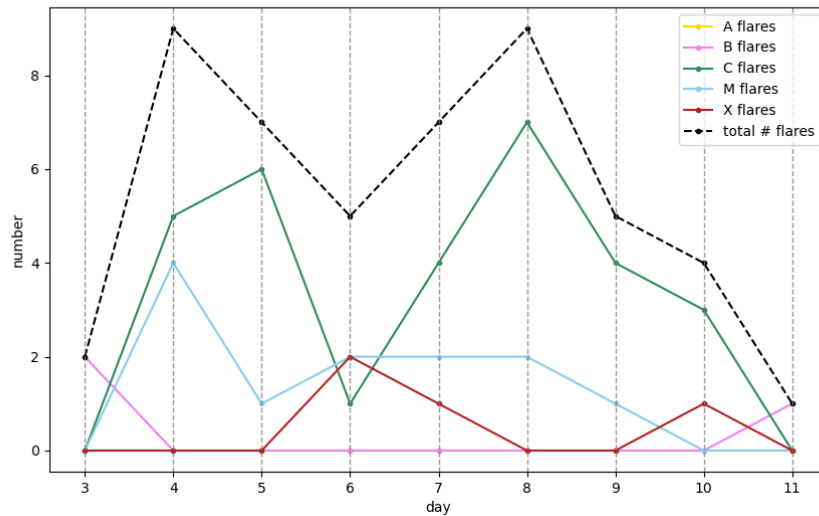
Figure 5.50: Number of flares per day (C,M,X and total) during 3rd-11th of September 2017.
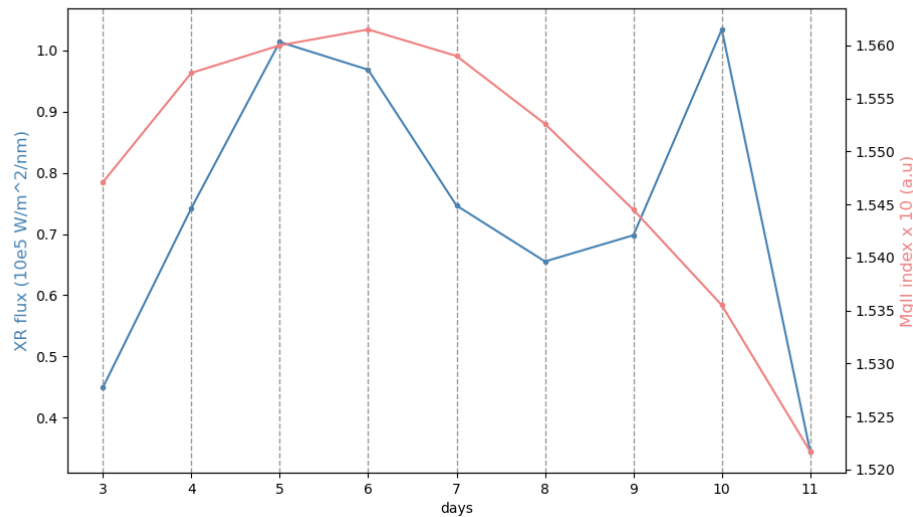
Figure 5.51: UV (MgII) and XR fluxes during 3rd-11th of September 2017.

To sum up, there were twenty-four flares registered during day time between 3rd and 11th of September 2017; four of these were X-flares, and eleven were M-flares. Their distribution throughout the days is seen in Figure 5.50. Table 5.1 summarizes the flare occurrence for September 2017, including peak time, type, and total number of flares.

During the days when M, X, or more than 5 C solar flares were registered (see Figures 5.45 and 5.50), the variations of 1h TEC data were analysed, and in some cases, the effect of the flares was seen, although, for a few flares, signatures were not prominent. A noticeable effect on the 1h TEC variation due to a flare might depend on the flare type, peak (or start) time, and duration. Weaker (C-flares) do not affect daily TEC variations as much as M or X flares. Furthermore, the TEC changes were consistent across the analysed locations but were particularly pronounced at Lisbon in March of 2015 and at Madeira in September of 2017. Other effects were also seen in these events, such as the post-sunset decreases in TEC.

A detailed analysis of conditions necessary for a flare to have a significant effect on TEC

is out of the framework of this work. However, it is possible to make some conclusions: first, Δ TEC is the best of the three parameters, to study the solar flares' effect as one can see an increase in the ionization with this parameter. Parameters like the daily mean TEC or EOF1 are not suitable to study flares' effects. The increases in EOF1 (see Figure 5.8 and 5.40) are driven mainly by changes in the UV and XR fluxes (see Figures 5.46 and 5.51). Secondly, a time resolution of, for example, 5-15 minute data would allow a better study of the solar flares since their duration is usually short (less than 30 minutes).

Table 5.1: Flare (X,M and C) occurrence during 3rd-11th of September 2017

Day	Flare type	Peak time (UTC)	# C flares	# M flares	# X flares	Flares # total
4	M	15:30	-	2	-	2
4	M	18:00	-	2	-	2
5	M	7:00	4	2	-	6
5	C	10:15	4	2	-	6
5	C	12:34	4	2	-	6
5	C	16:19	4	2	-	6
5	C	17:15	4	2	-	6
5	M	17:43	4	2	-	6
6	X	9:10	-	2	2	4
6	X	12:02	-	2	2	4
6	M	15:56	-	2	2	4
6	M	19:30	-	2	2	4
7	M	9:54	-	2	1	3
7	M	10:15	-	2	1	3
7	X	14:36	-	2	1	3
8	M	7:49	6	2	-	8
8	C	9:39	6	2	-	8
8	C	10:49	6	2	-	8
8	C	11:27	6	2	-	8
8	C	12:13	6	2	-	8
8	C	12:33	6	2	-	8
8	C	15:47	6	2	-	8
8	M	18:18	-	2	1	3
9	M	11:04	-	1	-	1
10	X	16:06	-	-	1	1

Modeling of TEC at Portugal during quiet and disturbed periods

6

6.1 Ionospheric models

In order to better understand the ionosphere, different types of models are developed. Ionospheric models can be used not only to test and improve our understanding of the physical processes in the ionosphere. Such models can also be used to forecast conditions potentially dangerous for, for example, the proper functioning of navigation and communication services. The models are tested by comparing their forecasts with observations or forecasts made by reference models. There are three different types of models: physics-based models (use equations describing physical processes), empirical models (based on experimental data), and semi-empirical models (use both physical equations and experimental data). Models can also be global (mapping worldwide ionospheric conditions) or local (specific to a region).

Two models that can forecast TEC for a particular region and a given time interval were used. One of these models is **IRI** (International Reference Ionosphere) [56, 57]. It is built using observational data (for example, ionosonde, topside sounder, and GNSS data) that are fitted to mathematical expressions (such as the Chapman layer equation). The input parameters for the IRI model are the latitude and longitude of the studied region and height (0-1000 km, top to bottom). The output is TEC in TECu [58]. IRI16 is a reliable and stable model available online [59].

The **PCA-NN** model forecasts TEC using neural networks (NN) and PCA. TEC data

used to train this model are the same as those used in this work. This model was developed during the PRIME project. It uses a set of predictors - space weather parameters, like Dst, ap, and AE geomagnetic indices, proxies of the solar UV and XR fluxes, and the number of solar flares per day. The full description of the model can be found in [60]. The PCA-NN model execution consists of three stages. At the first stage, the TEC data with 1h time resolution observed for the previous 31 days are decomposed using PCA; then NN models the daily mean TEC, EOF1, and EOF2 (all parameters with 1-day time resolution) are built using space weather predictors. Once trained, the NN can forecast the daily mean TEC, EOF1, and EOF2 values for the following day, which are later used to make a forecast of TEC for that day with 1h time resolution.

6.2 Comparison between observed and modeled TEC

Figures 6.1 - 6.14 show TEC observed (in black line) and modeled (dashed blue and pink lines) during geomagnetic storms of March, June, October, and December of 2015, and May and September of 2017 for Lisbon (Figures 6.1 - 6.6), Funchal (Figures 6.7 - 6.10) and Furnas (Figures 6.7 - 6.14).
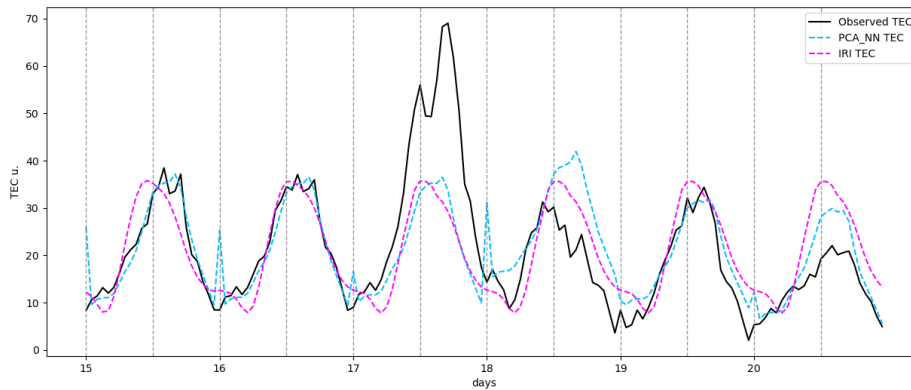
Figure 6.1: Observed (black full line), modeled with IRI (pink dashed line) and with PCA-NN (blue dashed line) series of daily TEC over the period of 15-20th of March 2015 in Lisbon.
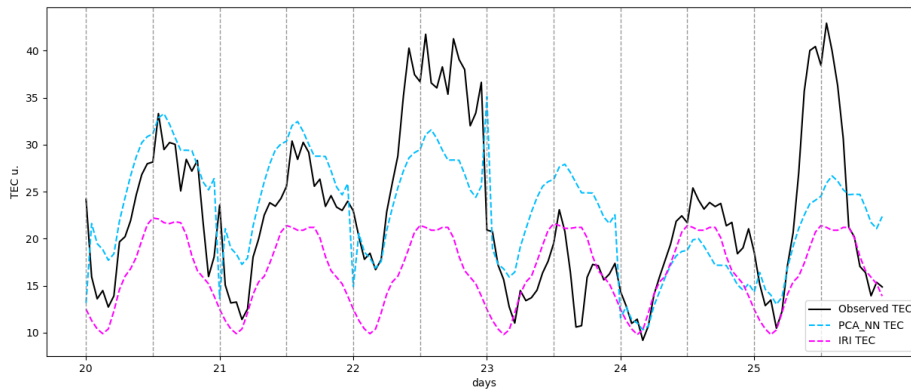
Figure 6.2: Same as Figure 6.1 but for the period of 20-26th of June 2015 in Lisbon.

Figures 6.1 - 6.6 show TEC variations during six storms (17-18th of March, 22nd-23rd of June, 7th of October, and 20th of December of 2015, and 28th of May and 8th of September of 2017) that are modeled and compared with observations for Lisbon. Both models give a similar forecast and fit with the observed data for quiet days of March and June 2015, and May 2017, as one can see in Figures 6.1, 6.4 and 6.5. On the days of a storm, in these examples, the observed TEC increases, but the models forecast another apparently quiet day,

still, for May 2017 (Figure 6.5) TEC modeled by PCA-NN is closer to the observed values than TEC modeled by IRI.
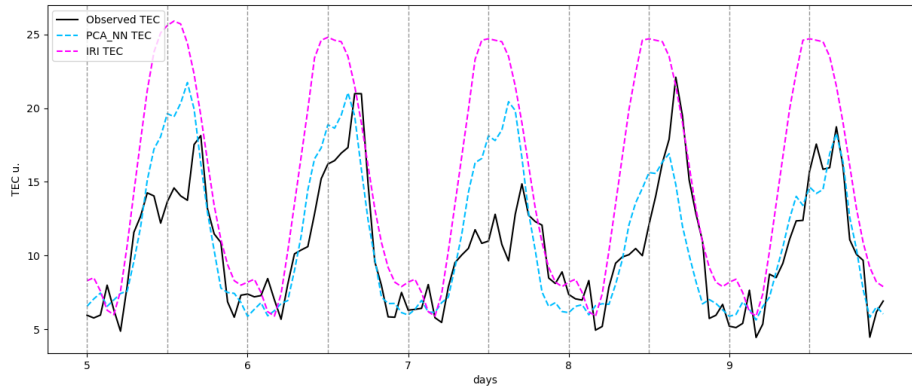
Figure 6.3: Same as Figure 6.1 but for the period of 5-9th of October 2015 in Lisbon.
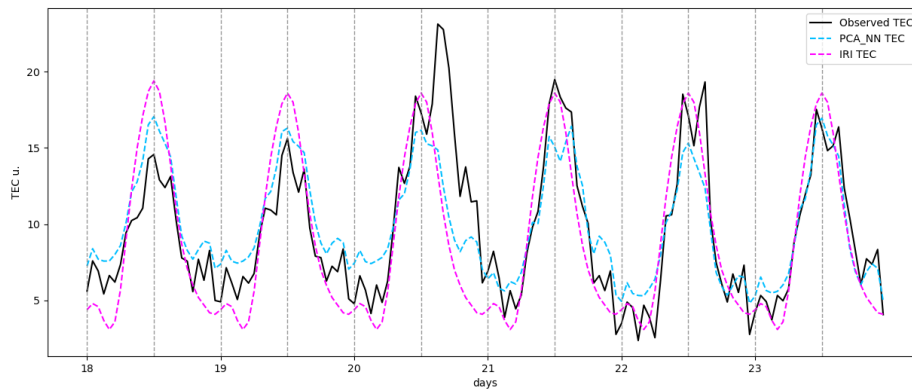
Figure 6.4: Same as Figure 6.1 but for the period of 18th-23rd of December 2015 in Lisbon.

The two models presented slightly different TEC values from the observed TEC in some days of June and October of 2017 and May 2017 (as it can be seen in Figures 6.2, 6.3 and 6.6 respectively). Both models also forecast different TEC values during these time intervals: on June 2015 and September 2017 TEC (Figures 6.2 and 6.6) values are higher for PCA-NN model, for October 2015 (Figure 6.3), it is IRI that has the most significant TEC

values. Storm days 7-8th of September 2017 are well modeled by PCA-NN, the increase of the modeled TEC values is clearly seen in Figure 6.6 for this day.
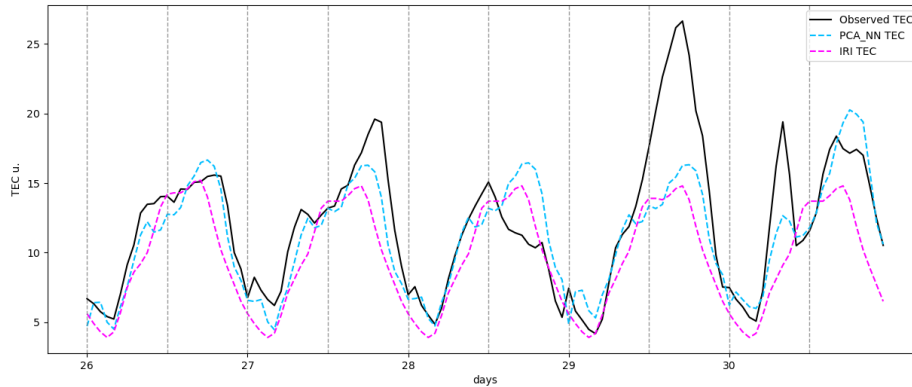
Figure 6.5: Same as Figure 6.1 but for the period of 26-30th of May 2017 in Lisbon.
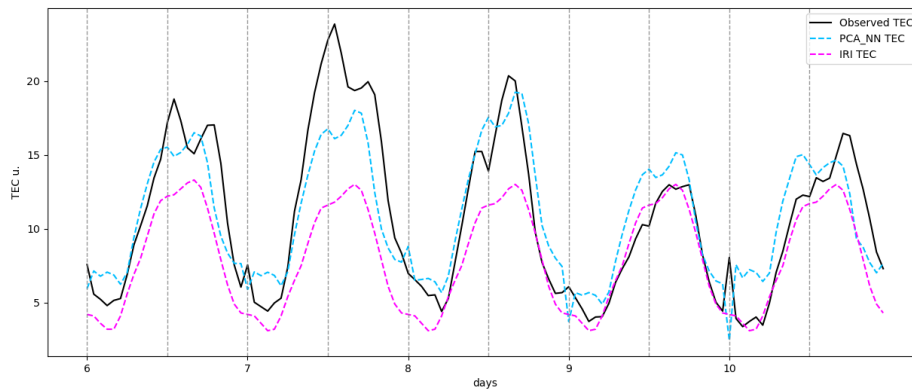
Figure 6.6: Same as Figure 6.1 but for the period of 6-10th of September 2017 in Lisbon.

Four geomagnetic disturbed periods (17-18th of March and 22nd-23rd of June 2015, and 28th of May and 8th of September 2017) were modeled for Funchal (Madeira) (Figures 6.7 to 6.10), and Furnas (Azores) (Figures, 6.11 to 6.14) using IRI and PCA-NN.

The forecasted TEC values are similar between IRI and PCA-NN in Funchal for the four analysed time intervals, Figures 6.7 to 6.10. Modeled TEC values fit with the observed data

on the quiet days.
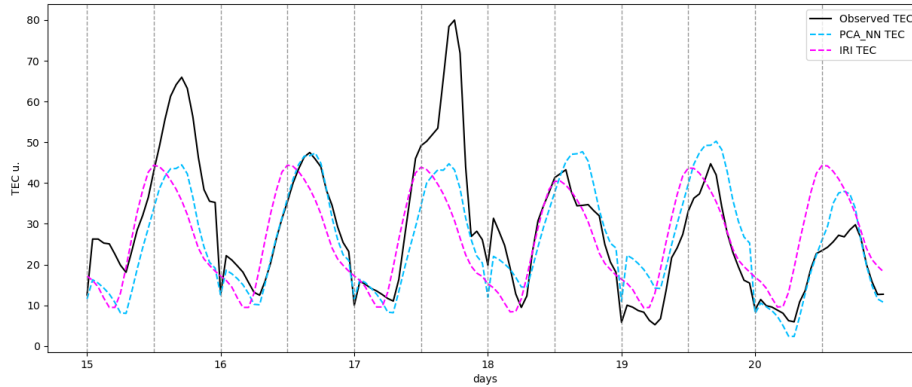
Figure 6.7: Same as Figure 6.1 but for the period of 15-20th of March 2015 in Funchal.
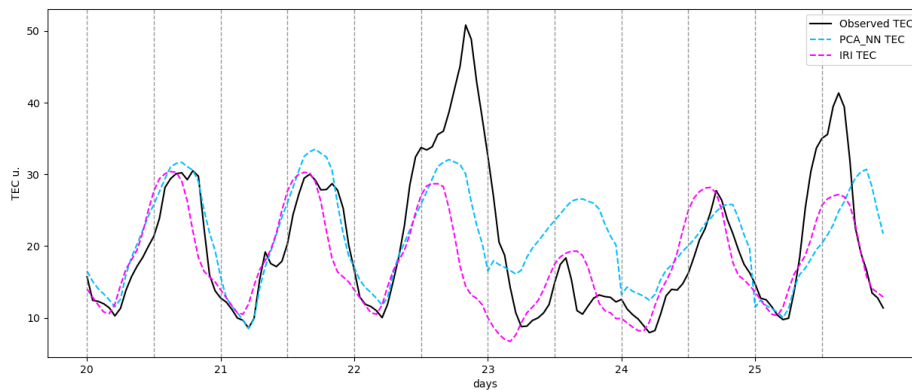
Figure 6.8: Same as Figure 6.1 but for the period of 20-25th of June 2015 in Funchal.

The IRI model forecasts the TEC values of the second storm day of June 2015, the 23rd, better than PCA-NN (see Figure 6.8). The observed TEC decreased on this day, and IRI values are very close to the data series. However, for the first day of the storm, 22nd of June, both models forecast TEC variations similar to those of a quiet day.

The TEC variations during the period of 26th to 30th of May 2017, are initially better modeled by PCA-NN (days 26th and 27th), as one can see in Figure 6.9. After the storm,

on 29th of May, TEC values are better forecasted by IRI.
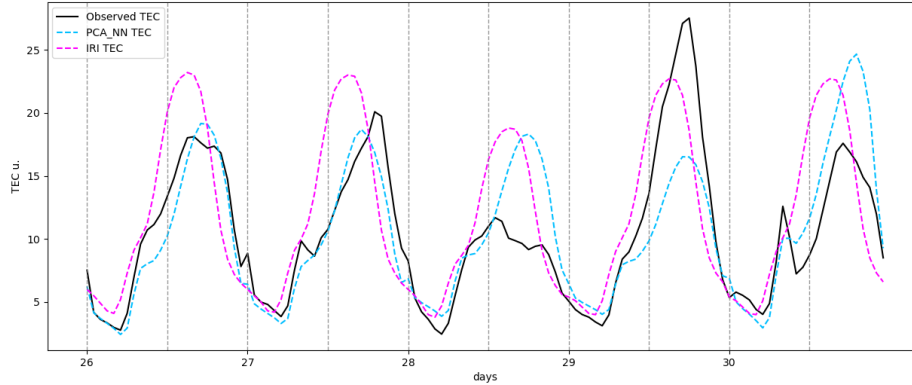
Figure 6.9: Same as Figure 6.1 but for the period of 26-30th of May 2017 in Funchal.
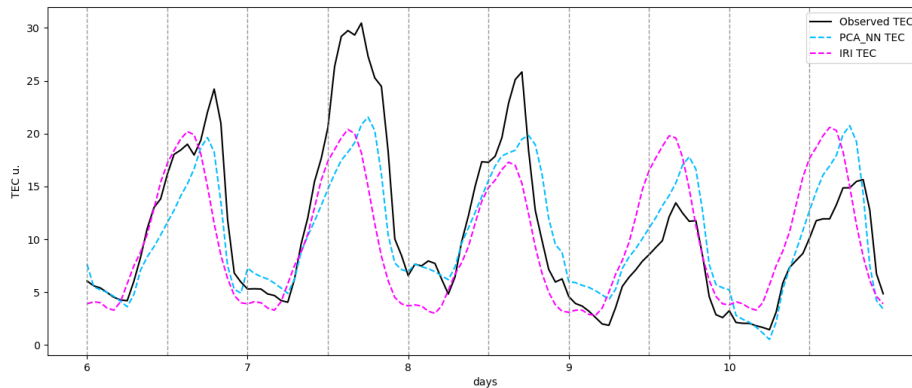
Figure 6.10: Same as Figure 6.1 but for the period of 6-10th of September 2017 in Funchal.

For Furnas, TEC modeled by the two ionospheric models is coherent with the quiet day TEC variations of the observed series, as one can see from Figures 6.11 to 6.14. The decrease in TEC of 18th of March 2015 is better forecasted by PCA-NN, Figure 6.11.

For the storm in June 2015, PCA-NN forecasted TEC values are close to the observed ones at the beginning (days 20th-21st). After the storm, from days 23rd to 25th of June, the IRI model TEC values predict the observed TEC slightly better, as seen from Figure 6.12.
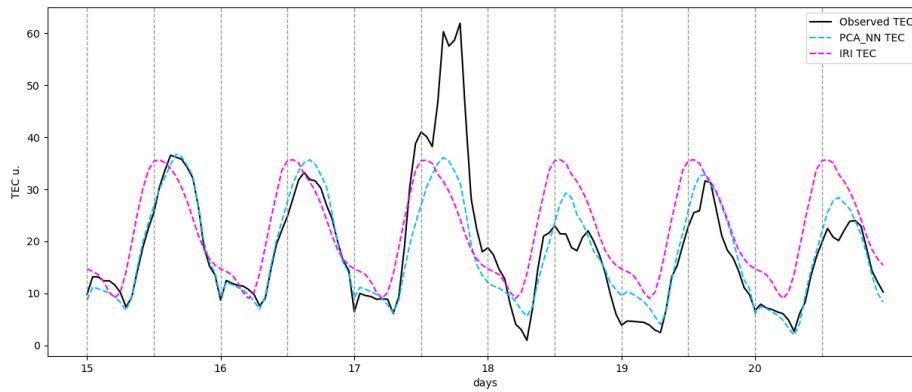
Figure 6.11: Same as Figure 6.1 but for the period of 15-20th of March 2015 in Furnas.
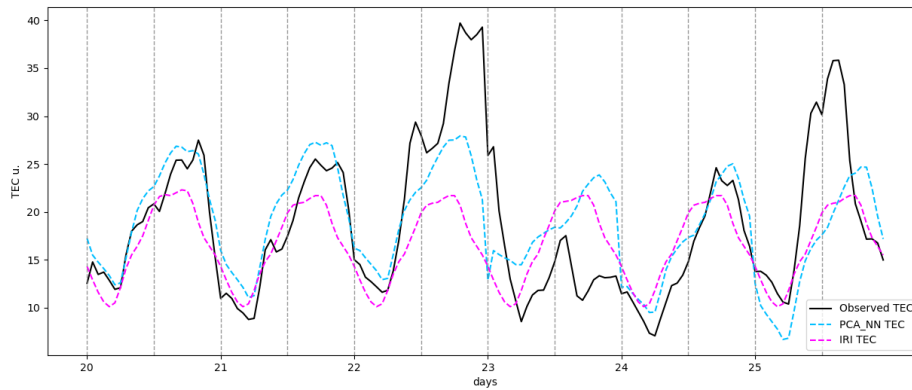
Figure 6.12: Same as Figure 6.1 but for the period of 20-26th of June 2015 in Furnas.

During May and September 2017, the modeled (IRI and PC-NN) and observed TEC variations are very similar, except for the few hours of the day of the storm (29th of May and 7th of September, Figures 6.13 and 6.14, respectively) when the observed TEC reaches its maximum.

105
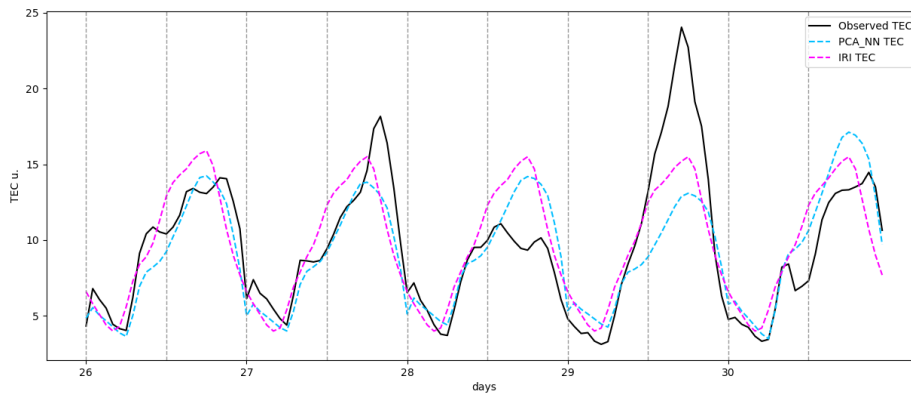
Figure 6.13: Same as Figure 6.1 but for the period of 26-30th of May 2017 in Furnas.
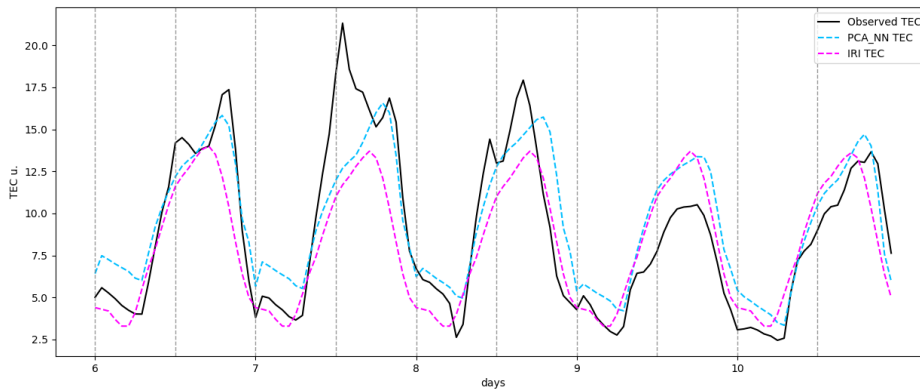
Figure 6.14: Same as Figure 6.1 but for the period of 6-10th of September 2017 in Furnas.

It is clear that quiet days (usually the first two days shown in Figures 6.1 - 6.14) are accurately simulated by both models. One can see that the IRI model (in pink) usually follows a quiet day variation, not changing too much from day to day, while the PCA-NN model is trained to use space weather conditions to forecast TEC. Thus, disturbed days are generally better described by the PCA-NN model than by IRI.

To quantify the predictive power of the models, the root mean square error (RMSE), equation 6.1, was calculated using the observations ($TECo$) and each of the models' forecasts

$(TECm)$, and where n is the length of the compared series:

$$RMSE = \sqrt{\frac{1}{n}\sum_{i=1}^{n}(TECo_i - TECm_i)^2} \tag{6.1}$$

The results are presented in tables 6.1, 6.2 and 6.3, for Lisbon, Funchal and Furnas, respectively.

The performance of both models is similar between the different locations, showing adaptation to the latitude changes for both models. From Tables 6.1 - 6.3, one can see that the predictive power of the model PCA-NN is better (RMSE (IRI) > RMSE (PCA-NN)) for all of the analysed cases and all studied locations. For four storms (in March and June of 2015 and May and September of 2017), it is possible to compare the performance of the models for different locations. As one can see from Tables 6.1 - 6.3, the best forecasts (lowest RMSE values) by both models were made for Furnas, and the worst forecasts (highest RMSE values) were made for Funchal.

Table 6.1: RMSE in TECu of the analysed periods for Lisbon

month, year	RMSE (IRI)	RMSE (PCA-NN)
3, 2015	9.379	9.069
6, 2015	8.964	6.569
10, 2015	6.187	2.987
12, 2015	3.125	2.410
5, 2017	3.863	2.941
9, 2017	3.971	2.635

Table 6.2: RMSE in TECu of the analysed periods for Funchal

month, year	RMSE (IRI)	RMSE (PCA-NN)
3, 2015	12.413	9.788
6, 2015	8.229	7.447
5, 2017	4.628	3.532
9, 2017	5.189	3.834

Table 6.3: RMSE in TECu of the analysed periods for Furnas

month, year	RMSE (IRI)	RMSE (PCA-NN)
3, 2015	9.442	5.939
6, 2015	6.641	5.795
5, 2017	2.648	2.761
9, 2017	2.696	2.301

Tables 6.4 - 6.6 show the RMSE for the quiet days (DQ RMSE), prior to and after the storm, and for the storm days (SD RMSE), for both models. From these tables, both models perform better during the quiet days, QD RMSE < SD RMSE in all cases. In general, for both models, the RMSE values calculated taking into account only quiet days are smaller than the RMSE values calculated for the whole studied intervals (compare Tables 6.4 - 6.6 with Tables 6.1 - 6.3). However, even for the storm days, RMSE is low and smaller for PCA-NN than for IRI, except for storms in March 2015 for Lisbon and in May 2017 for Funchal and Furnas, when IRI performed better.

Table 6.4: RMSE in TECu for the quiet days and storm days of the analysed periods for Lisbon

month, year	QD RMSE (IRI)	SD RMSE (IRI)	QD RMSE (PCA-NN)	SD RMSE (PCA-NN)
3, 2015	6.287	13.596	4.207	14.537
6, 2015	7.320	11.571	5.819	7.858
10, 2015	5.850	7.385	2.606	4.176
12, 2015	2.521	5.427	2.000	4.219
5, 2017	3.186	5.830	2.128	5.015
9, 2017	2.859	6.792	2.306	3.666

Table 6.5: RMSE in TECu for the quiet days and storm days of the analysed periods for Funchal

month, year	QD RMSE (IRI)	SD RMSE (IRI)	QD RMSE (PCA-NN)	SD RMSE (PCA-NN)
3, 2015	11.397	14.229	8.781	11.542
6, 2015	4.999	12.376	5.722	10.029
5, 2017	4.737	4.162	3.096	4.9047
9, 2017	4.466	7.408	3.086	5.950

Table 6.6: RMSE in TECu for the quiet days and storm days of the analysed periods for Furnas

month, year	QD RMSE (IRI)	SD RMSE (IRI)	QD RMSE (PCA-NN)	SD RMSE (PCA-NN)
3, 2015	7.681	12.226	2.571	9.622
6, 2015	4.719	9.368	4.821	7.366
5, 2017	2.398	3.471	1.938	4.802
9, 2017	2.182	4.159	2.058	3.088

The PCA-NN model is very recent, and it has been validated for middle latitudes ($\sim 40° - 50°$ N). For southern regions, there are still structures that need to be considered (EEJ and plasma bubbles) to improve the model's performance [60]. While the RMSE obtained in this part of the work are not very small, the overall performance of the PCA-NN model is in line with other current TEC models, such as IRI, and it was able to outperform it in some cases.

Conclusion and Outlook 7

In this work, the variations of the ionospheric TEC in the regions of Portugal's mainland and its insular territories were studied during space weather quiet and disturbed conditions (geomagnetic storms and solar flares). Afterwards, the observational data were compared with simulations made by a state-of-the-art ionospheric model (IRI), and a new model (PCA-NN) developed at IA-U.Coimbra group in the frame of the PRIME project.

The daily quiet TEC variations obtained by two methods, QDA and PCA, were compared. They exhibit similar patterns across all locations and months investigated. Discrepancies between TEC_{PC} and TEC_{QD} are negligible when compared to the uncertainties of TEC_{QD}. Thus, it is proven that the PCA method is a useful tool for obtaining the daily TEC variations. The analysis of the daily TEC variations shows that for the studied region, the daily TEC is lowest during nighttime due to a lack of sunlight. TEC increases as the sun rises and reaches its highest point around solar midday. Also, the amplitude and the shape of the daily variations of TEC depend on the time of sunrise/sunset and insolation throughout the year.

To study TEC variations during geomagnetic storms, eleven storm events were analysed throughout 2015-2018 (descent of the 24th solar cycle) using three TEC parameters: Δ TEC for the differences between current TEC and quiet TEC, the daily mean TEC to show the daily mean of TEC during the month with a disturbance and EOF1 representing the amplitudes of the daily variations. The results show that in most cases, TEC variations were synchronous between Lisbon, Azores and Madeira regions. The southern region of Madeira usually has higher TEC values due to its equatorial location, therefore, disturbed TEC is higher. Positive or positive-negative ionospheric storms (increase of TEC during only the first

day of the storm or increase of TEC during the first day of the storm and decrease during the second day, respectively) were most common (eight out of the eleven). The storms in September 2017 and August 2018 can be more precisely classified as positive-positive-negative and positive/negative/positive, respectively. A negative-positive ionospheric storm (with a decrease of TEC during the first day of the storm and an increase during the second day, respectively) was observed in May 2017, and it was caused by a geomagnetic storm that started, contrary to all other studied geomagnetic storms, during the local night time. A negative ionospheric storm occurred in October 2015, caused by a geomagnetic storm that took place during an already geomagnetically disturbed background.

The analysis of TEC variability on days with M, X and C solar flares was done to study the ionospheric response to solar flares during geomagnetically quiet days. The effects of solar flares in 1h TEC data are not always present, but it can be seen as an increase of Δ TEC. The TEC perturbations were synchronous through the locations studied but were stronger in Lisbon for March 2015 and in Madeira for September 2017. Due to the brief duration of solar flares, a better time resolution of TEC data would be needed to accurately study how TEC varies depending on the type of flare, flare start time, and duration.

Finally, the modelling of TEC variations during six time intervals around a geomagnetic storm for Lisbon and four for Furnas and Funchal showed that the quiet days are well simulated by both models. For the geomagnetically disturbed periods, the PCA-NN model gives better forecasts than the IRI model. There are at least, two reasons for the better performance of the PCA-NN model. First, IRI models are mostly climatological models, while PCA-NN is made using data from the quiet and disturbed periods. Also, the PCA-NN model is trained on the local data and, therefore, can better represent local TEC variability, both during the quiet and disturbed days.

To sum up, the understanding of TEC variations over the Portuguese region was explored

in this work. Furthermore, the study on the forecasting of TEC during SW events may contribute to the reliability of the GNSS-based services in the studied areas.

As a future work, improving the time and spatial resolution of the TEC series would be useful to allow the analysis of spatial differences in detail and short-duration events like the solar flares. Also, longer time series would be necessary to study seasonal and solar activity cycle-influenced TEC variations. Longer time data series are needed to do a detailed study of the different types of geomagnetic storms. This would help distinguish a statistically significant difference in the TEC response to storms of different strength, local commencement time, origin (CME vs coronal holes), and other parameters.

APPENDIX

<div style="text-align: right; font-size: 3em;">A</div>

Plasma criteria

Magnetic moment: Considering it takes 1 gyro-period $\Omega^{-1} = \frac{m}{qB}$ for a particle to complete 1 orbit of area $A = 2\pi r_L$, the current generated in this loop is going to be $I = -\frac{|q|\Omega}{2\pi}$. The magnetic moment $\mu = IA$ is

$$\mu = \frac{1}{2}\frac{|q|v_\perp^2}{\Omega} = \frac{1}{2}|q|r_L v_\perp \tag{A.1}$$

The Debye shielding: Considering a three-dimensional gas, with $f\ d^3(u, v, w)$ particles per m^3 where f is the Maxwell-Boltzmann distribution function:

$$f(u, v, w) = n\left(\frac{m}{2\pi k_B T}\right)^{3/2} e^{-\frac{m(u^2+v^2+w^2)}{2k_B T}} \tag{A.2}$$

$k_B = 1.380649 \times 10^{-23}\, J/K$ and T is the temperature

Adding an electric potential ϕ associated with a charge q one defines the density of the particles to be n_∞ where $\phi(\infty) = 0$. Integrating f over the velocity vector gives the density of species $n_s = n_\infty \exp\left(q\phi/k_B T\right)$

Assuming $T_e = T_i = T$ and $n = n_\infty$ the quantity λ is defined as the Debye length:

$$\lambda_D = \left(\frac{\varepsilon_0 k_B T}{ne^2}\right)^{1/2} \tag{A.3}$$

from this length forward, particles are shielded from an electric field created by another particle. For the ensemble of charged particles to behave like plasma, it must be dense

enough so that the dimension of the system L $\gg \lambda_D$.

The number of particles in a sphere with radius $r = \lambda_D$ is

$$N_D = n\frac{4}{3}\pi\lambda_D^3 = n\frac{4}{3}\pi\left(\frac{\varepsilon_0 k_B T}{ne^2}\right)^{3/2} \tag{A.4}$$

There must be enough particles in the sphere for Debye shielding to be valid, $N_D \gg 1$ [2].

Most plasma will remain free from strong electric fields: it is "quasi-neutral": $n_i \approx n_e \approx n$ [5].

Plasma Oscillation: Taking the time rate of change of a current density in this plasma of one specie of ion n_i and electrons n_e, $\mathbf{j} = e(n_i\mathbf{u}_i - n_e\mathbf{u}_e)$ and applying the divergence, one gets:

$$\frac{\partial^2}{\partial t^2}\rho_q = -\left(\frac{n_i}{m_i}e^2 + \frac{n_e}{m_e}e^2\right)\frac{\rho_q}{\varepsilon_0} = -(\omega_{pi}^2 + \omega_{pe}^2)\rho_q \tag{A.5}$$

Plasma oscillates at a specific frequency $\omega_p^2 = \omega_{pi}^2 + \omega_{pe}^2$. Since $m_i >> m_e$, $\omega_p \approx \omega_{pe}$, and the plasma particles behave in unison, too many collisions between these particles will damp the collective oscillation, so for a mean time τ between them, plasma requires $\omega_p\tau > 1$ [2, 5].

Macroscopic variables for plasmas

$$\mathbf{J} = \int q\mathbf{v}f(\mathbf{r}, \mathbf{v}, t), d\mathbf{v} \qquad \text{(Current density)} \qquad \text{(A.6)}$$

$$n(\mathbf{r}, t) = \int f(\mathbf{r}, \mathbf{v}, t), d\mathbf{v} \qquad \text{(Number density)} \qquad \text{(A.7)}$$

$$\mathbf{u}(\mathbf{r}, t) = \frac{1}{n} \int \mathbf{v}f(\mathbf{r}, \mathbf{v}, t), d\mathbf{v} \qquad \text{(Fluid velocity)} \qquad \text{(A.8)}$$

$$T = \frac{m}{3nk_B} \int |\mathbf{v} - \mathbf{u}|^2 f(\mathbf{r}, \mathbf{v}, t), d\mathbf{v} \qquad \text{(Temperature)} \qquad \text{(A.9)}$$

$$K = \frac{m}{2n(\mathbf{r}, t)} \int |\mathbf{v} - \mathbf{u}|^2 f(\mathbf{r}, \mathbf{v}, t), d\mathbf{v} \qquad \text{(Average random kinetic energy)} \qquad \text{(A.10)}$$

$$P_{ij} = \int m(v_i - u_i)(v_j - u_j)f(\mathbf{r}, \mathbf{v}, t), d\mathbf{v} \qquad \text{(Pressure tensor)} \qquad \text{(A.11)}$$

Magnetohydrodynamics equations

$$\frac{\partial \rho}{\partial t} + \nabla \cdot (\rho\mathbf{v}) = 0 \qquad \text{(Continuity Equation)} \qquad \text{(A.12)}$$

$$\rho \left(\frac{\partial \mathbf{v}}{\partial t} + \mathbf{v} \cdot \nabla\mathbf{v} \right) = -\nabla p + \frac{1}{\mu_0}(\nabla \times \mathbf{B}) \times \mathbf{B} \qquad \text{(Momentum Equation)} \qquad \text{(A.13)}$$

$$\rho \left(\frac{\partial e}{\partial t} + \mathbf{v} \cdot \nabla e \right) = -p\nabla \cdot \mathbf{v} + \mathbf{v} \cdot (\nabla \times \mathbf{B}) \times \mathbf{B} \qquad \text{(Conservation of Energy)} \qquad \text{(A.14)}$$

$$\frac{\partial \mathbf{B}}{\partial t} = \nabla \times (\mathbf{v} \times \mathbf{B}) \qquad \text{(Magnetic Induction Equation)} \qquad \text{(A.15)}$$

Appendix

<div style="text-align: right; font-size: 3em;">B</div>

Table B.1: The first 3 λ_i for PCA from Lisbon's (1.1) data set.

month, year	λ_1	λ_2	λ_3
11, 2014	0.988	0.005	0.0
12, 2014	0.965	0.012	0.006
1, 2015	0.929	0.031	0.017
2, 2015	0.947	0.027	0.01
3, 2015	0.936	0.024	0.016
4, 2015	0.942	0.028	0.008
5, 2015	0.896	0.037	0.028
6, 2015	0.837	0.066	0.031
7, 2015	0.84	0.05	0.037
8, 2015	0.867	0.073	0.016
9, 2015	0.891	0.05	0.028
10, 2015	0.93	0.032	0.018
11, 2015	0.943	0.021	0.019
12, 2015	0.881	0.051	0.031
1, 2016	0.834	0.073	0.03
2, 2016	0.894	0.049	0.018
3, 2016	0.88	0.046	0.027
4, 2016	0.905	0.044	0.018
5, 2016	0.909	0.039	0.019
6, 2016	0.903	0.035	0.025
7, 2016	0.91	0.038	0.017
8, 2016	0.906	0.043	0.022
9, 2016	0.899	0.045	0.019
10, 2016	0.879	0.074	0.02
11, 2016	0.857	0.073	0.028

Table B.2: (continuation) The first 3 λ_i for PCA from Lisbon's (1.1) data set.

month, year	λ_1	λ_2	λ_3
1, 2017	0.999	0.088	0.044
2, 2017	0.829	0.117	0.045
3, 2017	0.779	0.083	0.035
4, 2017	0.836	0.044	0.027
6, 2017	0.893	0.0	0.015
7, 2017	0.999	0.043	0.02
8, 2017	0.908	0.047	0.014
10, 2017	0.895	0.027	0.022
11, 2017	0.944	0.072	0.057
1, 2018	0.869	0.07	0.022
2, 2018	0.807	0.046	0.049
3, 2018	0.999	0.061	0.028
4, 2018	0.891	0.133	0.019
5, 2018	0.866	0.04	0.034
6, 2018	0.783	0.046	0.028
8, 2018	0.893	0.043	0.022
9, 2018	0.867	0.049	0.044
10, 2018	0.877	0.124	0.031
11, 2018	0.999	0.09	0.057

Table B.3: The first 3 λ_i for PCA from Lisbon's (1.2) data set.

month, year	λ_1	λ_2	λ_3
2, 2015	0.962	0.022	0.006
4, 2015	0.948	0.029	0.007
5, 2015	0.887	0.043	0.026
1, 2017	0.908	0.037	0.016
2, 2017	0.917	0.029	0.022
3, 2017	0.896	0.052	0.023
4, 2017	0.913	0.04	0.017
5, 2017	0.905	0.036	0.022
6, 2017	0.908	0.04	0.025
7, 2017	0.854	0.063	0.031
8, 2017	0.852	0.104	0.017
9, 2017	0.889	0.048	0.036
10, 2017	0.804	0.117	0.038
11, 2017	0.917	0.049	0.015
12, 2017	0.836	0.07	0.034
1, 2018	0.891	0.046	0.022
2, 2018	0.845	0.071	0.031
3, 2018	0.88	0.079	0.015
4, 2018	0.913	0.038	0.028
5, 2018	0.863	0.085	0.025
6, 2018	0.886	0.05	0.024
7, 2018	0.902	0.045	0.017
8, 2018	0.909	0.034	0.018
9, 2018	0.895	0.053	0.022
10, 2018	0.916	0.038	0.021
11, 2018	0.925	0.031	0.015

Table B.4: The first 3 λ_i for PCA from S. Miguel island's (2.1) data set.

month, year	λ_1	λ_2	λ_3
1, 2015	0.914	0.041	0.021
2, 2015	0.95	0.029	0.01
3, 2015	0.947	0.025	0.009
4, 2015	0.912	0.042	0.023
5, 2015	0.857	0.064	0.039
6, 2015	0.814	0.073	0.042
1, 2017	0.999	0.056	0.016
2, 2017	0.999	0.042	0.016
3, 2017	0.887	0.079	0.022
4, 2017	0.915	0.034	0.018
5, 2017	0.871	0.036	0.014
6, 2017	0.922	0.038	0.024
7, 2017	0.92	0.075	0.027
8, 2017	0.91	0.094	0.016
9, 2017	0.866	0.048	0.039
10, 2017	0.868	0.062	0.025
11, 2017	0.886	0.028	0.015
12, 2017	0.893	0.08	0.034
1, 2018	0.928	0.033	0.018
2, 2018	0.843	0.032	0.016
3, 2018	0.911	0.063	0.012
4, 2018	0.926	0.027	0.014
5, 2018	0.901	0.038	0.016
6, 2018	0.94	0.041	0.025
7, 2018	0.92	0.037	0.017
8, 2018	0.896	0.033	0.013
9, 2018	0.907	0.061	0.024
10, 2018	0.921	0.04	0.026
11, 2018	0.881	0.035	0.027

Table B.5: The first three λ_i for PCA from Madeira island's (3.1) data set.

month, year	λ_1	λ_2	λ_3
1, 2015	0.929	0.025	0.02
2, 2015	0.95	0.029	0.01
3, 2015	0.949	0.019	0.013
4, 2015	0.912	0.042	0.023
5, 2015	0.857	0.064	0.039
6, 2015	0.859	0.067	0.028
1, 2017	0.999	0.056	0.016
2, 2017	0.999	0.042	0.016
3, 2017	0.887	0.079	0.022
4, 2017	0.915	0.034	0.018
5, 2017	0.871	0.03	0.014
6, 2017	0.922	0.038	0.024
7, 2017	0.935	0.075	0.027
8, 2017	0.91	0.094	0.016
9, 2017	0.866	0.036	0.03
10, 2017	0.868	0.062	0.025
11, 2017	0.906	0.028	0.015
12, 2017	0.893	0.08	0.034
1, 2018	0.928	0.033	0.018
2, 2018	0.843	0.032	0.016
3, 2018	0.911	0.063	0.012
4, 2018	0.926	0.027	0.014
5, 2018	0.901	0.038	0.016
6, 2018	0.94	0.041	0.025
7, 2018	0.92	0.037	0.017
8, 2018	0.896	0.031	0.017
9, 2018	0.907	0.061	0.024
10, 2018	0.915	0.04	0.026
11, 2018	0.881	0.035	0.027

References

1. Schunk, R. W. & Nagy, A. F. *Ionospheres* (Cambridge University Press, 2000).

2. Russell, C. T., Luhmann, J. G. & Strangeway, R. J. *Space physics* (2016).

3. Glassmeier, K. & Tsurutani, B. Carl Friedrich Gauss - General Theory of Terrestrial Magnetism - a revised translation of the German text. *History of Geo- and Space Sciences* **5** (2014).

4. Barata, T., Pereira, J., Hernández-Pajares, M., Barlyaeva, T. & Morozova, A. Ionosphere over Eastern North Atlantic Midlatitudinal Zone during Geomagnetic Storms. *Atmosphere* **14,** 949. ISSN: 2073-4433. http://dx.doi.org/10.3390/atmos14060949 (2023).

5. Francis, C. *Introduction to plasma physics and Controlled Fusion* (Springer, 2018).

6. Kamide, Y. & Chian, A. C. *Handbook of the solar-terrestrial environment* (Springer, 2007).

7. Kudeki, E. *Applications of Radiowave Propagation* 2006.

8. Britannica. *Stellar classification* 2022. https://www.britannica.com/science/stellar-classification.

9. J., K. H. E. *Physics of space storms from the surface of the Sun to the Earth* (Springer, 2011).

10. D., W. *Sun facts sheet* 2022. https://nssdc.gsfc.nasa.gov/planetary/factsheet/sunfact.html.

11. ESO. *Solar layers* 2003. https://www.eso.org/public/outreach/eduoff/vt-2004/mt-2003/mt-sun.html.

12. C, D. *Fusion on the Sun* 2023. https://euro-fusion.org/fusion/fusion-on-the-sun/.

13. Elliott, J. & Gough, D. O. Calibration of the Thickness of the Solar Tachocline. *apj* **516,** 475–481 (1999).

14. Blin, A. H. *Astrophysics and Cosmology* (2020).

15. Brau, J. *Solar Magnetism - solar dynamo* 2016.

16. spaceweatherlive. *What are sunspots* 2023. https://www.spaceweatherlive.com/en/help/what-are-sunspots.html.

17. Hathaway, D. The Solar Cycle. *Living Rev. Sol. Phys.* **39,** 227 (2015).

18. Landeau, M., Fournier, A., Nataf, H.-C., Cebron, D. & Schaeffer, N. Sustaining Earth's magnetic dynamo. *Nature Reviews Earth & Environment* **3,** 255–269. https://hal.science/hal-03623383 (2022).

19. Balay, S. *Cryptochrome Expression in the Zebrafish Retina: Potential Implications for Magnetoreception* PhD thesis (2018).

20. Ganushkina, N. Y., Liemohn, M. W. & Dubyagin, S. Current Systems in the Earth's Magnetosphere. *Reviews of Geophysics* **56,** 309–332. eprint: https://agupubs.onlinelibrary.wiley.com/doi/pdf/10.1002/2017RG000590. https://agupubs.onlinelibrary.wiley.com/doi/abs/10.1002/2017RG000590 (2018).

21. Case, N. *Solar Wind-Magnetosphere Interactions: A Statistical Analysis of Spacecraft Measurements* PhD thesis (2014).

22. Eastwood, J., Nakamura, R., Turc, L., Mejnertsen, L. & Hesse, M. in *The Scientific Foundation of Space Weather. Series: Space Sciences Series of ISSI* (eds Baker, D. *et al.*) 339–370 (2019).

23. Le, G., Russell, C. & Takahashi, K. Morphology of the ring current derived from magnetic field observations. *Annales Geophysicae* **22,** 1267–1295 (2004).

24. Tsurutani, B. T. in *Magnetic storms* (American Geophysical Union, 1997).

25. Edlefson, E. & Akhavan-Tafti, M. *Cross-Scale Quantification of Storm-Time Dayside Magnetospheric Magnetic Flux Content: A Statistical Analysis* in *AGU Fall Meeting Abstracts* **2021** (2021), SH55C–1849.

26. Natalia Papitashvili, R. C. 2022. https://omniweb.gsfc.nasa.gov/form/dx1.html.

27. GFZ, H.-Z. P. .-. D. G. *KP index - KP index* 2023. https://kp.gfz-potsdam.de/en/.

28. *Auroral Electrojet indices* https://wdc.kugi.kyoto-u.ac.jp/aedir/ae2/onAEindex.html.

29. Chapman, S. The absorption and dissociative or ionizing effect of monochromatic radiation in an atmosphere on a rotating earth. *Proceedings of the Physical Society* **43,** 26–45 (1931).

30. Jursa, A. S. *Handbook of geophysics and the space environment, 4th edition* Final Report Air Force Geophysics Lab., Hanscom AFB, MA. 1985.

31. Langel, R. A., Estes, R. H. & Sabaka, T. J. Uncertainty estimates in geomagnetic field modeling. **94,** 12281–12299 (1989).

32. Jin, S., Jin, R. & Kutoglu, H. Positive and negative ionospheric responses to the March 2015 geomagnetic storm from BDS observations. *Journal of Geodesy* **91,** 613–626 (2017).

33. Danilov, A. D. Ionospheric F-region response to geomagnetic disturbances. *Advances in Space Research* **52,** 343–366 (Aug. 2013).

34. Cowan, G. *Statistical Data Analysis* (Clarendon Press, 1998).

35. J., S. A tutorial on principal component analysis (2014).

36. Ana Paula Santana, J. F. Q. *Introdução à Álgebra Linear* (gradiva, 2010).

37. Morozova, A., Barlyaeva, T. & Barata, T. Updating datasets of ionospheric parameters provided by SCINDA GNSS receiver from Lisbon airport area with full data sets for 2014-2019. *Data in Brief* **47,** 109026 (2023).

38. Barlyaeva, T. *Datasets of ionospheric parameters provided by Scinda GNSS receiver from Lisbon Airport Area* 2020. https://data.mendeley.com/datasets/kkytn5d8yc/1.

39. RENEP. 2023. https://renep.dgterritorio.gov.pt/.

40. RAEGE-Az. 2023. https://raege-az.pt/.

41. GNSS-Lab. 2023. http://www.gnss-lab.org/.

42. Hernández-Pajares, M. J. J. S. J. e. a. *The ionosphere: effects, GPS modelling and the benefits for space geodetic techniques.* 2011. https://doi.org/10.1007/s00190-011-0508-5.

43. Teqc. 2023. https://www.unavco.org/software/data-processing/teqc/teqc.html.

44. NOAA & GOES. 1975. https://www.ngdc.noaa.gov/stp/space-weather/solar-data/solar-features/solar-flares/x-rays/goes/xrs/.

45. Zell, H. *Solar flares: What does it take to be X-class?* 2013. https://www.nasa.gov/mission_pages/sunearth/news/X-class-flares.html.

46. Snow, M., Weber, M., Machol, J., Viereck, R. & Richard, E. Comparison of Magnesium II core-to-wing ratio observations during solar minimum 23/24. *Journal of Space Weather and Space Climate* **4,** A04 (Jan. 2014).

47. Viereck, R. *et al.* The Mg II index: A proxy for solar EUV. **28,** 1343–1346 (2001).

48. Chen, G.-X. *et al.* Statistical characteristics of the day-to-day variability in the geomagnetic Sq field. *Journal of Geophysical Research (Space Physics)* **112,** A06320 (2007).

49. de Michelis, P., Tozzi, R. & Meloni, A. On the terms of geomagnetic daily variation in Antarctica. *Annales Geophysicae* **27,** 2483–2490 (2009).

50. Xu, W.-Y. & Kamide, Y. Decomposition of daily geomagnetic variations by using method of natural orthogonal component. *Journal of Geophysical Research (Space Physics)* **109,** A05218 (2004).

51. Bjornsson, H. & Venegas, S. A. *A Manual for EOF and SVD analyses of Climatic Data* 1997.

52. Paul, A. *et al.* Latitudinal features of Total Electron Content over the African and European longitude sector following the St. Patrick's day storm of 2015. *Advances in Space Research* **61,** 1890–1900 (2018).

53. Stankov, S. M. *et al.* Multi-instrument observations of the solar eclipse on 20 March 2015 and its effects on the ionosphere over Belgium and Europe. *Journal of Space Weather and Space Climate* **7,** A19 (2017).

54. Pazos, M. *et al.* Analysis of the effects of geomagnetic storms in the Schumann Resonance station data in Mexico. *Journal of Atmospheric and Solar-Terrestrial Physics* **193,** 105091 (2019).

55. Morozova, A. L., Barlyaeva, T. V. & Barata, T. Variations of TEC Over Iberian Peninsula in 2015 Due to Geomagnetic Storms and Solar Flares. *Space Weather* **18,** e2020SW002516. arXiv: 1912.00959 [physics.geo-ph] (2020).

56. *International Reference Ionosphere* https://irimodel.org/.

57. *IRI 2016 model* https://ccmc.gsfc.nasa.gov/models/IRI~2016/.

58. Bilitza, D., Rawer, K., Bossy, L. & Tamara, G. International Reference Ionosphere - Past, Present, Future. *Adv. Space Res.* **13,** 3–23 (1993).

59. https://kauai.ccmc.gsfc.nasa.gov/instantrun/iri/.

60. Morozova, A., Barata, T., Barlyaeva, T. & Gafeira, R. Total Electron Content PCA-NN Prediction Model for South-European Middle Latitudes. *Atmosphere* **14,** 1058 (2023).